

Phenomenological and Physical Modelling of High Homologous Temperature Deformation

A thesis submitted by,

Sriharsha Sripathi

In partial fulfillment of the requirement for the award of the degree of

Doctor of Philosophy

in

Nano Science & Technology

Under the supervision of

Dr. Dibakar Das & Prof. K Anantha Padmanabhan

School of Engineering Sciences & Technology



Hyderabad 500046

India

2016

Declaration

I, Sriharsha. S declare that this work, *Physical and Phenomenological Modelling of High Homologous Temperature Deformation*, submitted in partial fulfillment of the requirements for the award of Doctor of Philosophy in Nano Science and Technology to the School of Engineering Sciences and Technology, University of Hyderabad is a bona fide work. This work was done under the guidance of Prof. KA Padmanabhan and Dr. Dibakar Das. This work has not been submitted, either in part or full to any other University or Institution for the award of any degree or diploma.

Sriharsha. S (10ENPT01)

School of Engineering Sciences and Technology

University of Hyderabad



Certificate

This is to certify that the dissertation entitled **Physical and Phenomenological Modelling of High Homologous Temperature Deformation** submitted by **Sriharsha Sripathi**, bearing the registration number **I0ENPT01**, in partial fulfillment of the requirements for the award of the degree of **Doctor of Philosophy in Nano Science and Technology** is a bonafide work carried out by him under our guidance. This dissertation has not been submitted previously in part or in full to this or any other University or Institute for the award of any diploma, degree or equivalent.

Thesis supervisors

Dr. Dibakar Das

School of Engineering Sciences and
Technology
University of Hyderabad

Prof. KA Padmanabhan

School of Engineering Sciences and
Technology & Center for Nanotechnology
University of Hyderabad

Approved by

Prof. M Ghanashyam Krishna

Dean
School of Engineering Sciences and Technology
University of Hyderabad

Table of Contents:

1	Acknowledgements	i
2	List of publications	i
3	List of the symbols, acronyms and meaning of subscripts	ii
4	Abstract	1
5	Introduction	3
6	Universality of the phenomenon of superplasticity	16
7	Validation of the mesoscopic-grain boundary sliding controlled flow model	34
8	Mesosopic grain boundary sliding and inverse Hall-Petch effect	85
9	Conclusions and suggestions for future work	91
10	References	94
<hr/> Appendix: Published manuscripts		
1	Universality of the phenomenon of Structural Superplasticity	
2	Grain size softening effect in intermetallics	
3	Inverse Hall–Petch effect in quasi- and nanocrystalline materials	
4	On the experimental validation of a mesoscopic grain boundary sliding-controlled flow model for structural superplasticity	
5	A Robust Numerical Method for Validating Mesoscopic Grain Boundary Sliding Controlled Flow Model for Structural Superplasticity	

1. Acknowledgements:

The author wishes to acknowledge his Doctoral advisors Prof. KA Padmnanabhan and Dr. Dibakar Das; Doctoral Review Committee members, Prof. Valsa Kumar and Dr. Suresh; Dean of the School of Engineering Sciences & Technology, Prof. M Ghanashyam Krishna; Dr. M Raviathul Basariya, Dr. David John Sherwood, faculty members and non-teaching staff of the School of Engineering Sciences & Technology, friends and family members for their help, support and encouragement.

Sriharsha. S

2. List of Publications:

1. Sripathi Sriharsha, Padmanabhan KA, 2016. *Universality of the phenomenon of Structural Superplasticity*. Materials Science Forum 838-839, 84–88.
2. Basariya MR, Mukhopadhyay NK, Sripathi Sriharsha, Padmanabhan KA, 2016. *Grain size softening effect in intermetallics*. Journal of Alloys and Compounds 673, 199–204.
3. Padmanabhan KA, Sripathi Sriharsha, Hahn H, Gleiter H, 2014. *Inverse Hall–Petch effect in quasi- and nanocrystalline materials*. Materials Letters.
4. Sripathi Sriharsha, Padmanabhan KA, 2014. *On the experimental validation of a mesoscopic grain boundary sliding-controlled flow model for structural superplasticity*. Journal of Materials Science 49, 199–210.
5. Sripathi Sriharsha, Padmanabhan KA, 2012. *A Robust Numerical Method for Validating Mesoscopic Grain Boundary Sliding Controlled Flow Model for Structural Superplasticity*. Materials Science Forum 735, 246–250

3. Symbols, acronyms and subscripts:

Symbols

$\dot{\epsilon}$	Strain rate
α_f	Form factor
γ_0	Unit shear strain
σ	Experimental stress
σ_0	Threshold stress
η	Viscosity
ΔF_0	Free energy of activation
ΔA	Increase in the grain boundary
Γ_B	Specific grain boundary energy
a_0	Atomic diameter
b	Burgers vector
c	Yield criterion
d	Grain size
k	Boltzmann constant
m	Strain rate sensitivity index
n	Stress exponent
ν	Poisson's ratio
p_1, p_2	Constants
r	Residual misfit
A	Grain area
AE	Average error
CC	Correlation coefficient
D	Diffusion coefficient
D_0	Frequency factor
G	Shear modulus
H_0	Instantaneous hardness
H_v	Steady state hardness
L	Grain size
MT	Maximum tolerance

N	Number of grains participating the sliding event
P	Pressure
P_1, P_2	Fitting constants
Q	Activation energy
R	Universal gas constant
SD	Standard deviation
T	Experimental temperature on absolute scale
T_m	Melting temperature on absolute scale
T_{hom}	Homologous temperature
V_0	Volume of the basic sliding unit
W	Grain boundary width
$B_{gbs.glide}, K, K', \beta_1, \beta_2,$	Constants

Acronyms/ Subscripts

GBS	Grain boundary sliding
m-GBS	Mesoscopic-grain boundary sliding
pred	Predicted
expt	Experimental
Tol	Tolerance
opt	Optimum
max	Maximum
hom	Homologous
app	Apparent
abs	Absolute

4. Abstract

The main focus of this study is to critically assess the relevance or otherwise of a *mesoscopic grain boundary sliding controlled flow model*, which has been proposed as the common basis for explaining superplastic deformation in different classes of materials. The rationale behind this approach is that, as superplasticity is observed to be a near-ubiquitous phenomenon, there could be an underlying physical phenomenon responsible for this. If this were the case, *the phenomenology of the superplastic flow process* should also be similar for different classes of materials, i.e. there should be a universal curve for superplastic flow *in all systems* if the experimental variables like stress, strain-rate, strain-rate sensitivity and temperature of deformation are correctly normalized. Starting from these premises, it has been shown that under isothermal conditions the $\log(\sigma) - \log(\dot{\epsilon})$ plots of superplastic materials of different classes and the variation of the strain-rate sensitivity with $\log(\dot{\epsilon})$ for materials of different classes have near-identical features. The viscosity and the free energy of activation of all the alloy systems at (nearly) the same homologous temperature also vary quite similarly. Thus, the universality in the mechanical response of superplastic alloys is demonstrated.

Further, the mesoscopic-grain boundary sliding controlled flow model for superplastic deformation, initially proposed for micron-grained metallic materials, but later extended to include dispersion strengthened alloys, intermetallics, metals with a quasi-crystalline phase, ceramics and ceramic-composites was taken up for consideration. An algorithm was developed to analyze the experimental data in terms of this model, so that many systems could be analyzed successfully. It has been shown that the mesoscopic-grain boundary sliding model satisfactorily describes superplastic deformation in metals and alloys, dispersion strengthened alloys,

ceramics, composites, intermetallics, nanostructured materials and a material containing a quasi-crystalline precipitates and of grain sizes ranging from a few micrometers to a few nanometers. Also, the same approach has been used to satisfactorily explain superplasticity in geological materials and ice. In the present state of its development, in the mesoscopic-grain boundary sliding controlled model, even though theoretical expressions exist, the values of the free energy of activation and the threshold stress needed for the onset of mesoscopic-grain boundary sliding are treated as fitting constants.

By way of applying the ideas to an allied, relevant situation, the mesoscopic-grain boundary sliding controlled model was also used to satisfactorily account for the inverse/ reverse Hall-Petch effect observed in materials when the grain size is in the lower ranges of the nanometer scale.

Future efforts could be towards a theoretical framework at a mesoscopic level, by estimating the threshold stress necessary for the onset of mesoscopic-grain boundary sliding a priori.

5. Introduction

Preamble: Although the phenomenon of superplasticity was observed clearly as early as in the 1930s [1], a formal definition for superplasticity was introduced only in 1991 as:

The ability of a polycrystalline material to exhibit, in a generally isotropic manner, very high tensile elongations prior to failure [2].

This has been shown to be a rather incomplete definition/ description in several ways [3], particularly because it does not contain any quantifiable measures or microstructural details.

Structural superplasticity is normally considered to be the behavior exhibited by fine-grained polycrystalline materials at low strain-rates and when the deforming temperature is more than half the melting temperature on an absolute scale. Superplasticity is observed in many classes of materials. In this thesis superplasticity in metallic alloys, ceramics, composites, metals with a quasi-crystalline phase, quasi-single phase metals, intermetallics, nanostructured materials, geological materials and ice is examined. Further, superplasticity has also been reported in carbon nano-tubes [4] and amorphous materials like bulk metallic glasses [5,6]. Therefore, it would appear that superplasticity is a near-ubiquitous phenomenon, that can be observed in almost all classes of materials under the right experimental conditions [7]. Although Superplasticity is normally reported as a phenomenon observed at low strain-rates, superplastic deformation has also been reported at high strain-rates, at times even exceeding 1 s^{-1} [8]. It may also be noted that when the grain-size decreases to nano-scale, the temperature required for superplastic deformation will come down considerably.

Superplasticity is broadly classified into two categories, as environmental superplasticity and structural superplasticity. Environmental superplasticity is observed in materials exhibiting anisotropy of thermal expansion or solid state phase change during a thermal treatment. Neutron irradiation over a prolonged period also could lead to this type of superplasticity [9]. When materials exhibiting a solid state phase change are cycled between temperatures involving such a change, while simultaneously subjecting them to a small stress, environmental superplasticity can be observed [10].

Structural superplasticity, which is of interest to the present work, is a phenomenon that is observed at high-homologous temperatures. At low homologous temperatures, the stress is a function of both strain and strain rate ($T/T_m \leq 0.3-0.4$), i.e. the flow is strongly influenced by strain hardening as well as strain-rate hardening. As the deforming temperature increases, strain-rate hardening becomes more important and strain hardening becomes insignificant, if microstructure were relatively stable. When the strain-rate effect becomes dominant and the strain hardening effects become negligible, as in superplastic deformation, the steady state flow stress is related to the strain-rate through Equation 5.1.

$$\sigma = K' \dot{\epsilon}^m \quad 5.1$$

As $P = \sigma A$ and $\dot{\epsilon} = -\frac{1}{A} \frac{dA}{dt}$, Equation 5.1 can be rewritten as:

$$\frac{dA}{dt} = -\left(\frac{P}{K'}\right)^{1/m} \left(\frac{1}{A}\right)^{(1-m)/m} \quad 5.2$$

From Equation 5.2 it can be seen that when the value of the strain-rate sensitivity index increases, the dependence of the rate of change of cross-sectional area on the cross sectional area decreases. This resists necking, as a result of which extreme elongations can be obtained prior to failure. This is the phenomenological explanation for superplastic flow. As the value of $m \neq 1$, superplastic flow is not linear, like Newtonian flow. It is often observed that the double logarithmic plot of σ versus $\dot{\epsilon}$ at constant temperature acquires a sigmoidal shape, when the experiments are performed over a sufficiently wide strain-rate range and hence, the strain-rate sensitivity index goes through a maximum with strain-rate. Figure 5.1 shows the sigmoidal curve at constant temperature. The strain-rate regimes normally observed during superplastic deformation are also depicted in Figure 5.1. Due to the sigmoidal nature of the stress versus strain-rate behavior the $\log(\sigma)$ versus $\log(\dot{\epsilon})$ can be divided into three zones, as shown in Figure 5.1. In regions I and IIa the value of the strain-rate sensitivity index, m , increases with increasing strain-rate and reaches a peak value towards the end of region IIa. In regions IIb and III the value of m

continuously decreases. The schematic for the expected behavior of the strain-rate sensitivity index is shown in Figure 5.2.

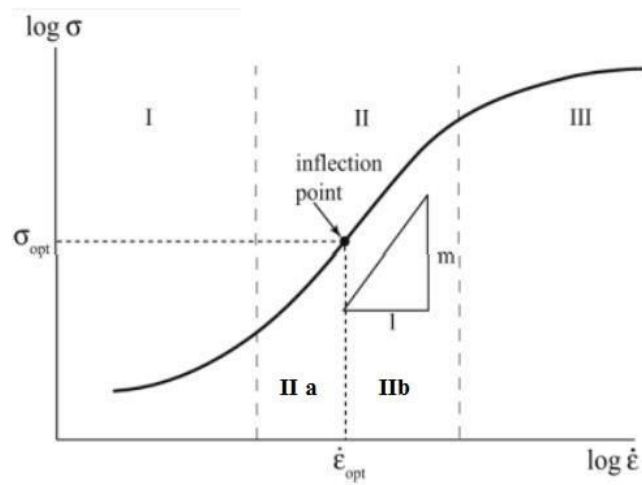


Figure 5.1: Sigmoidal nature of superplastic deformation

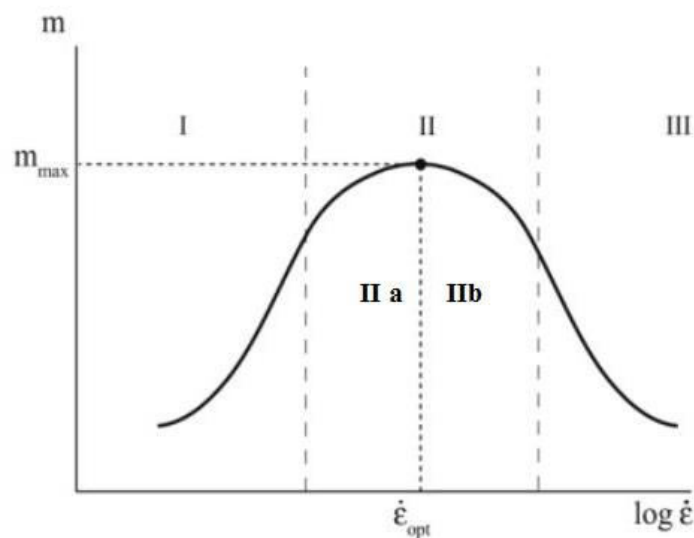


Figure 5.2: Variation of the strain-rate sensitivity index with strain rate

The strain-rate sensitivity index, m , is normally calculated as shown in Equation 5.3 [3,9,11]. This value of m is then assigned to either the mean value of the two strain-rates or by convention, to the lower of the two strain-rates.

$$m = \frac{\log(\sigma_1 / \sigma_2)}{\log(\dot{\epsilon}_1 / \dot{\epsilon}_2)} \quad 5.3$$

Microstructural features like grain-size, shape, misorientations between grains, texture, dislocation density, segregation, defects etc. are all expected to influence the superplastic response of a material. Nevertheless, the grain-size is used as the only unique microstructural parameter in most of the experimental and theoretical studies [12]. Quite often, a generic equation of the form shown below is used to describe high-temperature deformation/ steady-state creep [13].

$$\dot{\epsilon} = A \frac{D_0 G b}{kT} \left(\frac{b}{d} \right)^p \left(\frac{\sigma}{G} \right)^n \exp\left(-\frac{Q}{kT} \right) \quad 5.4$$

Experimental investigators of a good number of systems considered for analysis in this thesis have suggested models for superplastic flow mostly based on Equation 5.4. However, it needs to be noted that A and n are not at all constants, which also lack physical significance. Their values, for the same material, differ depending on the experimental conditions. For example, for the ten aluminum systems analyzed in this thesis the values of A ranged from $\sim 10^6$ to $\sim 10^{11}$ and n from 1 to 4.4. The same will be described in a more detailed manner in Chapter 7. Further, A and n are not independent of each other, but are interdependent in a unique manner, due to which they cannot be determined independent of each other [14]. As can be seen from Equation 5.4, the flow stress is normalized with respect to the shear modulus. The latter is not a good choice as a reference parameter when it is necessary to determine the activation energy for the rate controlling process (required in many, if not the most, cases), because the temperature dependences of stress and the shear modulus are not identical. Therefore, it will not be possible to separate the effect of stress from that of temperature on the activation energy for the rate controlling process. How to overcome this problem and the correct way of normalizing the stress in a constitutive equation for high temperature deformation (including superplastic deformation) are presented in a recent publication [15]. In contrast, it will be shown below that in the analysis based on the mesoscopic grain boundary sliding controlled flow model, there are no such ambiguities and the experimental results can be understood without invoking adjustable parameters. Prior to undertaking this exercise, a brief review of some of the other models often discussed in the literature on superplasticity will be considered.

Models used to explain superplastic deformation: Developing a comprehensive theory to describe real-time deformation is very difficult. Such theories can be tractable when they regard the material as a continuum. Introduction of sensible constitutive relations to describe the properties of the material will be the primary challenge. This can be achieved by understanding the physical properties of the material in such a way that the microstructure can be understood and controlled in a way that improves the properties [16]. Theories describing superplastic flow can broadly be divided into diffusional flow mechanisms, creep based models, GB deformation models and also, as experiments are often insufficient for isolating individual mechanisms, models involving a combination of flow processes.

Diffusion Creep accommodated by GBS [13]: Experimentally it is seen that on an average the interior grains of superplastic alloys remain equiaxed and appear to retain their size and shape after extensive tensile elongations. These observations led to a suggestion that superplasticity could be understood as a diffusion-accommodated process in which grains slide relative to each other and switch their neighbors in the course of deformation. This approach is based on an idea that the crystal deformation by dislocation motion in the vicinity of grain boundaries can be controlled by GB diffusion while deformation by dislocation creep in the grain interiors is controlled by lattice diffusion. Here it is assumed that crystal deformation in the vicinity of grain boundaries is controlled by the annihilation of dislocations of opposite sign that climb together from the plane of the GB. Further, it is also assumed that the transition from lattice diffusion controlled deformation at high strain-rates to GB diffusion controlled creep at low strain rates is controlled by the size of the sub-grains relative to the grain-size. At higher strain-rates, the sub-grain size is small relative to the grain-size and deformation is controlled completely by creep process in the grain interior. At low strain-rates, the sub-grain size approaches the grain size, with the consequence that little substructure is created in the grain interiors and creep is controlled by GB processes. This model for an iso-strain rate can be described as in Equation 5.5:

$$\frac{\tau}{G} = \left(1 - \frac{10Gb}{\tau L}\right)^6 \left(\frac{\tau}{G}\right)_c + \left(1 - \left(1 - \frac{10Gb}{\tau L}\right)^6\right) \left(\frac{\tau}{G}\right)_m \quad 5.5$$

where,

$$\left(\frac{\tau}{G}\right)_c = \left(\frac{\dot{\gamma} b^3 kT}{3500 s G \Omega D_1}\right)^{0.2} \quad \text{and} \quad \left(\frac{\tau}{G}\right)_m = \left(\frac{\dot{\gamma} b^3 kT}{3.07 G \Omega D_1 \delta_{gb} D_{gb}}\right)^{0.25}$$

It needs to be noted that even according to the authors this model is phenomenological and many constants, which cannot be generalized, are used in the model.

Diffusional Flow Mechanisms [13]: Diffusion-controlled structure change (often involving easier migration of vacancies) could be necessary for superplastic deformation. The process of diffusion gains more significance in the light that additions of elements that enhance diffusivity have a positive effect on superplastic properties. As superplasticity is a high homologous temperature and quite often a low strain rate phenomenon, Nabarro-Herring and Coble creep equations [9] (shown below) are used to describe superplastic flow.

$$\dot{\epsilon} = \frac{A_1}{L^2} \frac{\Omega \sigma}{kT} D_L \quad 5.6$$

$$\dot{\epsilon} = \frac{A_2}{L^3} \frac{\Omega \sigma}{kT} 2D_{gb} \quad 5.7$$

A creep-based model by Weertman [17] is also sometimes used. In this model deformation occurs by the glide of dislocations from sources within grains. These dislocations spread until they are blocked by dislocations spreading from other sources, forming edge dislocation dipoles. These dipoles are removed by bulk diffusion. There can also be dislocation pile-ups, which may then have to climb through bulk diffusion. This model is represented using Equation 5.8.

$$\dot{\epsilon} = \alpha D_b \left(\frac{\sigma}{G}\right)^{3.5} \left(\frac{\sigma \Omega}{kT}\right) \quad 5.8$$

This model and other creep-based models, yield poor fits with the experimental results.

Ashby-Verrall's Diffusion-Accommodated Creep Model [18]: This model is described by Equation 5.9 as:

$$\dot{\epsilon} = \frac{A\Omega\sigma}{kTL^2} D_L L + \frac{3.3WD_{gb}}{LD_L} \quad 5.9$$

The model suggests that the diffusive flow controls the deformation while GBS is only an inherently fast accommodation process, which at no stage is rate controlling. Here it has been pointed out that diffusional transport must occur from the centre of the grain boundaries toward the corners, if normal traction continuity across the boundary is to be maintained. This would not be true because, if grains experience a net torque, it can cause a loss of matter from grain corners to fill the center of grain boundaries. Several other limitations have also been pointed out and can be found in the published literature. Some more models have been suggested to explain the phenomenon of superplasticity and these can be found in some of the well-known expert-level books on this subject [9,19,20].

Mesoscopic grain boundary sliding controlled flow model [7,9,21–26]: Essentially, in this model work has to be done to overcome the grain boundary viscosity before shear displacements between the grains occur, which leads to large scale macroscopic deformation. This model assumes that the rate controlling process for superplastic deformation will be confined to grain/ interphase boundary regions. Further, dislocation/ partial dislocation emission and/ or diffusion will ensure the continuity of strain across grains and coherence of deformation. From experimental results [9,19,20] it is already known that GBS is the dominant mechanism during superplastic deformation; diffusional flow and dislocation activity will be present to limited extent. An additive combination of the strain-rates due to GBS, diffusion creep and intragranular slip ($\dot{\epsilon}_{total} = \dot{\epsilon}_{GBS} + \dot{\epsilon}_{DC} + \dot{\epsilon}_{IS}$) [3] cannot account for the sigmoidal $\sigma - \dot{\epsilon}$ curve, normally obtained during superplastic deformation over a considerable range of strain rates; it has also been reported that there would be no independent contribution from dislocation motion to superplastic

deformation. It is hence suggested that the rate of superplastic deformation is a result of the combined operation of GBS and diffusional flow and the existence of dislocation activity will be in a non-rate controlling manner. Although the two rate mechanisms (GBS and diffusion) are interdependent, one mechanism can be assumed to be the rate controlling mechanism by assuming the other mechanism to be the faster process. The faster process will not be a part of the rate equation. The m-GBS model for superplastic deformation regards grain boundary sliding to be the rate controlling process.

M-GBS model analyses GBS as a two scale process; at atomistic level, the initial relative displacement of a grain with respect its neighbor along their common boundary is considered; next, development of this GBS process to a mesoscopic scale (~ a grain size or more) due to the formation of a plane interface is considered. When such plane interfaces form simultaneously in various parts of the deforming specimen, they can interconnect, due to which large scale GBS is obtained and a consequence of this will be significant specimen elongation.

It would be quite difficult to exactly describe the actual grain shapes in materials; for the sake of analysis, while tetrakaidecahedron represents the ideal shape, rhombic dodecahedron resembles the real grains to the closest [27] and it has been assumed to be the grain shape in the m-GBS model. Figure 5.3 shows both the grain shapes, along with the shaded regions in which the rate controlling processes are assumed to be confined.

It is known [22] that high-angle grain boundaries are conducive to superplastic deformation and any low-angle grain boundaries present are transformed by deformation into high-angle grain boundaries during the course of superplastic flow, provided the sliding rates at these boundaries are adequate to match those of the fast moving boundaries. In fact, the investigators of one of the systems analyzed here, Ref. [28], have experimentally reported the near-complete transformation of low-angle grain boundaries into high-angle grain boundaries, in the course of superplastic deformation.

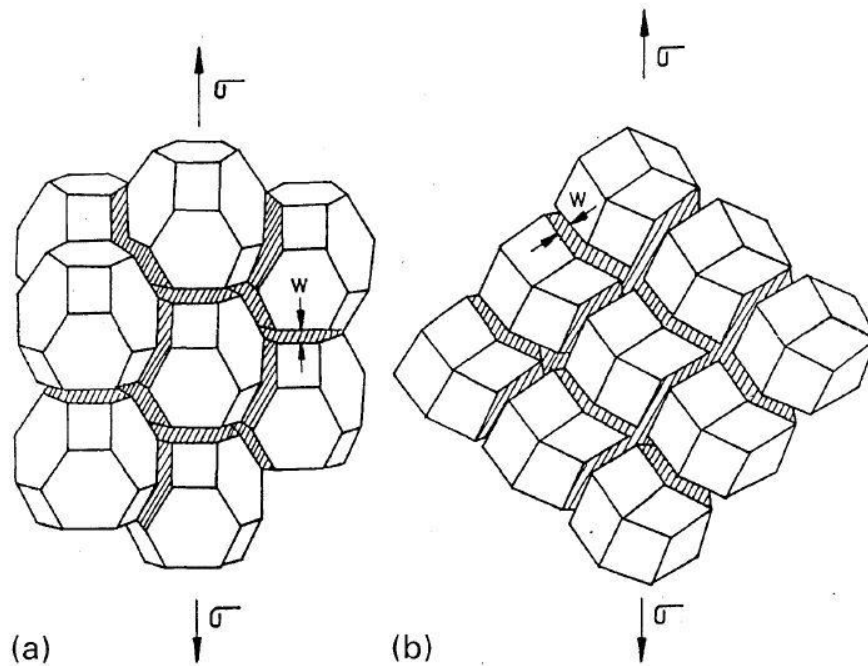


Figure 5.3: Schematic of rate controlling flow of grain boundaries surrounding arrays of essentially non-deforming (apart from what is needed for non-rate controlling accommodation between grains to ensure strain compatibility) grains during occurrence of optimal structural superplasticity. Idealized shapes are suggested to be (a) equilibrium (tetrakaidecahedron), and (b) real shape (rhombic dodecahedron) of grains (reproduced from [25])

The m-GBS approach divides the high-angle grain boundary into a number of atomic scale ensembles, surrounding the free volume sites present at discrete locations characteristic of the boundary misorientation. For mathematical development, as shown in Figure 5.4, the shape of the basic sliding unit is assumed to be an oblate spheroid, with a size of 5 atomic diameters in the boundary plane and 2.5 atomic diameters in the perpendicular direction, when the GB width is assumed to ~ 2.5 atomic diameters.

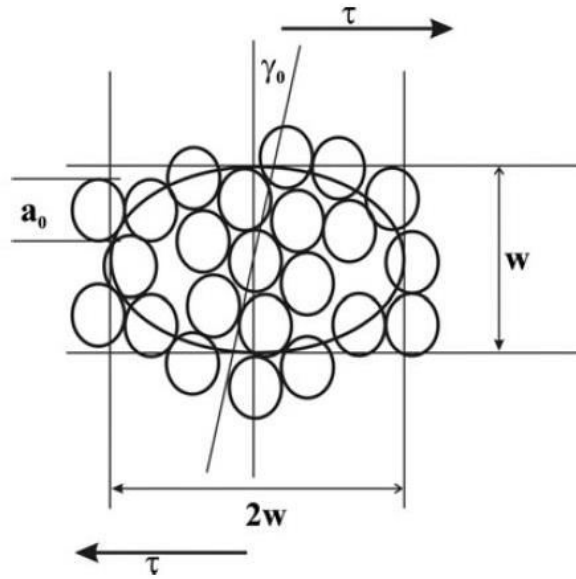


Figure 5.4: Shape of the basic sliding unit (reproduced from [7])

The choice of shape of an oblate spheroid is because the stress-strain field that develops inside an oblate spheroid when it is deformed is uniform, has already been worked out and from a knowledge of this stress/ strain field, important engineering properties of the material can be known [29]. Presence of a free volume makes the basic sliding unit weaker compared with the rest of the boundary. Based on bubble raft experiments and MD simulations, average shear strain associated with unit shear, when an ensemble moves from a stable/ metastable position to another is assumed to be ~ 0.1 [30,31]. The distortion and the momentary volumetric dilatation present when the ensemble goes from one stable/ metastable configuration to another through a saddle point constitutes the free energy of activation associated with the boundary sliding process. (When the deforming oblate spheroid and its surrounding are viewed together it is referred to as the free energy of activation. But when only the deforming oblate spheroid is considered, it is commonly known as the activation energy for the deformation process [32]. Therefore, according to Eshelby [29], the free energy of activation for the boundary sliding event is given by,

$$\Delta F_0 = (\beta_1 \gamma_0^2 + \beta_2 \epsilon_0^2) G V_0 \quad 5.10$$

where,

$$\beta_1 = 0.944 \frac{1.59 - p}{1 - p}, \beta_2 = \frac{4(1 + p)}{9(1 - p)}, \text{ (for an oblate spheroid)}$$

If the yield behavior of the superplastic solid is governed by the von Mises criterion, $\epsilon_0 = \gamma_0/3^{0.5}$; $\sigma = 3^{0.5}\tau$. The volume of the basic sliding unit (oblate spheroid) is $V_0 = (2/3) \pi/W^3$. The grain boundary width, W , is assumed to be ~ 2.5 times the atomic diameter (see above).

However, the sliding events, after sliding for the length of about a grain diameter faces a steric hindrance like a triple junction. This hindrance will terminate the relative motion between the grains, limiting the GBS event. For substantial sliding to a mesoscopic scale, two or more grains should align and form a plane interface. Substantial elongation can be obtained then by the simultaneous plane interface formation in different regions of the sample and long range sliding along these plane interfaces, which when interconnected will give rise to extensive boundary sliding. The sliding event at an individual boundary is depicted in Figure 5.5, while its mode of spreading to the adjacent/ contiguous grains is shown in Figure 5.6.

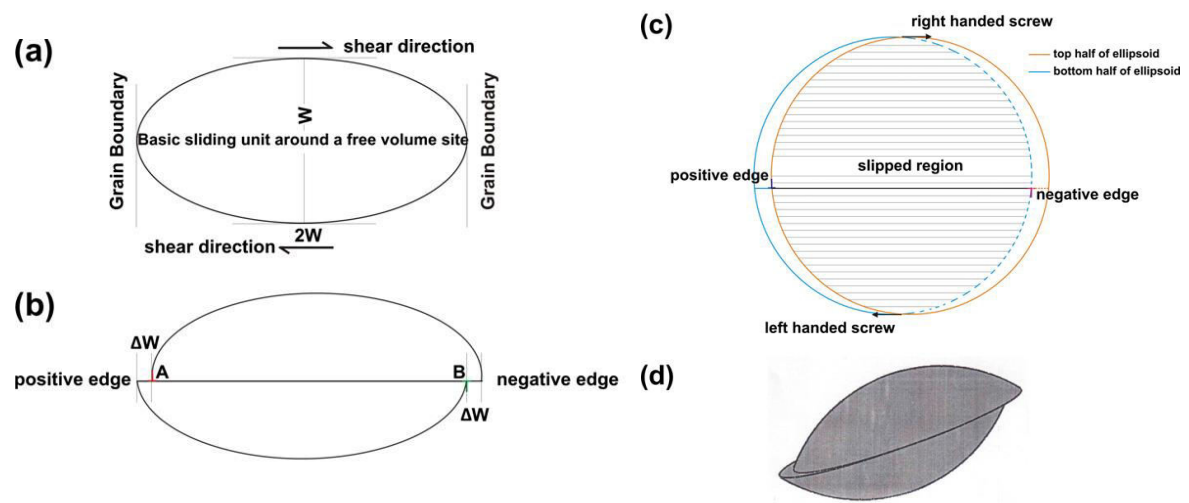


Figure 5.5: Description of unit shear event at a grain boundary: (a) undeformed oblate spheroid, (b) deformed oblate spheroid, view in elevation, (c) plan view of deformed spheroid, with closure failure at the two extremities indicated in (b) and (c), (d) isometric view (reproduced from [7])

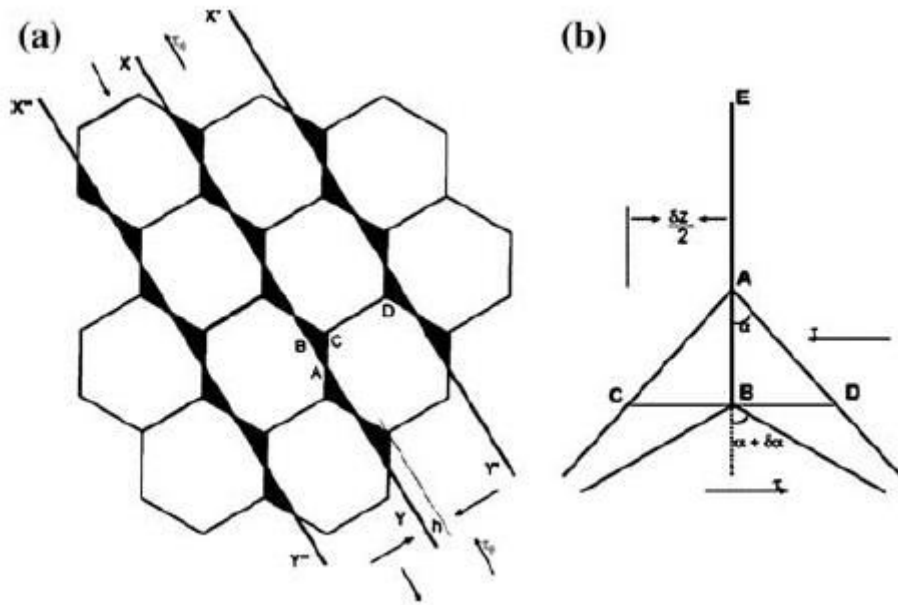


Figure 5.6: a. A 2D section of a specimen cross-section, with the black regions indicating the regions from which matter is to be removed to form the plane interfaces; b. a schematic for the migration of one of the boundaries at a triple junction (the vertical one downward in this picture) during interface formation as such a step will minimize the overall free energy of the system (reproduced from [23])

The plane interface formation during an m-GBS event by the movement of atoms in the shaded regions in Fig. 5.6 requires some energy expenditure, which gives rise to a long range threshold stress [26]. This has been estimated in Refs. [25,26] as,

$$\tau_0 = \left(\frac{2G\Gamma_B (\Delta A / A)}{\alpha_f (NA)^{0.5}} \right)^{0.5} \quad 5.11$$

As the grain shape is assumed to be rhombic dodecahedron, the area per grain that will participate in plane interface formation is $A = (3^{0.5}/4) L^2$ and the change in area produced by plane interface formation is $\Delta A = (1/2^{0.5} \cdot 4) L^2$. Noting that $\sigma_0 = 3^{0.5} \tau_0$, the rate equation for the model can be written as [7,23,25,26].

$$\dot{\varepsilon} = \frac{2cW\gamma_0v}{L} \sinh\left(\frac{(\sigma - \sigma_0)c\gamma_0V_0}{2kT}\right) \exp\left(-\frac{\Delta F_0}{kT}\right) \quad 5.12$$

It is pertinent to note that in Equation 5.12 there are no adjustable constants; each constant is well defined and is either already known or can be calculated from the expressions derived. Validation of the above equations and the further development of the m-GBS model has been a major concern of this thesis.

6. Universal nature of the phenomenology of superplasticity

Introduction: As mentioned in the Introduction, a sigmoidal curve is observed in various classes of superplastic materials, when the isothermal, steady state $\log(\sigma)$ values are plotted against the $\log(\dot{\epsilon})$ values [9,19,20]. In this Chapter it is suggested that on proper normalization of the stress, strain-rate and the other variables, universal curves can be obtained for almost all materials that exhibit superplasticity. While, in principle, all systems for which superplastic behavior has been established could be taken up for investigation to either validate or reject the above hypothesis, it will be seen here that the normalization of the stress, strain-rate, strain-rate sensitivity index, temperature, free energy of activation for the rate controlling process and “absolute” viscosity of the superplastic medium has to be done with respect to the stress/ strain-rate, strain-rate sensitivity index and absolute viscosity value corresponding to the point of inflection in the isothermal, sigmoidal $\log(\sigma) - \log(\dot{\epsilon})$ plot, which is the point of maximum value in m / percentage elongation etc. (if the parameters pertaining to this point are chosen as the base, no problem of convergence will be there in any series expansion, as all the normalized parameters then will have values less than unity). Evidently, the free energy of activation should be normalized with respect to the melting point of the superplastic system, as this parameter (the melting point) determines the strength of the inter-atomic bonds (there is a direct dependence between the two parameters). The first restriction (i.e., identification of the parameters at the point of inflection in the isothermal, sigmoidal $\log(\sigma) - \log(\dot{\epsilon})$) necessitates that only systems in which the region II to region III transition in the sigmoidal plot is clearly defined by the reported experimental data could be taken up for the present study. As a result, the experimental data pertaining to two Zinc alloys [33,34], two Aluminum alloys [35,36], one magnesium alloy [37] and one titanium alloy [38] are considered here. A good correlation coefficient in terms of a universal curve could be obtained for all the parameters of interest in all the systems investigated here.

In the past, using limited experimental data, the concept of universality in the behavior of superplastic alloys was probed by our group, focusing just on the variations in the strain-rate sensitivity index, m , in different systems [3,39]. However, in those studies even with respect to this parameter (m), the temperature-dependence of m was not taken into

account. Therefore, the earlier analysis is regarded here as rather limited. In this chapter, the universality in the behavior of superplastic alloys is studied over a wide range of temperatures, with respect to all the parameters mentioned above, based on experimental results reported in [28,35,40–42].

Unlike solids, which have a viscosity in the range of $\sim 10^{14}$ Nms⁻¹ and more, most superplastic materials possess an apparent viscosity of $\sim 10^3 - 10^8$ Nms⁻¹ [9]. Also, it is known that in the optimal region, superplastic deformation exhibits a viscoplastic behavior, i.e. the “apparent” viscosity decreases with increasing strain rate [9,43]. A study of universality in mechanical response, therefore, should also include universal “absolute” viscosity curves for the superplastic materials, provided the normalization steps are carried out properly. This proposition is established here using the experimental results reported in Refs. [34,44–48].

When a common rate controlling mechanism is suggested, as done by our group, regardless of the material in which superplasticity is studied, a case exists that the free energy of activation (as shown earlier, the same as the activation energy for the rate controlling process, in the popular language found in the literature [32]) obtained for all the materials should be similar/ comparable, when a proper normalization is done, i.e., with respect to (RT_m) (T_m is the melting point; it is assumed, as done always in the classical domain that the temperature dependence to follow a Maxwell-Boltzmann distribution). This idea is established using the values of the free energy of activation of 37 superplastic systems.

Thus, in this chapter a case for the existence of a multidimensional, universal relationship involving $\sigma - \dot{\epsilon} - m - \eta - T - \Delta F_0$ in a normalized hyper-space for all those superplastic systems, for which adequate experimental data could be found, is presented.

The sigmoidal curve: Figures 6.1 and 6.2 show a sigmoidal curve and a schematic indicating the variation of the strain-rate sensitivity index with strain-rate. Initially, the strain-rate sensitivity index increases with increasing strain-rate and after reaching a peak value, it decreases with a further increase in strain-rate. That value of the strain-rate at which m is a maximum is regarded as the optimal strain-rate for superplastic flow and the

corresponding stress is considered as the optimal stress - Figure 6.1. Here the optimal stress, strain-rate (both of which correspond to the maximum in “m” value for a given grain size and temperature) and m_{\max} are taken as the normalization bases. Further, the experimental temperature is normalized with respect to the melting temperature of the material (homologous temperature) and the apparent viscosity, η_{app} , with respect to the “absolute viscosity”, η_{abs} , i.e., the viscosity at the stress level, σ_c , at which $m = 1.0$ in the normalized stress – strain-rate space [15]. Hence, the expected multidimensional relationship is as shown in formalism 6.1.

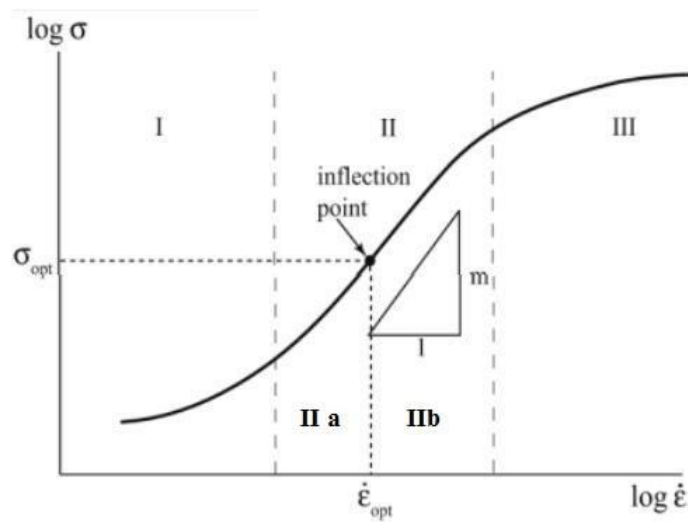


Figure 6.1: Sigmoidal nature of superplastic deformation (after KAP-Davies, 1980)

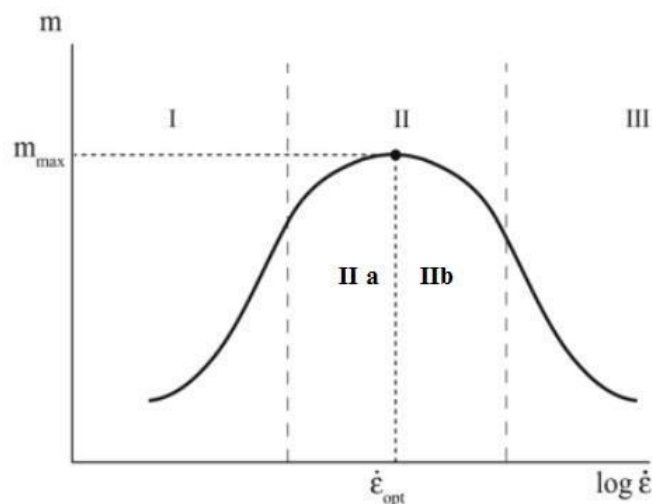


Figure 6.2: Variation of the strain rate sensitivity index with strain rate (after KAP-Davies, 1980)

$$\sigma / \sigma_{\text{opt}} - \dot{\epsilon} / \dot{\epsilon}_{\text{opt}} - m / m_{\text{max}} - T / T_m - \eta_{\text{app}} / \eta_{\text{abs}}$$

6.1

Equation 6.1 is a universal curve in hyper-space of five dimensions.

Experimental data reported in [33–38] have been considered for analysis. As already mentioned, these data sets represent the $\log(\sigma)$ versus $\log(\dot{\epsilon})$ relationship over a range wide enough to include all the relevant regions of superplastic deformation. The optimal values of m , σ and $\dot{\epsilon}$ were chosen as explained above (at the point of inflection) and they were used as the normalization bases. Table 6.1 displays the optimal values of m , σ and $\dot{\epsilon}$ at each temperature of deformation for the systems analyzed. The test temperature, T , as stated before, was normalized with respect to the melting point, T_m , of the material involved.

Table 6.1: Normalizing details of the systems analyzed

Sl. No.	Composition	T, K	T/T _m	m _{max}	σ _{opt} , MPa	ḡ _{opt} x10 ⁻³ , s ⁻¹
1	Zn 22Al [33]	423	0.56	~0.5	86.91	13.13
		473	0.62		37.0	7.20
		503	0.66		14.88	3.28
2	Zn 22Al [34]	453	0.60	~0.5	20.89	0.63
3	Al 5.7Mg 0.32Sc [35]	573	0.61	0.42	32.70	5.64
		623	0.67	0.42	60.62	142.98
		673	0.72	0.43	71.03	589.09
		723	0.77	0.49	63.20	1471.30
4	Al 3Mg 0.2Sc [36]	573	0.61	~0.5	98.39	32.09
		623	0.67		40.33	32.09
		673	0.72		29.16	32.09
		723	0.77		22.86	32.09

5	Mg 4Y 0.7Zr [37]	598	0.65	~0.5	95.56	10.60
		623	0.67		46.89	10.60
		648	0.70		23.01	10.60
6	Ti 6Al 4v [38]	1023	0.53	0.45	17.783	0.78
		1123	0.58	0.51	57.54	0.63
		1173	0.61	0.52	50.12	0.50
		1198	0.62	0.51	20.89	0.56

Compositions are in weight percent up to here

The normalized experimental data for the different systems is presented in Figure 6.3.

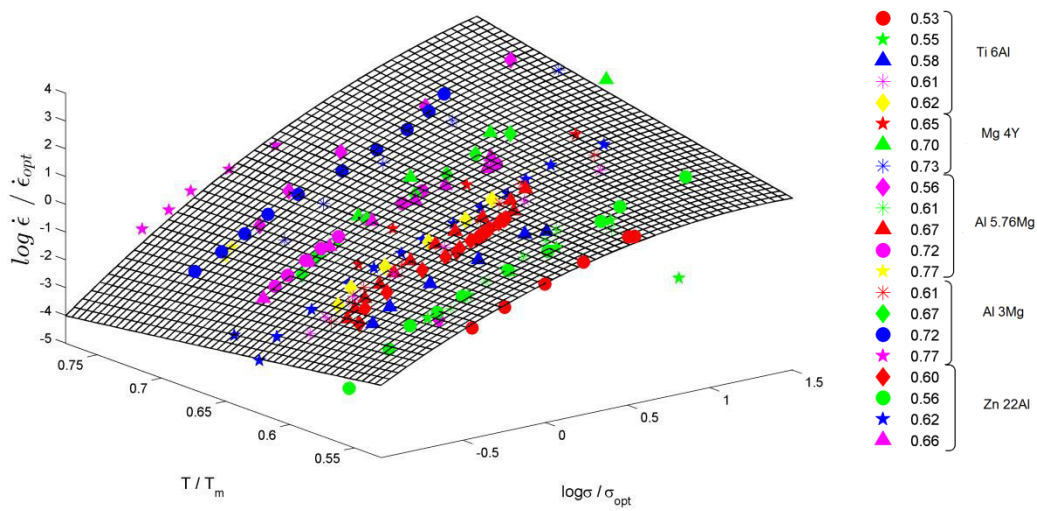


Figure 6.3: Universality in stress-strain rate-temperature relationship for superplastic materials

The equation resulting from the plot presented in Figure 6.3 is expressed as Equation 6.2 below.

$$f(x, y) = 0.53 - 1.6x - 1.73y + 1.21x^2 + 6.6xy - 0.66y^2 \quad 6.2$$

In Equation 6.2 normalized strain-rate is considered a function of homologous temperature and normalized stress; i.e. $f(x, y) = z \sim \log(\dot{\epsilon}/\dot{\epsilon}_{\max})$, $x \sim T/T_m$ and $y \sim \log(\sigma/\sigma_{\text{opt}})$. The correlation coefficient for the above fit is 0.96.

A commonly used equation to describe high temperature deformation is:

$$\dot{\epsilon} = a\sigma^n \exp\left(-\frac{\Delta F_0}{RT}\right) \quad 6.3$$

For mathematical convenience, this is written here as,

$$\dot{\epsilon} = A\sigma^n \exp\left(-\frac{B}{T}\right) \quad 6.4$$

where $A = a$, $B = (\Delta F_0/R)$.

For explaining superplastic flow, many authors [2,19,20,49,50] have taken $n \approx 2$ [19,20], as they assume that a value of n , the stress sensitivity (inverse of m , the strain rate sensitivity index), implies that the flow is dominated/ controlled by grain boundary sliding. A fit was attempted for all the systems presented in Table 1 using Equation 6.4 with $n = 2$ and the correlation coefficient for this fit is reported in Table 6.2.

In Chapter 7 it has been demonstrated that a micro-mechanistic model based on a physical idea that optimal structural superplastic flow is rate controlled by grain boundary sliding that develops to a mesoscopic scale (\sim of the order of a grain diameter or more) is effective in explaining the phenomenon of optimal superplasticity using data pertaining to 42 systems. Mathematical development of the idea has shown that this mechanism is represented as,

$$\dot{\epsilon} = \frac{2cW\gamma_0 v}{L} \sinh\left(\frac{(\sigma - \sigma_0)c\gamma_0 V_0}{2kT}\right) \exp\left(-\frac{\Delta F_0}{kT}\right) \quad 6.5$$

For the isothermal case, this equation reduces to a form $Y = A \sinh(a^*X)$. The temperature dependence is Maxwell-Boltzmann. A correlation coefficient, estimated by

considering the normalized strain-rate as a function of normalized temperature and normalized stress was obtained.

On inspection, the $\log(\sigma) - \log(\dot{\epsilon})$ curve up to the point of inflection (the optimal range) appears to be quadratic. A second order regression fit was also attempted for all the data. The results are reported in Table 6.2.

Table 6.2: Results of the test for universality of superplasticity data for different systems

Sl No	Fit type	CC
1	2 rd order polynomial fit*	0.96
2	Equation 6.3 (with n=2; model popularized by several authors)	0.69
3	Equation 6.4 (m-GBS model)	0.95

Correlation coefficient presented pertains to the systems presented in Table 1

*Regression analysis; no theoretical basis

An examination of Table 6.2 reveals that the fit corresponding to the m-GBS model (Equation 6.5) is very good. The quadratic fit, presented as Serial Number 1 in Table 6.2 is based on a regression analysis, which is devoid of any physical meaning. This mathematical fit is also equally good. However, this fit does not provide a physical insight to the phenomenon of superplasticity. In contrast, the fit in terms of Equation 6.3, with $n = 2$, very popular with many authors who claim that this is the mathematical form of GBS-dominated superplastic flow [2,19,20,49,50], gives a rather poor fit ($CC < 0.70$) of the experimental data. Therefore, the present analysis, in addition to establishing the universality of the stress – strain-rate relationship in superplastic materials, provides a point in favor of the m-GBS model for optimal structural superplasticity and against the suggestion that GBS is characterized by a physical process (or processes) that has a value for $m = 0.5$.

Viscosity: As mentioned already, the rheological response of superplastic materials is viscoplastic, wherein the (apparent) viscosity (the ratio of shear stress to shear strain-rate

under isothermal conditions) in the optimal range decreases with increasing strain-rate. A procedure to obtain the dimensionless isothermal stress – strain-rate relationship for a superplastic alloy in the optimal region has been outlined in [15]. A method for determining the stress, σ_c , at which $n = 1$ (Newtonian viscosity) in the normalized stress – strain-rate space has also been given. From the analysis presented in [15], it follows that steady state optimal superplastic flow in a material can be written as,

$$\log(\dot{\epsilon}) = \log(A) + (1 + P_0) \log(\sigma) - \frac{P_0}{\sigma_c} \sigma \quad 6.6$$

This reduces to a form,

$$Y = C_1 + C_2 \log(X) - C_3 X \quad 6.7$$

where the several (experimental) values of Y ($\log(\dot{\epsilon})$) and X (σ) are known. Data at each temperature for the systems [34,44–48] were fitted using Equation 6.7. The value of C_2 in such a fit is given by $C_2 = 1 + P_0$; and $C_3 = P_0 / \sigma_c$. The value of σ_c , which is the stress value at which $n = 1$ in the normalized space, and the corresponding $\dot{\epsilon}$ values are used to determine the absolute viscosity, η_{abs} , from the relation, $\sigma_c / \dot{\epsilon}_{at \sigma_c} = 3\eta$ (von Mises yield behavior is assumed to be present in the superplastic material). The data for different systems were analyzed and these are plotted in Figure 6.4. Here the homologous temperature range was from 0.92 to 0.50. Evidently, the data pertaining to different classes of materials (aluminum, copper, zinc and magnesium alloys and cobalt and titanium based intermetallics) exhibit similar behavior. The differences in the homologous temperatures for the different materials are responsible for the small scatter in the plots.

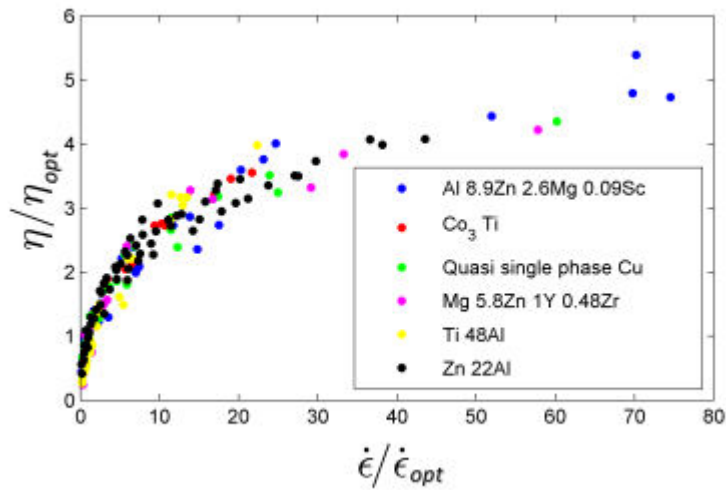


Figure 6.4: “Absolute” viscosity v/s normalized strain-rate for different materials

A correlation coefficient of ~ 0.95 was obtained for a second order fit between the normalized strain-rate and normalized viscosity. If temperature was considered, the correlation coefficient for the third order fit will be ~ 0.96 . The different data points shows that all the materials studied follow a universal curve. The scatter further decreases if the actual homologous temperature at which the data is generated is also taken into account; the 3D plot is presented in Figure 6.5. Equations 6.8 and 6.9 present the fit obtained for second and third order fits respectively.

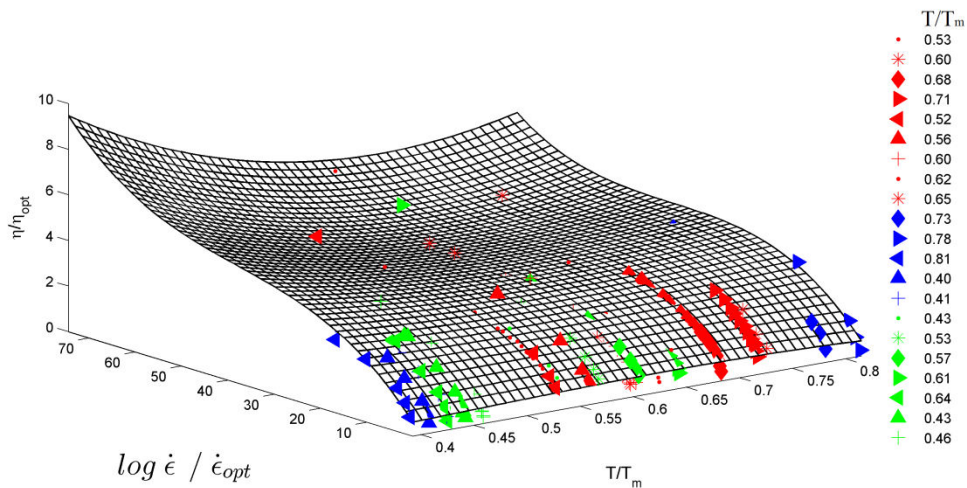


Figure 6.5: Normalized viscosity v/s normalized strain-rate for different homologous temperatures

$$f(x) = -0.0015x^2 + 0.15x + 0.95 \quad 6.8$$

where, $f(x) \sim \eta/\eta_{\text{opt}}$; $x \sim \dot{\epsilon} / \dot{\epsilon}_{\text{opt}}$.

$$f(x,y) = 8.34y^2 - 0.0014x^2 + 0.06xy - 12.18y + 0.11x + 5.16 \quad 6.9$$

where, $f(x,y) \sim \eta/\eta_{\text{opt}}$; $x \sim \dot{\epsilon} / \dot{\epsilon}_{\text{opt}}$; $y \sim T/T_m$.

Strain-rate sensitivity index: As pointed out earlier, due to the sigmoidal behavior present in the isothermal, double logarithmic plots of stress versus strain-rate a peak value is observed in the strain-rate sensitivity index. Based on limited data, earlier it was shown that when the strain-rate sensitivity index is normalized with respect to the peak value of the strain-rate sensitivity index and the strain-rate is normalized with respect to the corresponding value of the strain-rate for m_{max} , a universal curve between the normalized strain rate sensitivity index and the strain rate is seen [3,39]. Experimental results reported in [28,35,40–42] were considered for the present, more detailed analysis. The homologous temperature ranged from 0.56 to 0.77. The results are plotted in Figure 6.6.

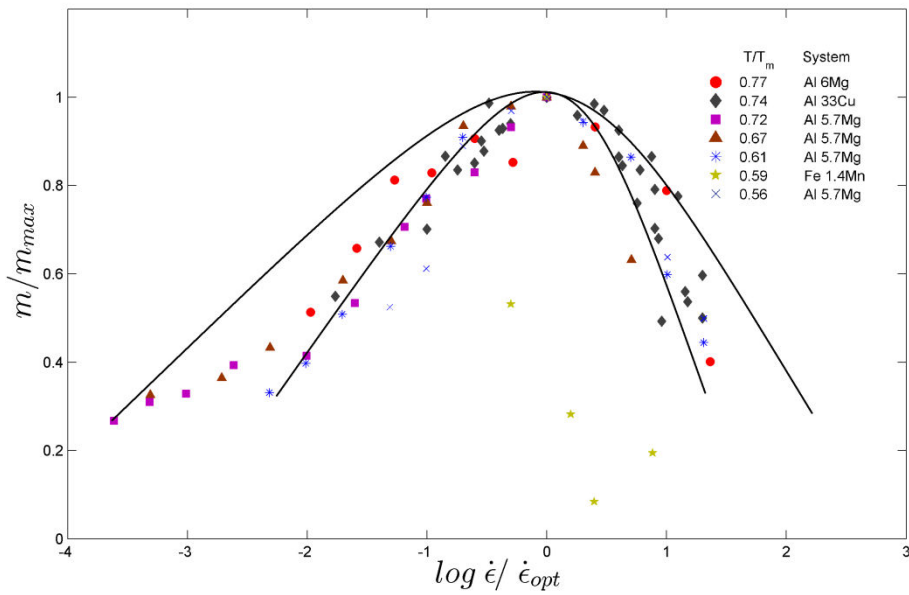


Figure 6.6: Normalized strain-rate sensitivity index v/s versus normalized strain-rate for the systems mentioned in the inset; plotted ignoring the differences in the homologous temperature.

From Figure 6.6 it can be seen that all the data, pertaining to different classes of materials fall within a narrow band. When the homologous temperature differences are considered, the relationship appears as in Figure 6.7.

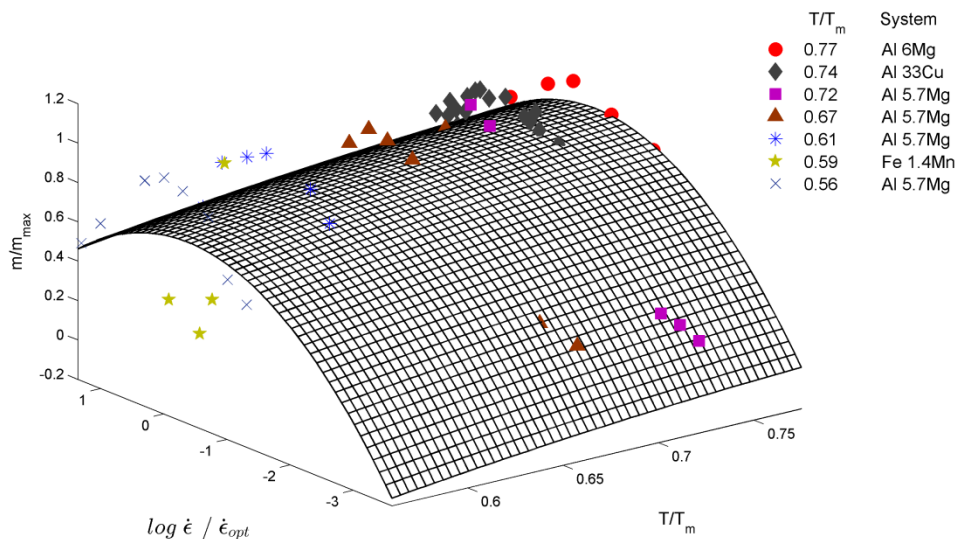


Figure 6.7: Normalized strain rate sensitivity index v/s versus normalized strain-rate v/s versus homologous temperature

The fit presented in Figure 6.7 is defined well by the equation below:

$$f(x, y) = z = -0.56 + 3.82x - 0.07y - 1.81x^2 + 0.02xy - 0.08y^2 \quad 6.10$$

where, $f(x, y) = z$ corresponds to the normalized strain rate sensitivity index, x and y correspond to homologous temperature and normalized $\log(\dot{\epsilon})$ respectively. The coefficient correlation value for this case is 0.80. Sizeable experimental scatter in some systems, experimental data from different sources and more importantly the different methods used to estimate the value of m by the different authors are the key factors that gave rise to a lower value of the correlation coefficient, which still is reasonably good.

Free energy of activation: Historically, Equation 6.3 became a popular way of quantifying superplastic flow because the pioneers, Backofen and coworkers, saw a remarkable similarity between the flow of superplastics and hot polymers and molten glass. As Equation 6.3 was a popular equation in the polymer literature, that got transferred to the superplasticity literature as well (for a summary of the early work, the reader is referred to, for example, [9]). The limitations of this equation, as a description for superplastic flow, were considered in detail in [3]. The most important inadequacies are as follows:

- a) Even when the isothermal stress – strain-rate relationship is presented as a log – log plot, the relationship was not linear; so people tried to divide the full range into several limited ranges to attribute a separate deformation mechanism for each domain- evidently a highly convoluted argument/ way of representation.
- b) More importantly, in the equation (6.3) both the proportionality constant and the strain-rate sensitivity index, m , (or its converse, n , the stress exponent) were functions of the experimental variables of stress, temperature and grain size. From a mathematical point of view, such a description would be regarded as inelegant/ inadequate [3]. (The constant of proportionality is expected to be independent of the variables in a sound formulation).

In chapter 7, after analyzing the experimental data pertaining to 42 superplastic materials, it is shown that a flow mechanism, in which optimal superplastic flow is rate controlled by grain boundary sliding that develops to a mesoscopic level, accounts for the experimental results very accurately. It was pointed out earlier in this chapter that a mathematical formulation of the physical ideas based on the above description results in Equation 6.5. It is easy to see that that equation reduces to a simple constitutive (phenomenological) equation for the isothermal case as Equation 6.11.

$$\dot{\varepsilon} = P_1 \sinh(\sigma - \sigma_0) + P_2 \quad 6.11$$

As for small values of σ , as present during superplastic deformation, $\sinh(\sigma - \sigma_0) \approx (\sigma - \sigma_0)$, Equation 6.11 may be rewritten as:

$$\dot{\varepsilon} = P_1(\sigma - \sigma_0) + P_2 \quad 6.12$$

Ever since the 1940s, when persons like Eyring, Kauzman, Mott, Nabarro and others, came out with the idea of that the temperature dependence of the flow stress (or conversely the flow rate) of a solid obeys the Maxwell-Boltzmann relationship (i.e. the idea of thermally activated complexes got applied to high temperature deformation and the reaction rate theory came into vogue), Arrhenius kinetics has been used to understand high temperature solid state deformation. As can be seen, the temperature dependence of Equation 6.5, which is the basis of Equation 6.11, is in accordance with the Maxwell-Boltzmann relationship. This kind of temperature dependence is true of Equation 6.3 also, which has been used by several authors. In other words, what is stated here is that Equations 6.5 and 6.11 are alternative ways of stating Equation 6.3 and that our analysis in this thesis has shown that they (6.5 and 6.11) describe optimal superplastic flow very accurately.

Therefore, using Equation 6.5, the free energy of activation for the different systems was computed and normalized with respect to (RT_m) , where T_m is the melting point of the system under consideration. (This normalization is based on the well-known fact that the strength of a material, and hence the free energy of activation, is directly dependent on the melting point of the material. The systems considered (see Table 6.3) for analysis were of widely differing compositions, grain sizes and test temperatures and pertained to

two classes, viz. metal-based systems and ceramics. The normalized ($\Delta F_0/RT_m$) values for the different systems are presented in Figures 6.8 and 6.9.

Table 6.3: Details of the systems considered for the analysis

Metallic systems			
	Composition*	L, $\mu\text{m}^\#$	Experimental Temperature, K
1	Zn 22Al ^a [33,34]	2.50	423, 473, 503
2		0.90	398, 453, 518, 545
3	Al 13Si ^a [51]	18.00	791, 811, 831
4	Al 33Cu 0.4Zr ^a [52]	7.60	713, 753, 793
5	Al 17Si 2Fe 2Mg 1Cu 1Ni ^a [53]	1.40	763, 783, 793, 803
6	Al 5.76Mg 0.32Sc 0.3Mn ^a [28]	3.00	723, 748, 773
7	Al 3Mg 0.2 Sc ^a [36]	0.20	573, 623, 673, 723
8	Al 1Mg 0.6Si ^a [54]	2.50	843, 863, 883
9	Al 6Zn 2Mg 1.4 Cu ^a [55]	1.75	753, 773, 793
10	Al 5.76Mg 0.32Sc 0.3Mn ^a [35]	1.0-1.6	523, 573, 623, 673, 723
11	Al 8.9Zn 2.6Mg 0.009Sc ^a [44]	0.68	493, 523, 563, 583, 603
12	Al 5Mg 0.18 Mn 0.2Sc ^a [56]	24.00	748, 773, 793
13	Mg 6Zn 0.8Zr ^a [8]	0.65	473, 498, 523
14	Mg 3Zn 1.5Zr 0.5Y ^c [37]	5.00	648, 673, 698, 723
15	Mg 4Y 0.7Zr 0.4Nd ^a [57]	2.00	598, 623, 648 673
16	Mg 6.19Zn 1.1Y 0.46Zr ^a [58]	5.20	673, 698, 723
17	Mg 5.8Zn 1Y 0.48Zr ^a [46]	15-20	673, 723, 753
18	Ti 48Al ^c [59]	0.90	1163, 1273, 1373

19	Ti 46.8Al 2.2Cr ^c [60]	0.80	1073, 1123, 1173
20	Ti 43Al ^c [48]	5.00	1273, 1323, 1373

21	Ti 6Al 4V ^a [38,61]	0.68	1033, 1113, 1173
22		0.85	
		1.15	
		1.5-2.5	1073, 1123, 1173

23	Cu 2.8Al 1.8Si 0.4Co ^a [45]	7.00	723, 773, 823, 873
24		3.00	673, 723, 773, 823

25	Ni 9Si 3.1V 2Mo ^a [62]	15.00	1323, 1353, 1373
----	-----------------------------------	-------	------------------

26	Co 22Ti ^c [47]	24.00	1173, 1223, 1273
----	---------------------------	-------	------------------

Ceramic systems

27	ZrO ₂ 3Y ₂ O ₃ ^d [63]	0.51	1523, 1573, 1623, 1673, 1723
28	ZrO ₂ 4Y ₂ O ₃ ^d [63]	0.75	
29	ZrO ₂ 3Y ₂ O ₃ ^d [64]	0.50, 0.80, 1.10	1723
30	ZrO ₂ 8Y ₂ O ₃ ^d [65]	0.50	1573, 1623, 1673, 1723, 1773
31	ZrO ₂ [66]	0.065- 0.072	1273, 1323, 1373
32		0.065, 0.110, 0.140	1723
33	ZrO ₂ 8Y ₂ O ₃ ^d [67]	1.10	1573, 1623, 1673, 1723

34	Al ₂ O ₃ 30ZrO ₂ 30Al ₁₆ Si ₂ O ₁₃ ^b [68,69]	0.39	1673, 1723, 1773
35		0.40	
36	Al ₂ O ₃ 25NiAl ₂ O ₄ 25ZrO ₂ ^b [70]	1.30	1623, 1648, 1673, 1698 1723

37	Si ₃ N ₄ 5Y ₂ O ₃ 2Al ₂ O ₃ ^d [71]	0.068	1723, 1773, 1823, 1873
----	---	-------	------------------------

Composition is in ^a weight percent, ^b volume percent ^c atomic percent ^d mole percent

[#]Initial grain size

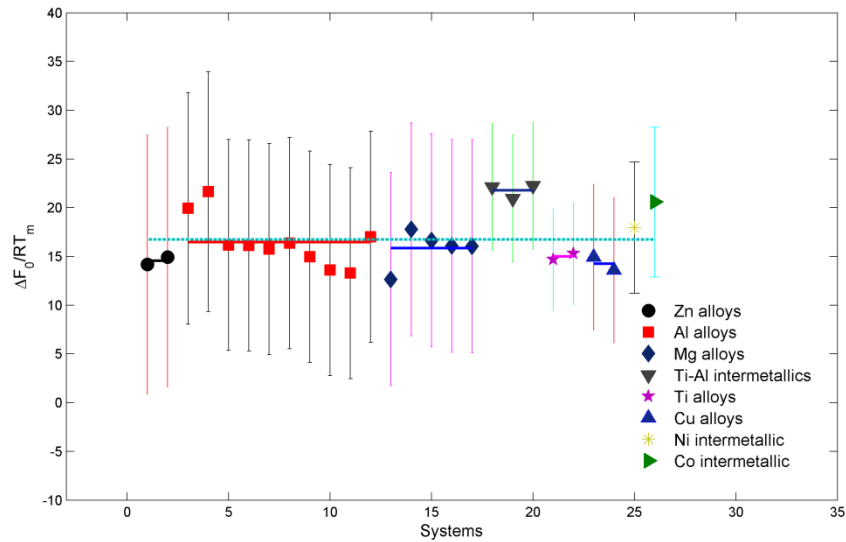


Figure 6.8: Normalized free energy of activation for metallic systems

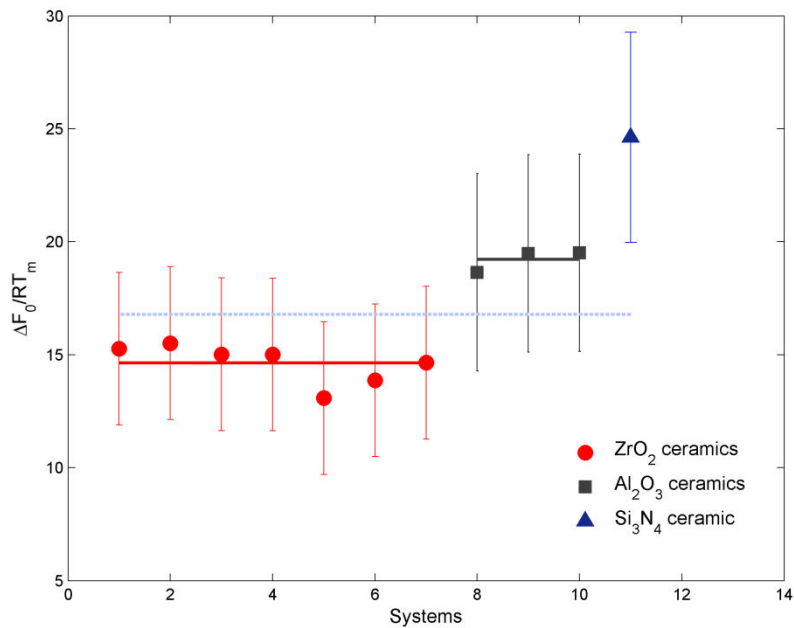


Figure 6.9: Normalized free energy of activation for ceramics

If the underlying physical mechanism responsible for superplastic deformation is the same for all materials, regardless of the class to which they belong, normalizing the free energy of activation for the rate controlling process with respect to (RT_m) (to compensate for the difference in the strength of the interatomic bonds in different materials), should result in fairly close values for all the systems. However, this normalized value could be different for metallic materials and ceramics because in the former the bonds are metallic in nature, while in the latter the bonds are either covalent or ionic, which are stronger than the metallic bonds. The commonly reported minimum error in the experimental estimates for the free energy of activation [72] is $42 \text{ kJ}\cdot\text{mol}^{-1}$. The same has also been normalized with respect to (RT_m) and an error band is associated with each of the (ΔF_0) values in Figures 6.8 and 6.9. It can, therefore, be concluded that the normalized values of the free energy of activation for the different systems are comparable, definitely so long as the nature of the inter-atomic bonds is the same.

Indeed it could be argued that the universality of the $(\Delta F_0/RT)$ relationship seems to transcend the differences between the metallic materials and ceramics, if one were to take into account the maximum accuracy possible in the experimental measurements of the activation energy. Again, it has been suggested in the literature that under pressure the

nature of the atomic bonds in ZrO_2 becomes very similar to the metallic. It is interesting that the values of the $(\Delta F_0/RT)$ for this ceramic material is very close to the values obtained for the metallic materials. In contrast, the values obtained for Al_2O_3 and Si_3N_4 ceramics, where the covalent bonding is stronger, are greater, which is in agreement with the ideas proposed above.

Therefore, it is suggested that there is a case to conclude that there is universality in the phenomenology of superplastic deformation, i.e. the formalism 6.1, which suggests universality in a normalized 5 dimensional hyper-space, appears to be meaningful. This, in turn, justifies the quest for identifying a common rate controlling physical mechanism for optimal superplastic flow, which is the subject of the next chapter.

7. Mesosopic-grain boundary sliding controlled flow model

The mesoscopic-grain boundary sliding controlled flow for superplastic deformation, described in chapter 5, was used to interpret optimal superplastic behavior in different classes of materials and the findings are described in this chapter.

A broad overview on the constitutive equations proposed in the literature for superplastic deformation was also presented in chapter 5. In this chapter, it is concluded after a detailed analysis that a constitutive equation of the form,

$$\dot{\epsilon} = P_1 \sinh(\sigma - \sigma_0) + P_2 \quad 7.1$$

adequately describes isothermal, steady state, optimal superplastic deformation (i.e. starting from the lowest strain-rate till the point of inflection in the isothermal sigmoidal $\log(\sigma) - \log(\dot{\epsilon})$ relationship) of materials of constant microstructure (defined in terms of an average grain size). It is to be noted that both P_1 and P_2 are constants, independent of σ and $\dot{\epsilon}$. This equation is a much simpler form of the constitutive equation compared with the commonly used $\dot{\epsilon} = K\sigma^n$, in which both K and n are functions of the experimental variables like stress/ strain-rate, even under isothermal, constant grain-size conditions. As a result, even an isothermal, isostructural plot of $\log(\dot{\epsilon}) - \log(\sigma)$ appears sigmoidal over a large strain-rate range (and quadratic within the optimal range of superplastic deformation). In contrast, Equation 7.1, with the use of the fact that $\sinh(x) \approx x$ suggests that there is a linear relationship between the strain rate and an “effective” stress, $(\sigma - \sigma_0)$, with σ_0 a physically meaningful constant – the threshold stress necessary for the onset of mesoscopic boundary sliding. This form of equation is well analyzed in the literature on Mechanics of Solids and the behavior is said to belong to a Bingham Solid. In this view, the mechanical response observed during steady state isothermal, iso-structural superplastic flow is akin to that of a Bingham Solid [3]. This has implications for the development of a concept of “frame of reference indifference” for superplasticity, as has already been done for plasticity, e.g. the von Mises yield criterion. This aspect is beyond the scope of the present thesis and will be considered elsewhere.

For this analysis, a total of 42 systems, vastly differing in composition and grain-size and belonging to different materials classes, were chosen. Table 7.1 presents the details of the systems chosen for the analysis, along with the values of the activation energy for the (strain) rate controlling process(es), as suggested in the original papers (wherever available). In these cases, a brief description of the analytical procedures used by the authors is also given.

The analytical procedure used and the algorithm on which the computer program was written by this author for the present purpose is discussed below, in §7.1.

7.1 Algorithm

A main aim of this investigation is the validation of the m-GBS model using the large amounts of experimental data available in the literature. For this exercise to involve many systems for which one could get dependable data and also to be completed in quick time, a computer program had to be written. The first step in this direction is the writing down of an algorithm, which will outline the procedure to be followed. The algorithm begins with an approximate estimation of the value for the free energy of activation for the rate controlling process using Equation 7.2. (The equations pertaining to the m-GBS model are already given in Chapter 5. But, for the ease of reference they are included at relevant places.)

$$\Delta F_0 = (\beta_1 \gamma_0^2 + \beta_2 \varepsilon_0^2) G V_0 \quad 7.2$$

where,

$$\beta_1 = 0.944 \frac{1.59 - p}{1 - p}, \quad \beta_2 = \frac{4(1 + p)}{9(1 - p)}, \quad (\text{for an oblate spheroid})$$

The value of the unit shear strain is initially assumed to be 0.1 (based on bubble raft experiments and MD simulations) [30,31]. The tolerance, which quantifies the accuracy in the predictions, is defined as the larger ratio between $(\dot{\varepsilon}_{\text{pred}} / \dot{\varepsilon}_{\text{expt}})$ and $(\dot{\varepsilon}_{\text{expt}} / \dot{\varepsilon}_{\text{pred}})$.

Although predictions are considered to be satisfactory if they are within an order of magnitude (i.e., tolerance < 10), almost all the predictions here are well within an order of magnitude (far below 10) and most of them are close to 1 (near exact fits). Figure 7.1 presents the algorithm developed for the validation of the m-GBS model. Most part of the algorithm is automated. The input data of stress, strain-rate and grain size are taken from the experimental results and the material properties of atomic diameter, shear modulus and its variation with temperature are taken from the well known compilation of Frost and Ashby [13]. As the strain-rate equation is transcendental, it can only be solved numerically. Therefore, the tolerance and the number of iterations necessary for convergence to a solution of pre-defined accuracy are determined manually for each system. In addition, the experimental points relevant to the analysis (i.e., from the lowest strain rate till the point of inflection in the isothermal $\log(\sigma) - \log(\dot{\epsilon})$ plots) were chosen manually for each system.

Data Preprocessing: An important consideration prior to the analysis is the choice of the data for the analysis. Minimum number of temperatures (or grain-sizes), at which the experimental data are to be available is 3. Such a data set is essential to compute the values of free energy of activation for the rate controlling process confidently, because this parameter is assumed to be independent of temperature (Arrhenius kinetics) and experimental data at a minimum of 3 temperatures are needed for obtaining a dependable linear fit between $\log(\dot{\epsilon})$ and $1/T$. The larger the number of data points at different temperatures or grain-sizes, the more suitable would a system be for the analysis. As stated earlier, the m-GBS model is applicable from the slowest strain rate till the point of inflection in the isothermal $\log(\dot{\epsilon}) - \log(\sigma)$ curve. Data from this range only (if data beyond were also reported) were manually extracted. With regard to material properties, the melting temperature and the shear modulus are available for most of the materials analyzed from the relevant phase diagrams and handbooks. The dependence of the shear modulus on temperature was not available for many cases. In such cases, following the suggestion of Frost and Ashby [13], the variation of G with respect to T for the base material/ principal constituent was used, as an approximation. Experimental values of Poisson's ratio were available for quite a few cases, while for the rest, the Poisson's ratio was assumed to be 0.33 [73]. The atomic diameters required for the calculations were

taken as those of the elements that formed the largest constituent of the alloy/ material [74].

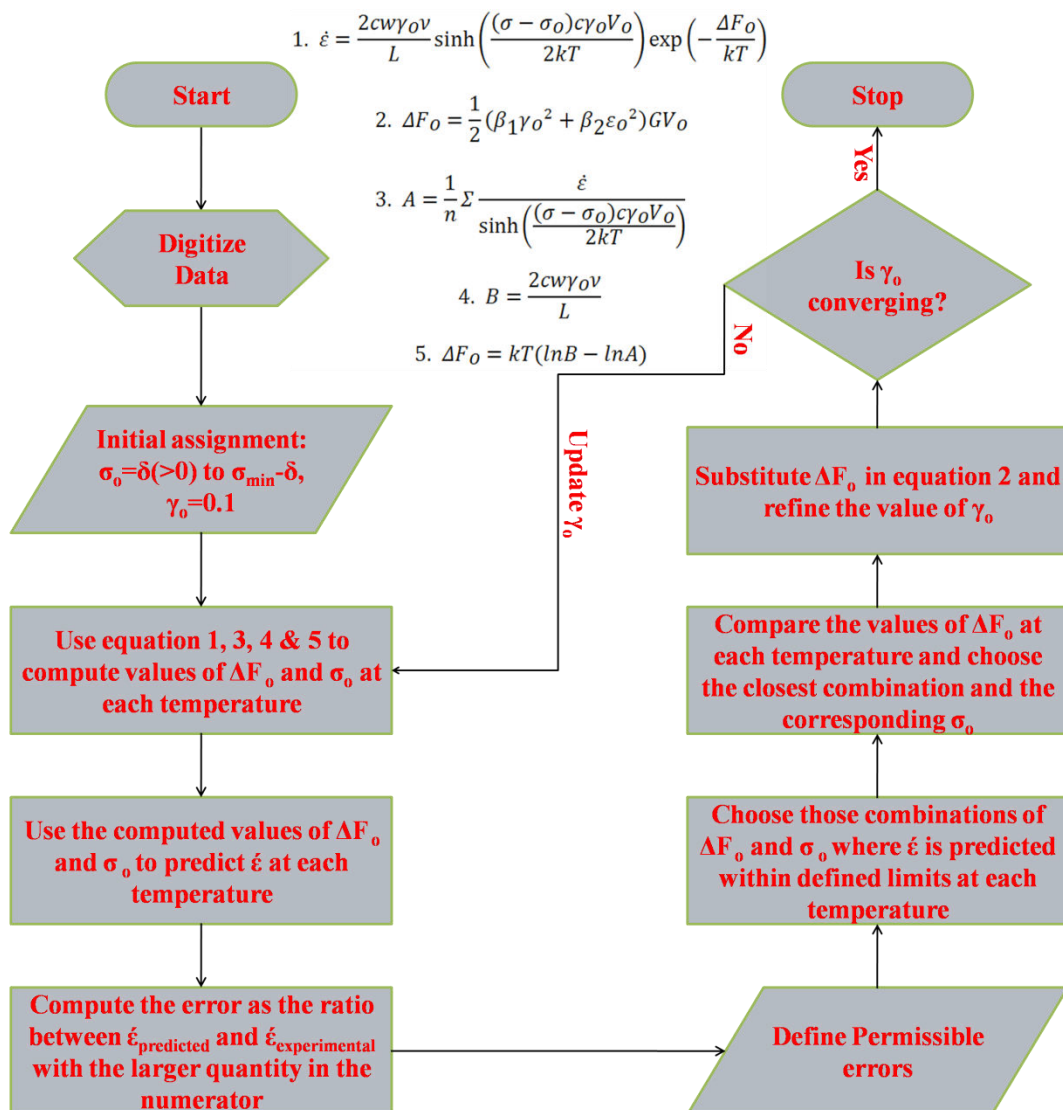


Figure 7.1: Flowchart describing the algorithm; equations used are presented inside the frame

Description of the Algorithm: Figure 7.1 is a flow chart showing the manner in which the computations are carried out. Equations 7.2 and 7.3 constitute two essential equations of the analysis: Using these equations, ΔF_0 and σ_0 are the two unknowns to be computed for different systems at each temperature.

$$\dot{\epsilon} = \frac{2cW\gamma_0v}{L} \sinh\left(\frac{(\sigma - \sigma_0)c\gamma_0V_0}{2kT}\right) \exp\left(-\frac{\Delta F_0}{kT}\right) \quad 7.3$$

For achieving this goal, the following steps are followed.

1. Initially γ_0 is assigned a value of 0.1 [26,75], which is later refined (see below for details). The material is assumed to obey the von Mises yield criterion (for determining the relation between the shear and normal yield stresses and the corresponding strains/ strain rates).
2. At each temperature, evidently, the value of σ_0 should be less than the lowest value of stress applied at that temperature in the experiments where a strain rate has been measured (as the threshold stress has to be below this stress for flow to take place). Hence, σ_0 is assigned values from δ to $\sigma_{\min} - \delta$. To ensure accurate calculations, δ was chosen as 0.001 and the increment at every step was also kept as $0.001\sigma_{\min}$.
3. The following substitution is made into Equation 7.3:

$$A = \frac{1}{N} \sum \frac{\dot{\epsilon}}{\sinh\left(\frac{(\sigma - \sigma_0)c\gamma_0V_0}{2kT}\right)}$$

Therefore, at each temperature values of ΔF_0 corresponding to each value of σ_0 , as defined in step 2, could be computed.

4. Computed values of σ_0 and ΔF_0 are used along with the experimental stress values at different temperatures in Equation 7.3 and the strain rates are predicted.
5. The error is defined as the larger value between $(\dot{\epsilon}_{\text{pred}} / \dot{\epsilon}_{\text{expt}})$ and $(\dot{\epsilon}_{\text{expt}} / \dot{\epsilon}_{\text{pred}})$. The error in prediction for each of the σ_0 and the corresponding ΔF_0 value is computed.
6. A maximum value of error (which was less than 10 for all the systems and less than 5 for most of the systems) is defined for each system. This was a manual process; a physical restriction associated with the choice of the permitted value for the error is that the threshold stress has to decrease with increasing temperature.
7. Among these, the ΔF_0 value which was the closest at all the temperatures, and the corresponding σ_0 values were chosen. This ensured that the ΔF_0 value was nearly independent of temperature, as required by Arrhenius kinetics.

8. The calculated value of ΔF_0 was substituted in Equation 7.2 and the value of γ_0 was iterated to get the exact value for the given experimental results. As the ΔF_0 value varies as γ_0^2 , the deviation of γ_0 from the initial value of 0.1 is not likely to be (and was not) very large.
9. Replacing the γ_0 value by the refined value obtained in step 8, steps 1 to 8 were followed iteratively till the values of γ_0 converged and a near stable value was obtained.

To study the meaningfulness of the analysis and the accuracy of predictions, the standard deviation, average error and correlation coefficient were calculated by comparing the experimental results against the predictions of Equations 7.4.

$$SD = \left(\frac{\sum (\dot{\epsilon}_{\text{expt}} - \dot{\epsilon}_{\text{pred}})^2}{n - 2} \right)^{0.5}$$

$$AE = SD/n^{0.5}$$

7.4

$$CC = \frac{\sum \dot{\epsilon}_{\text{expt}} \dot{\epsilon}_{\text{pred}} - n \dot{\epsilon}_{\text{m, expt}} \dot{\epsilon}_{\text{m, pred}}}{\left(\sum \dot{\epsilon}_{\text{expt}}^2 - n \dot{\epsilon}_{\text{m, expt}}^2 \right) \left(\sum \dot{\epsilon}_{\text{pred}}^2 - n \dot{\epsilon}_{\text{m, pred}}^2 \right)}$$

It will be seen below that all the systems analyzed gave rise to excellent correlations with the experimental results.

Table 7.1 classifies all the simple systems analyzed based on the principal constituent. The geological materials (rocks/ minerals) and ice (glacial) are grouped together. Even a cursory glance of the Table brings home the significant differences in the values of the activation energy reported in the literature for the rate controlling process even in alloys of similar/ very close compositions. It is not easy to explain this observation easily, without proposing some exotic/ esoteric effects of very minor additions. Therefore, a case could be made that this is evidence for a lack of robustness in the analytical procedures used by these authors.

Table 7.1: Details of the systems considered for the analysis

	Composition*	L, $\mu\text{m}^\#$	Reported values of	
			T, K	Q, $\text{kJ}\cdot\text{mol}^{-1}$

1	Zn 22Al ^a [33,34]	2.50	423, 473, 503	-
2		0.90	398, 453, 518, 545	-

3	Al 13Si ^a [51]	18.00	791, 811, 831	132-137 [‡]
4	Al 33Cu 0.4Zr ^a [52]	7.60	713, 753, 793	-
5	Al 17Si 2Fe 2Mg 1Cu 1Ni ^a [53]	1.40	763, 783, 793, 803	-
6	Al 5.76Mg 0.32Sc 0.3Mn ^a [28]	3.00	723, 748, 773	190
7	Al 3Mg 0.2 Sc ^a [36]	0.20	573, 623, 673, 723	120 ^e , 95 [†]
8	Al 1Mg 0.6Si ^a [54]	2.50	843, 863, 883	78-556 [‡]
9	Al 6Zn 2Mg 1.4 Cu ^a [55]	1.75	753, 773, 793	-
10	Al 5.76Mg 0.32Sc 0.3Mn ^a [35]	1.0-1.6	523, 573, 623, 673, 723	-
11	Al 8.9Zn 2.6Mg 0.009Sc ^a [44]	0.68	493, 523, 563, 583, 603	142
12	Al 5Mg 0.18 Mn 0.2Sc ^a [56]	24.00	748, 773, 793	-

13	Mg 6Zn 0.8Zr ^a [8]	0.65	473, 498, 523	-
14	Mg 3Zn 1.5Zr 0.5Y ^c [37]	5.00	648, 673, 698, 723	108-146
15	Mg 4Y 0.7Zr 0.4Nd ^a [57]	2.00	598, 623, 648 673	126
16	Mg 6.19Zn 1.1Y 0.46Zr ^a [58]	5.20	673, 698, 723	92
17	Mg 5.8Zn 1Y 0.48Zr ^a [46]	15-20	673, 723, 753	76, 213 [‡]

18	Ti 48Al ^c [59]	0.90	1163, 1273, 1373	240
19	Ti 46.8Al 2.2Cr ^c [60]	0.80	1073, 1123, 1173	220

20	Ti 43Al ^c [48]	5.00	1273, 1323, 1373	390
----	---------------------------	------	------------------	-----

21	Ti 6Al 4V ^a [38,61]	0.68	1033, 1113, 1173	150, 240
		0.85		
		1.15		
22		1.5-2.5	1073, 1123, 1173	-

23	Cu 2.8Al 1.8Si 0.4Co ^a [45]	7.00	723, 773, 823, 873	203 region I
24		3.00	673, 723, 773, 823	120 region II

25	Ni 9Si 3.1V 2Mo ^a [62]	15.00	1323, 1353, 1373	555
----	-----------------------------------	-------	------------------	-----

26	Co 22Ti ^c [47]	24.00	1173, 1223, 1273	80
----	---------------------------	-------	------------------	----

27	ZrO ₂ 3Y ₂ O ₃ ^d [63]	0.51	1523, 1573, 1623, 1673, 1723	533
28	ZrO ₂ 4Y ₂ O ₃ ^d [63]	0.75		
29	ZrO ₂ 3Y ₂ O ₃ ^d [64]	0.50, 0.80, 1.10	1723	-
30	ZrO ₂ 8Y ₂ O ₃ ^d [65]	0.50	1573, 1623, 1673, 1723, 1773	341, 411 [‡]
31	ZrO ₂ [66]	0.065- 0.072	1273, 1323, 1373	350 [‡]
32		0.065, 0.110, 0.140	1723	
33	ZrO ₂ 8Y ₂ O ₃ ^d [67]	1.10	1573, 1623, 1673, 1723	597, 683 [‡]

34	Al ₂ O ₃ 30ZrO ₂ 30Al ₁₆ Si ₂ O ₁₃ ^b	0.39	1673, 1723, 1773	911, 840 [‡]
----	---	------	------------------	-----------------------

35	[68,69]	0.40		870
36	Al_2O_3 25NiAl ₂ O ₄ 25ZrO ₂ ^b [70]	1.30	1623, 1648, 1673, 1698 1723	377, 368 [‡]

37	Si_3N_4 5Y ₂ O ₃ 2Al ₂ O ₃ ^d [71]	0.068	1723, 1773, 1823, 1873	853 region I 572 region II
----	--	-------	------------------------	-------------------------------

38	San Carlos Olivine [76]	5.40	1423, 1473, 1523	445
39	Limestone [77]	4.20	973, 1073, 1173	210.87
40	Anorthite-Diopside, dry ^g [78]	3.05	1323, 1373, 1473	571
41	Anorthite-Diopside, wet ^g [78]	3.05	1273, 1323, 1373, 1473	363
42	Fine grained ice [79]	10.00	199, 219, 220	49

Composition is in ^a weight percent, ^b volume percent ^c atomic percent ^d mole percent
^e RCM is dislocation climb, ^f RCM is dislocation glide, ^g Anorthite and Diopside are
minerals with compositions $\text{CaAl}_2\text{Si}_2\text{O}_8$ and $\text{MgCaSi}_2\text{O}_6$ respectively

[#]Initial grain size

[‡] At the highest and the lowest experimental stress respectively

The initial average grain sizes of all the 42 systems analyzed in this study are also given in Table 7.1. These values are used in subsequent calculations without repeating them. It is interesting that these grain sizes themselves are good enough to ensure a good accuracy of predictions. This brings home the relative stability of the grain size during optimal superplastic deformation in the strain range within which the stress – strain rate relationships are determined. A few more details are presented along with the analysis.

7.2 Zinc-based alloys

Two zinc-based alloys from Refs. [33,34] were analyzed. The details are as follows: the temperature range 423 K - 545 K; grain size range, 0.9 μm - 2.5 μm ; maximum strain rate

sensitivity index, ~ 0.51 ; stress range, 12.49 MPa - 988.38 MPa; strain-rate range $134.60 \times 10^{-6} \text{ s}^{-1}$ - $11.04 \times 10^{-6} \text{ s}^{-1}$; maximum reported elongation $\sim 3000\%$. Neither of the investigators has reported results/ analyses regarding the RCM or activation energy. A relevant observation is that Ref. [34] reports a maximum strain rate sensitivity of 0.51 at a grain size of 0.9 μm and 0.15 at a grain size of 145 μm for the same Zn 22Al alloy. This clearly demonstrates the importance of a fine grain size for obtaining significant superplastic deformation.

Results of the analysis: Table 7.2 presents the detailed results for the zinc-based systems. Although a constant value for the free energy of activation is expected at all temperatures, due to the iterative/ numerical (not exact) solutions obtained here, the value computed at each temperature was slightly different. However, it is noteworthy that the scatter in the values of the free energy of activation for each system was much less than 42 kJ.mol^{-1} , which is the commonly reported minimum error in the experimental estimates for the free energy of activation [72]. Hence an average of these slightly varying values of the free energy of activation is reported in Table 7.2.

Table 7.2: Details of the strain-rate predictions using the m-GBS model

System*	T, K	ΔF_0 kJ.mol ⁻¹	γ_0	σ_0 MPa	MT	SD	AE	CC
1	423	89.8	0.0864	26.941	4.72	0.1048	0.0349	0.9996
	473		0.0915	15.809	5.03	0.0968	0.0323	0.9816
	503		0.0941	12.2619	6.31	0.0961	0.032	0.9742
2	398	94.1	0.0846	20.9728	1.55	0.0245	0.0061	0.9176
	453		0.0906	6.2012	2.27	0.0269	0.0063	0.9398
	518		0.0982	2.9179	2.35	0.0287	0.0068	0.9607
	545		0.0997	2.9165	2.82	0.0339	0.0098	0.9761

* For composition of the respective systems, refer Table 7.3, presented below

Tolerance, in this context is defined as the ratio of the predicted strain-rate to the experimental strain-rate or the experimental strain-rate to the predicted strain-rate, whichever is larger. In order of magnitude calculations, results are considered to be satisfactory if the error is within an order of magnitude or the maximum tolerance is less than 10. From Table 7.2 it can be seen that the maximum tolerance, MT, is much less than 10 in all the cases and in fact, in some cases, where the experimental data were consistent, the predictions are extremely accurate.

Further, the statistical parameters of the analysis (Average error, Correlation coefficient, and Standard deviation) reveal that very good predictions are obtained when the experimental data are analyzed using the m-GBS model.

According to the m-GBS model, the threshold stress for the onset of mesoscopic boundary sliding, σ_0 , should decrease with increasing temperature and the unit shear strain, γ_0 , should increase with increasing temperature. From Table 7.2 it is seen that both the threshold stress and the unit shear strain are following the expected trends for both the systems.

A description about the different constitutive equations available in the literature was presented in Chapter 5 and in this thesis a simple constitutive equation is suggested for optimal superplastic flow (Equation 7.1). Table 7.3 presents the results of the fitting of the data using a constitutive equation of the form $y=Mx+c$ (where $y=\dot{\epsilon}$, $M \sim P_1$, $x \sim \sinh(\sigma-\sigma_0)$, $c \sim P_2$). The threshold stress, σ_0 , as predicted by the m-GBS system, is to be used in Equation 7.1.

Good values for the correlation coefficient could be obtained by fitting the experimental data using Equation 7.1. Table 7.3 presents the results. Evidently, Equation 7.1 describes optimal superplastic deformation very adequately.

Table 7.3: Fitting constants and the correlation coefficient for Equation 7.1

System	T_{hom}^*	Fitting constants		CC
		$P_1 \times 10^{-3}$	$P_2 \times 10^{-3}$	
1	0.5580	120.5447	-8.739	0.98
	0.6240	188.6957	-5.799	0.97
	0.6636	282.7686	-5.5337	0.97
Zn 22Al	0.5251	57.7683	-1.0009	0.91
	0.5976	126.0347	-0.8505	0.94
	0.6834	257.5193	-1.0708	0.96
2	0.7190	680.462	-1.8874	0.98

* Homologous temperature, $T_{\text{hom}}=T/T_m$; T is the experimental temperature, T_m is the melting temperature

Experimental strain rates and the strain rates predicted using the m-GBS model are presented in Figures 7.2 and 7.3 for the zinc-based alloys.

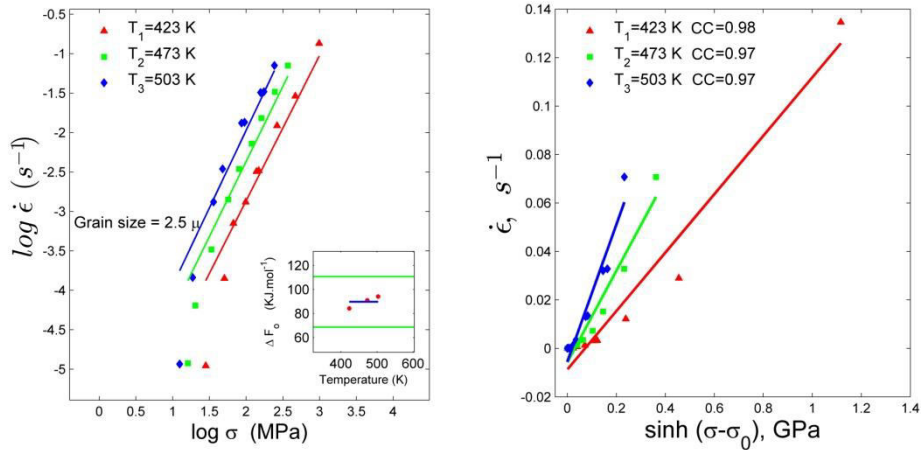


Figure 7.2: Strain rate predictions and $\dot{\epsilon}$ versus $\sinh(\sigma-\sigma_0)$ plot for system 1

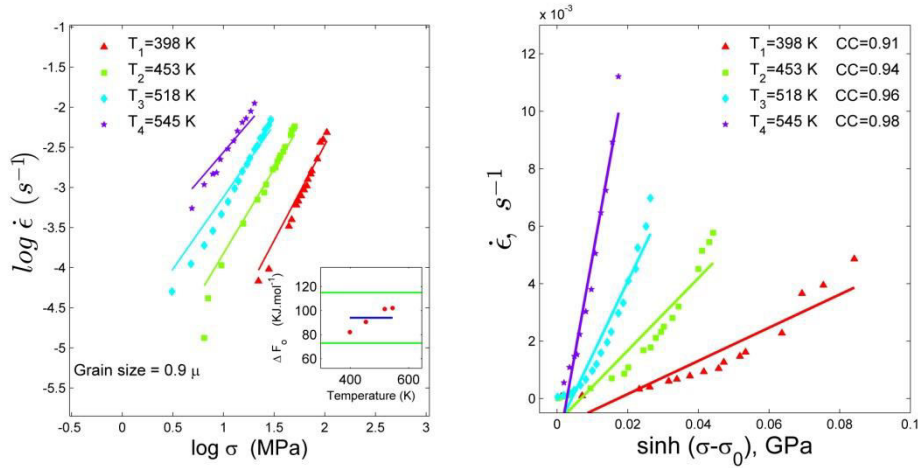


Figure 7.3: Strain rate predictions and $\dot{\epsilon}$ versus $\sinh(\sigma-\sigma_0)$ plot for system 2

7.3 Aluminum-based alloys

Ten aluminum-based alloys were analyzed [28,35,36,44,51–56]. Some systems, in fact, exhibited high strain rate superplasticity. Relevant experimental parameters are: experiments were performed in a temperature range of 493 K - 883 K; in a grain size range of 0.2 μm - 24 μm ; maximum reported values for m and elongation were ~ 0.7 and $\sim 2500\%$, respectively; strain-rate range $1.10 \times 10^{-6} \text{ s}^{-1}$ - $1.47 \times 10^{-6} \text{ s}^{-1}$; stress range 0.62 MPa - 0.95 GPa.

Equation 7.5 represents a general form very often used to describe superplastic behavior. The authors of Ref. [51] have tabulated the values of the parameters of Equation 7.5 from

earlier investigations. The parameters vary significantly from one model to another. While p varies from 0 to 3, n varies from 1 to 4.4, A , however, varies from $\sim 10^{-11}$ to 10^6 . These values are a far cry from the claim that A and n are constants. This raises some doubts about the physical meaning of Equation 7.5, particularly because in Regions I and IIa of isothermal steady state superplastic deformation (optimal range) itself the values of A and n vary significantly.

$$\dot{\epsilon} = \frac{ADGb}{kT} \left(\frac{b}{L}\right)^p \left(\frac{\sigma}{G}\right)^n \quad 7.5$$

Ref. [51] calculates the threshold stress by extrapolating the σ versus $\dot{\epsilon}$ to zero $\dot{\epsilon}$. The dominant deformation mechanisms are suggested to be dislocation climb in the high stress region and grain boundary sliding accommodated diffusion at intermediate and low stress levels. Ref. [28] believes that the conversion of sub-grain boundary to true high-angle grain boundary occurs in the early stages of deformation. Once high-angle grain boundaries are formed, grain boundary sliding takes over as the dominant deformation process. They propose a model wherein GBS is accommodated by dislocation glide across the grains. Dislocation glide is suggested as the RCM. The model reduces to Equation 7.6. (The suggestion of dislocation glide as the rate controlling process cannot be reconciled easily with the very high (far more than 0.3) values of m seen during superplastic flow, notwithstanding the claim of the authors. Also, the activation energy needed for dislocation glide would be far greater than what has been reported experimentally.)

$$\dot{\epsilon} = B_{\text{gbs.glide}} \frac{1}{d} \sigma^2 \quad 7.6$$

Ref. [36] begins by citing the *standard theories of creep (and assuming them to be applicable for superplasticity also)* that when $p = 2$, $n = 2$ in Equation 7.5, climb of dislocations would be the rate controlling process and when $p = 2$, $n = 1$, glide of dislocations across the grains becomes the rate controlling process. Accordingly, the investigators evaluated the respective activation energy as the slope of $1/T$ versus σ^2/d^2GT , ($= 120\text{kJ.mol}^{-1}$) when dislocation climb is the rate controlling process and the

slope of $1/T$ versus σ^2 / d^2T , ($= 95\text{kJ}\cdot\text{mol}^{-1}$) when dislocation glide is the rate controlling process, at a strain rate of $1 \times 10^{-2} \text{ s}^{-1}$. (Evidently, the activation energy values computed are apparent values and do not conform to the requirements of Arrhenius kinetics, where $\log \dot{\epsilon}$ is plotted against $(1/T)$ at constant stress σ or more correctly at constant σ^n [15,80]. The activation energies reported by the authors correspond to activation energy at constant strain rate – an apparent value. Yet, speculations about the RCMs have been made based on these values). The values of activation energy so computed are compared with the values of the activation energy for grain boundary diffusion for pure aluminum ($\approx 87\text{kJ}\cdot\text{mol}^{-1}$ [81]) and the activation energy for inter-diffusivity in Al-Mg solid solution alloys ($\approx 130.5\text{kJ}\cdot\text{mol}^{-1}$ [82]). As the strain rate at which the activation energies were calculated lies in region II of the sigmoidal $\log \sigma$ versus $\log \dot{\epsilon}$ curve and the activation energy for dislocation glide is close to that for conventional aluminum alloys, dislocation glide was suggested as the probable RCM. Ref. [54] extrapolates σ versus $\dot{\epsilon}^{0.5}$ curve towards zero strain-rate to determine the value of the threshold stress. With such a calculated value for the threshold stress, activation energy is calculated as the slope of $\log((\sigma - \sigma_0)/E)$ versus $1/T$, at a constant strain rate. However, it is to be noted that while reporting the values of activation energies, the investigators, instead of considering the approximate slope involving all the experimental temperatures, as is usually done, have reported activation energies between every two temperatures, as shown in Figure 7.4.

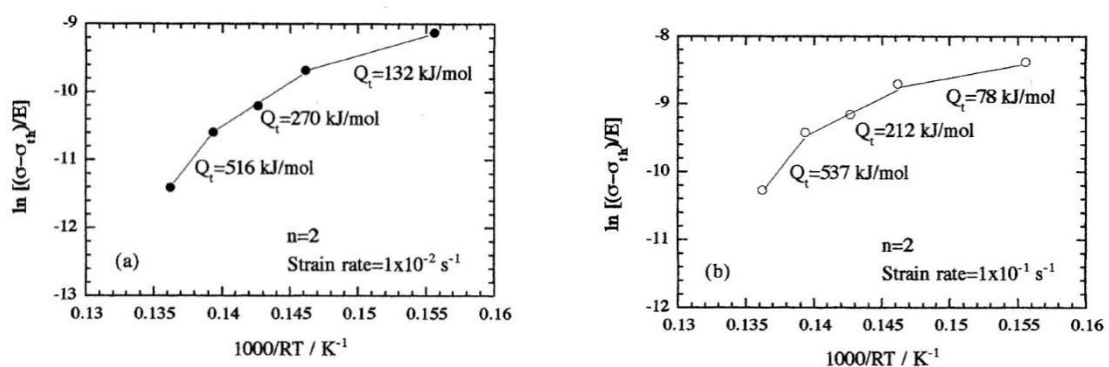


Figure 7.4: Activation energies reported in Ref. [54]

(As the region II of the sigmoidal curve is almost linear, same activation energy has been reported for second and third, third and fourth temperatures.)

Ref.[44] suggests *Rachinger GBS* as the plausible deformation mode with impurity-controlled or interface controlled flow [50]; $p = 1$ and $n = 3$ in Equation 7.5. Furthermore, the paper reports the value of the Constant A in Equation 7.5 as ~ 7100 and replaces shear modulus in Equation 7.5 with Young's modulus and reports another value for A, as $\sim 5.1 \times 10^6$. A better fit is said to emerge when the stress is normalized with respect to the Young's modulus, instead of the shear modulus. Investigators of [56] report near complete transformation of grain boundaries to high-angle types during the course of superplastic deformation. Average misorientation angle of 27.8° , prior to deformation, increased to 41.5° after deformation. Apart from the shortcomings already pointed out, the use of Equation 7.5 – originally proposed when n is a constant independent of stress and temperature, the activation energy for the rate controlling process also is independent of stress and temperature and nearly equal to the activation energy for bulk diffusion [15] to obtain some phenomenological constants empirically and venturing to speculate about the RCMs at the level of atomistics, to say the least, should be viewed with considerable caution. Topological and microstructural support for the mechanisms suggested is completely missing.

Results of the analysis: Table 7.4 presents the results for the aluminum-based systems analyzed and Table 7.5 presents the constants calculated using the constitutive equation, Equation 7.1 (m-GBS model).

Table 7.4: Details of the strain-rate predictions using the m-GBS model

System	T, K	ΔF_0 kJ.mol ⁻¹	γ_0	σ_0 MPa	MT	SD	AE	CC
1	791	140.1	0.1269	0.5574	1.58	0.0134	0.0060	0.9248
	811		0.1290	0.5127	1.59	0.0117	0.0052	0.9570
	831		0.1309	0.5125	2.06	0.0160	0.0080	0.9614
2	713	147.7	0.1268	1.4450	1.08	0.0025	0.0011	0.9955
	753		0.1302	0.6743	1.10	0.0028	0.0014	0.9971
	793		0.1324	0.4564	1.24	0.0040	0.0020	0.9975
3	763	125.4	0.1039	13.8053	3.33	0.5662	0.2831	0.9732
	783		0.1049	7.5482	4.36	0.5351	0.2675	0.9886
	793		0.1050	4.9204	4.57	0.5546	0.2773	0.9861
	803		0.1077	1.7177	7.75	0.1623	0.0726	0.8527
4	723	125.1	0.0694	4.2063	2.04	0.0591	0.0209	0.9564
	748		0.0707	3.3671	2.80	0.0703	0.0287	0.9529
	773		0.0721	2.0719	5.84	0.0664	0.0235	0.9772
5	573	122.4	0.1058	11.2734	1.57	0.0719	0.0294	0.9843

	623		0.1083	7.6555	2.00	0.0671	0.0300	0.9957
	673		0.1140	3.4066	2.73	0.0773	0.0316	0.9806
	723		0.1176	3.1563	3.33	0.0719	0.0322	0.9901
	843		0.1219	6.0819	2.13	0.3745	0.1872	0.9782
6	863	127.0	0.1221	1.7782	2.66	0.3909	0.1954	0.9737
	883		0.1235	0.7507	2.77	0.3942	0.1971	0.9813
	753		0.1119	9.5650	1.98	0.4211	0.1489	0.9861
7	773	116.1	0.1139	6.4640	2.19	0.3179	0.1124	0.9949
	793		0.1141	4.4559	2.73	0.3728	0.1409	0.9752
	523		0.0602	30.5027	1.22	0.0136	0.0068	0.9897
	573		0.0616	12.936	1.50	0.0260	0.0106	0.9798
8	623	105.4	0.0620	12.9328	1.60	0.1569	0.064	0.9812
	673		0.0633	9.5460	1.83	0.2591	0.0916	0.9918
	723		0.0644	9.4378	2.11	0.4201	0.1715	0.9899
	493		0.0960	36.9828	1.36	0.0851	0.0381	0.9653
	523		0.0978	28.0178	2.23	0.0754	0.0377	0.973
9	563	103.1	0.0995	13.9243	2.54	0.2098	0.0793	0.8952
	583		0.1005	10.2616	3.44	0.3078	0.1088	0.955
	603		0.1023	6.7804	3.68	0.2165	0.0818	0.8897
	748		0.0719	23.5183	1.26	0.0257	0.0115	0.9879
10	773	132.0	0.0734	15.5946	1.31	0.0247	0.0111	0.9888
	793		0.0745	11.9544	1.39	0.0221	0.0099	0.9896

* For composition of the respective systems, refer Table 7.5, presented below

Table 7.5: Fitting constants and the correlation coefficient for Equation 7.1

System	T_{hom}	Fitting constants		CC
		$P_1 \times 10^{-3}$	$P_2 \times 10^{-3}$	
1 Al 13Si	0.9306	321.0393	-0.0812	0.92
	0.9541	323.5111	-0.0670	0.95
	0.9776	455.094	-0.1324	0.96
2 Al 33Cu 0.4Zr	0.8685	14.9311	-0.0053	0.99
	0.9172	33.0183	-0.0042	0.99
	0.9659	110.241	-0.0098	0.99
3 Al 17Si 2F3 2Mg 1Cu 1Ni	0.8178	20276.6	-109.688	0.97
	0.8392	26488.94	-74.5992	0.98
	0.8499	44276.12	-93.7011	0.98
	0.8607	22753.08	-15.4228	0.85
4 Al 5.73Mg 0.32Sc 0.3Mn	0.7749	1158.476	-2.5298	0.95
	0.8017	1578.605	-3.1510	0.95
	0.8285	2747.592	-3.7136	0.97
5 Al 3Mg 0.2 Sc	0.6141	373.3772	-2.4323	0.98
	0.6677	1013.306	-1.7464	0.99
	0.7213	1296.519	-3.3707	0.98

		0.7749	1686.164	-2.4494	0.99
		0.9035	44941.49	-41.4924	0.97
6	Al 1Mg 0.6Si	0.9250	59343.86	-50.3523	0.97
		0.9464	141708.6	-48.7770	0.98
		0.8071	31512.37	-60.0958	0.98
7	Al 6Zn 2Mg 1.4 Cu	0.8285	31926.2	-50.328	0.99
		0.8499	61055.68	-4.8128	0.97
		0.5606	41.536	-0.1155	0.98
		0.6141	285.0385	-0.4754	0.97
8	Al 5.76Mg 0.32Sc 0.3Mn	0.6677	3236.729	-21.7134	0.98
		0.7213	9509.483	-30.6182	0.99
		0.7749	27971.61	-112.4010	0.98
		0.5284	201.2234	-4.4037	0.96
		0.5606	348.8728	-2.4299	0.97
9	Al 8.9Zn 2.6Mg 0.009Sc	0.6034	2340.098	-33.5165	0.89
		0.6249	4816.361	-61.3977	0.95
		0.6463	5905.905	-35.6695	0.88
		0.8017	75.6743	-0.4645	0.98
10	Al 5Mg 0.18 Mn 0.2Sc	0.8285	93.6177	-0.4233	0.98
		0.8499	105.8661	-0.3065	0.98

Predictions in Table 7.4 are well within an order of magnitude; as required by the model, σ_0 decreases with increasing temperature and γ_0 increases with increasing temperature. From Table 7.5 it is clear that the fitting constants for Equation 7.1 obtained lead to good fits – see the values of the correlation coefficients. The detailed results are plotted in Figures 7.5-7.14.

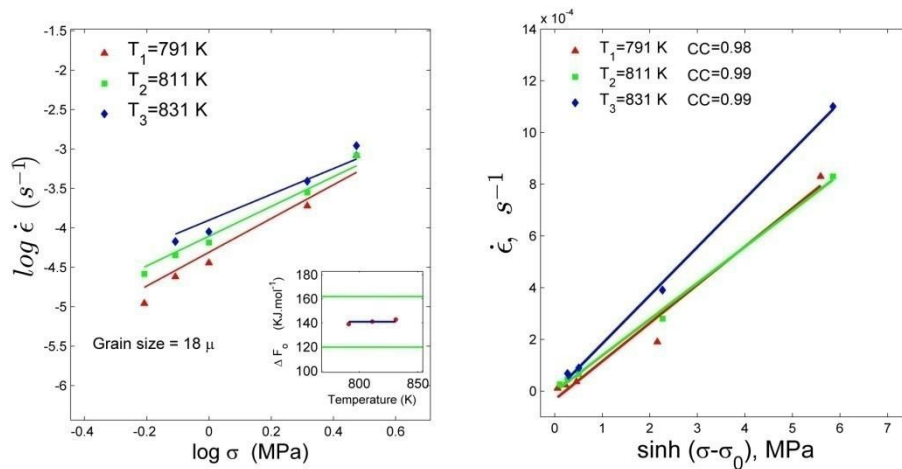


Figure 7.5: Strain rate predictions and $\dot{\epsilon}$ versus $\sinh(\sigma - \sigma_0)$ plot for system 1

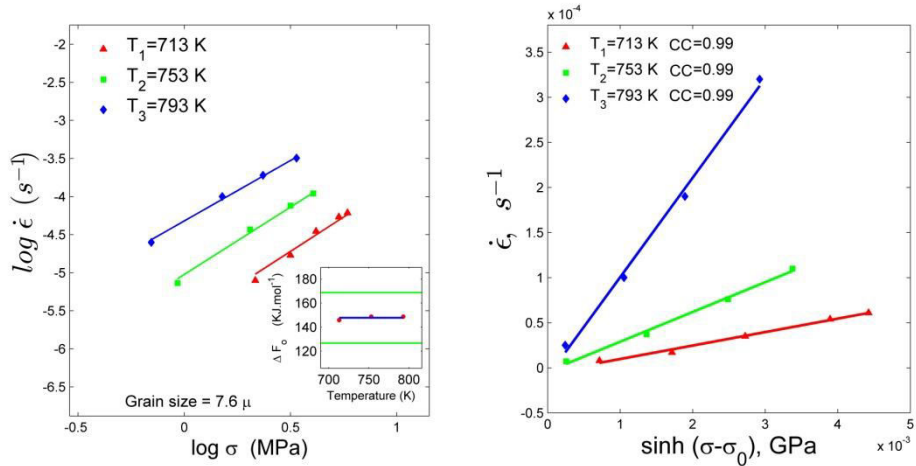


Figure 7.6: Strain rate predictions and $\dot{\epsilon}$ versus $\sinh(\sigma-\sigma_0)$ plot for system 2

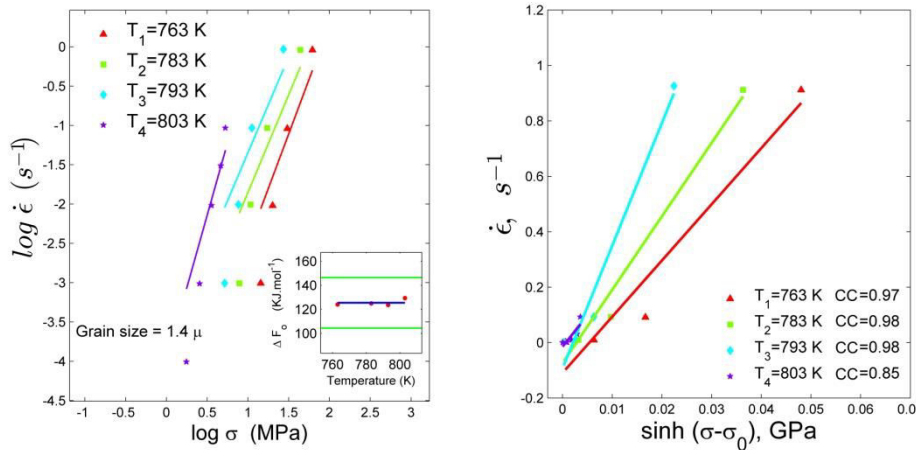


Figure 7.7: Strain rate predictions and $\dot{\epsilon}$ versus $\sinh(\sigma-\sigma_0)$ plot for system 3

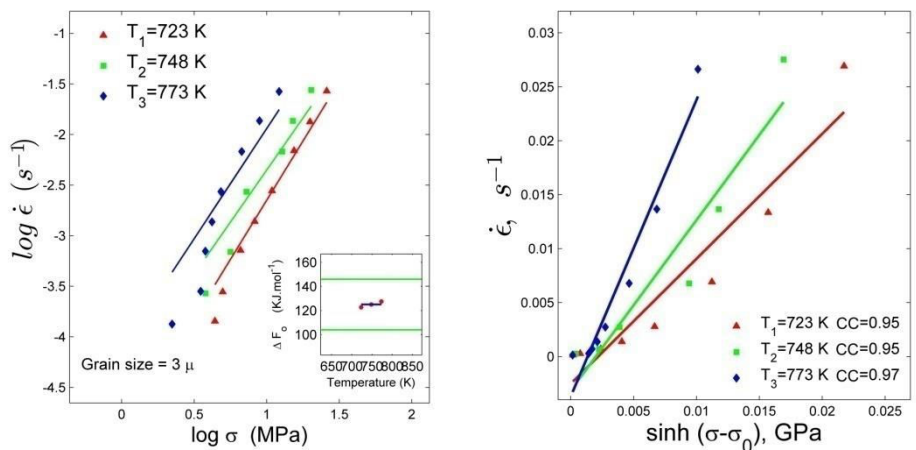


Figure 7.8: Strain rate predictions and $\dot{\epsilon}$ versus $\sinh(\sigma-\sigma_0)$ plot for system 4

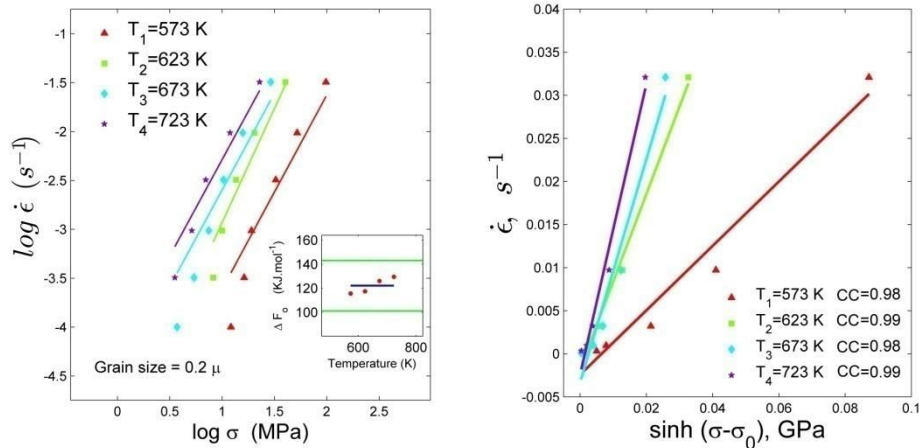


Figure 7.9: Strain rate predictions and $\dot{\epsilon}$ versus $\sinh(\sigma-\sigma_0)$ plot for system 5

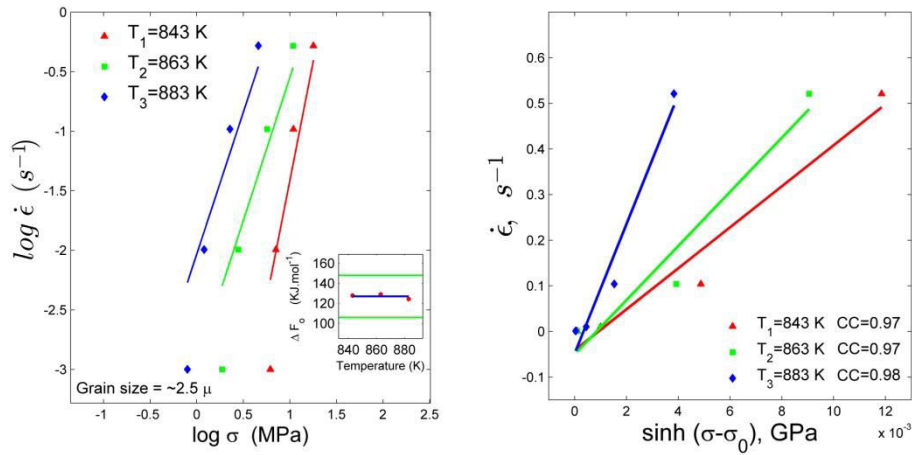


Figure 7.10: Strain rate predictions and $\dot{\epsilon}$ versus $\sinh(\sigma-\sigma_0)$ plot for system 6

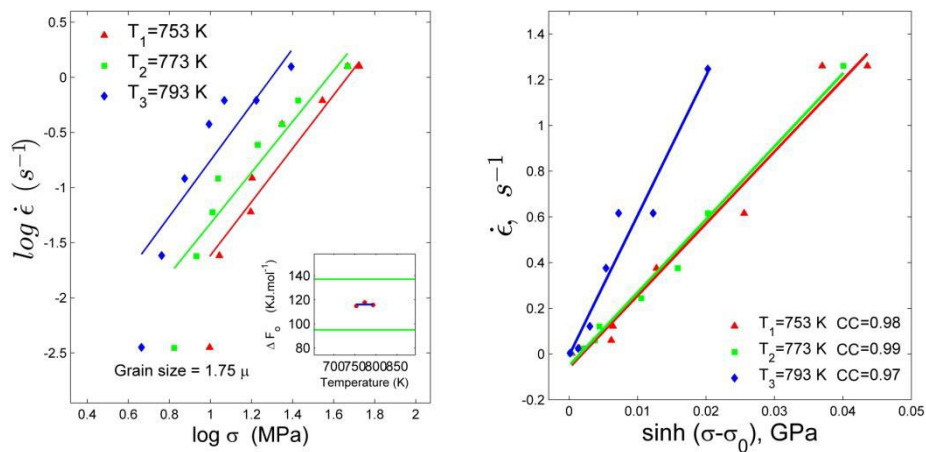


Figure 7.11: Strain rate predictions and $\dot{\epsilon}$ versus $\sinh(\sigma-\sigma_0)$ plot for system 7

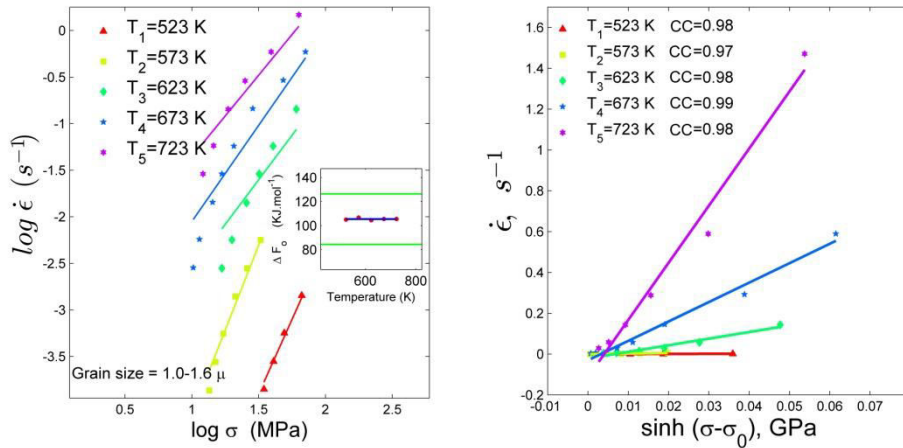


Figure 7.12: Strain rate predictions and $\dot{\epsilon}$ versus $\sinh(\sigma-\sigma_0)$ plot for system 8

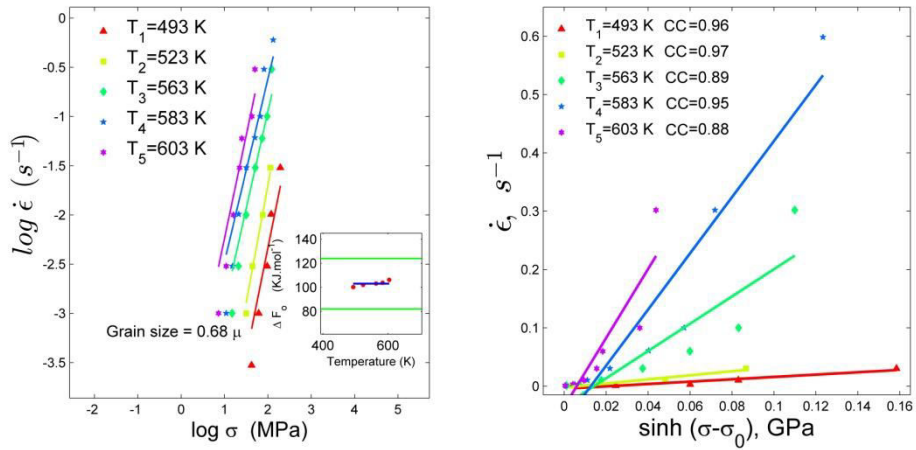


Figure 7.13: Strain rate predictions and $\dot{\epsilon}$ versus $\sinh(\sigma-\sigma_0)$ plot for system 9

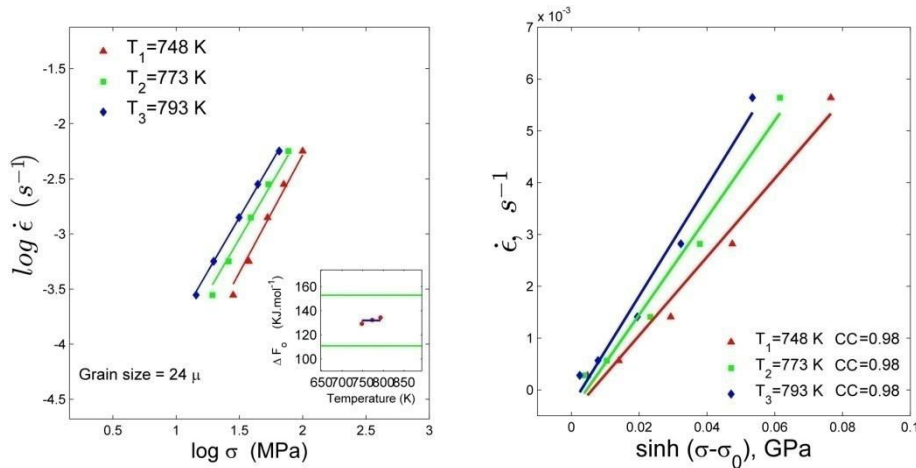


Figure 7.14: Strain rate predictions and $\dot{\epsilon}$ versus $\sinh(\sigma-\sigma_0)$ plot for system 10

7.4 Magnesium based alloys

Five magnesium-based alloys [8,37,46,57,58] were analyzed. Experiments were performed in the temperature range of 473 K to 753 K; grain sizes varied from 0.65 μm to 20 μm ; strain rate from $1.99 \times 10^{-6} \text{ s}^{-1}$ to $98.42 \times 10^{-3} \text{ s}^{-1}$; stress from 0.12 MPa to 164.62 MPa; maximum reported values of m and elongation were 0.75 and $\sim 1600\%$ respectively.

To estimate the threshold stress, σ versus $\dot{\epsilon}$ for different values of m , ranging from 0.2 to 1 was plotted in Ref. [37] and for the best fit (for $m = 0.5$), the stress was extrapolated towards zero strain rate in the σ versus $\dot{\epsilon}$ plot and the corresponding stress was reported as the threshold stress. In Equation 7.5, σ was replaced by $(\sigma - \sigma_0)$ and the activation energy was calculated based on a constitutive equation wherein $n = 2$ and $p = 3$, as the slope of $\dot{\epsilon}(T/G)(d/b)^3$ versus $1/T$ and GBS, accommodated by slip controlled grain boundary diffusion, was suggested as the RCM. Refs.[45, 57] have suggested Equation 7.7 as the most appropriate and report an activation energy, which is calculated as $Q = nR\partial(\ln\sigma)/\partial(1/T)$ at constant strain rate. Dislocation creep controlled by atom diffusion accommodated by GBS was suggested as the RCM in the regions with lower values of m or the region I of superplastic deformation and grain mantle creep accommodated by GBS was suggested in the region of higher values of m or the region II of the sigmoidal $\sigma - \dot{\epsilon}$ curve.

$$\dot{\epsilon} = A \frac{\sigma^n}{d^p} \exp\left(-\frac{Q}{RT}\right) \quad 7.7$$

Ref. [58] uses Equation 7.5 to describe the results, but with σ replaced by $(\sigma - \sigma_0)$. As the experimental data led to a strain rate sensitivity index of ~ 0.5 , σ_0 was assumed to be zero. Grain boundary diffusion accommodated by GBS is suggested to be the RCM. As in the previous cases, a macro-analysis based on Equation 7.5 or its mild variations is all that is attempted. No topological or microstructural aspects are examined. There is no attempt to develop the physical mechanisms suggested as responsible for superplastic flow in detail.

Results of the analysis: Table 7.6 presents the results for the magnesium-based systems analyzed. Table 7.7 presents the constants obtained by fitting the data using Equation 7.1.

Table 7.6: Details of the strain-rate predictions using the m-GBS model

System	T, K	ΔF_0 kJ.mol ⁻¹	γ_0	σ_0 MPa	MT	SD	AE	CC
1	473	97.3	0.0998	11.5375	3.87	0.1494	0.0668	0.9814
	498		0.1017	8.6547	3.95	0.1484	0.0664	0.9918
	523		0.1033	6.2717	5.83	0.1470	0.0658	0.9954
2	648	136.6	0.1238	0.4214	2.76	0.0155	0.0049	0.9354
	673		0.1264	0.259	2.50	0.0148	0.0047	0.9539
	698		0.1290	0.1674	2.50	0.0146	0.0046	0.9651
	723		0.1316	0.1046	2.15	0.0140	0.0044	0.9779
3	598	127.9	0.1158	7.3297	2.51	0.0577	0.0288	0.9794
	623		0.1280	3.9517	2.68	0.0572	0.0286	0.9896
	648		0.1465	2.0291	3.28	0.0590	0.0295	0.9792
	673		0.1732	1.8242	3.29	0.0552	0.0276	0.9926
4	673	123.6	0.1199	1.8093	1.23	0.0425	0.0212	0.9883
	698		0.1220	1.1424	1.44	0.0436	0.0218	0.9928
	723		0.1241	1.2133	1.46	0.0328	0.0164	0.9969
5	673	123.2	0.1000	6.7738	1.40	0.0538	0.024	0.9387
	723		0.1104	2.5488	2.02	0.0502	0.0224	0.9549
	753		0.1179	0.8912	2.18	0.0319	0.0159	0.9816

From Table 7.6 it can be seen that very good agreement between the experimental data and the predictions are obtained when the data are interpreted using the m-GBS model. Both σ_0 and γ_0 follow the expected trends in case of all the systems with varying temperatures; the values of ΔF_0 are also nearly the same at the different temperatures. Coefficient of correlation values reported in Table 7.7 demonstrate the aptness of Equation 7.1 in describing optimal superplastic flow in Mg-based alloys.

Table 7.7: Fitting constants and the correlation coefficient for Equation 7.1

System	T_{hom}	Fitting constants		CC
		$P_1 \times 10^{-3}$	$P_2 \times 10^{-3}$	
1 Mg 6Zn 0.8Zr	0.5119	647.2147	-6.0762	0.97
	0.5390	1239.21	-4.7169	0.99
	0.5660	2538.932	-3.944	0.99
2 Mg 3Zn 1.5Zr 0.5Y	0.7013	76.6857	-0.1587	0.93
	0.7284	101.8057	-0.1329	0.95
	0.7554	143.498	-0.1217	0.96
	0.7825	182.9761	-0.1023	0.97

		0.6472	124.2364	-853.822	0.97
3	Mg 4Y 0.7Zr 04Nd	0.6742	259.6659	-812.64	0.98
		0.7013	529.9517	-972.597	0.97
		0.7284	625.8909	-642.44	0.99
		0.7284	678.7522	-894.834	0.98
4	Mg 6.19Zn 1.1Y 0.46Zr	0.7554	1055.005	-897.9	0.99
		0.7825	1330.782	-451.708	0.99
		0.7284	397.1439	-1642.76	0.93
5	Mg 5.8Zn 1Y 0.48Zr	0.7825	532.4265	-1376.18	0.95
		0.8149	331.5208	-441.055	0.98

Results of this analysis are presented in Figures 7.15-7.19.

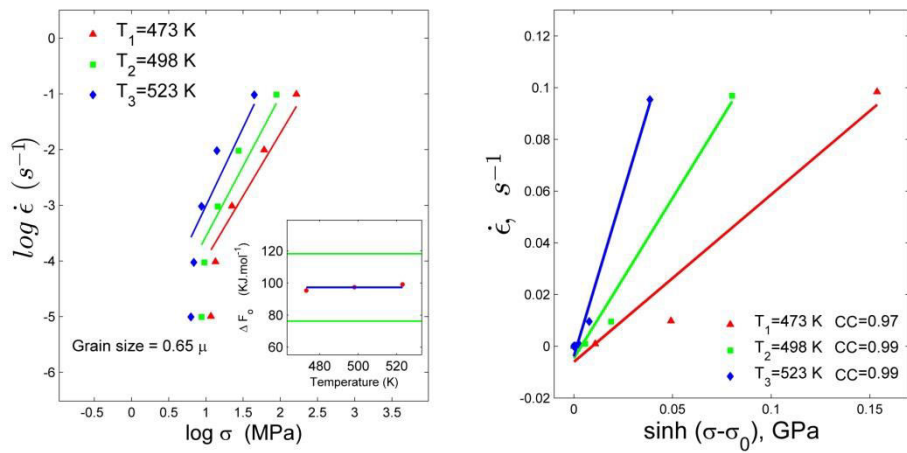


Figure 7.15: Strain rate predictions and $\dot{\epsilon}$ versus $\sinh(\sigma-\sigma_0)$ plot for system 1

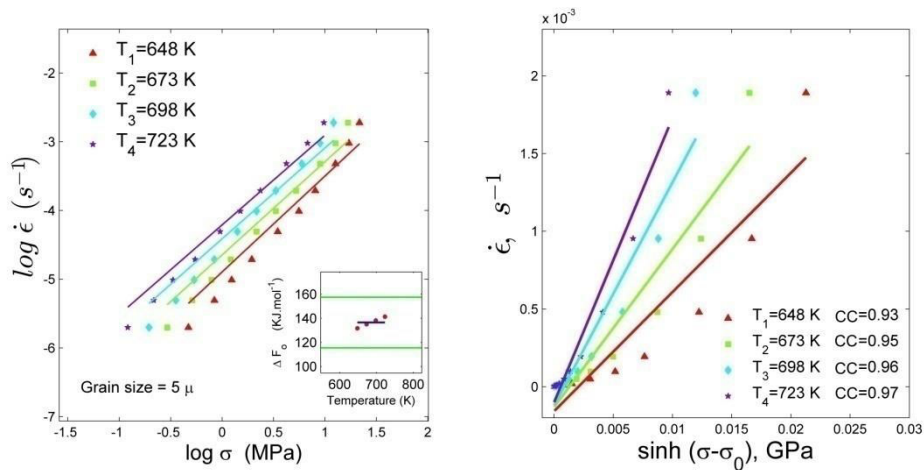


Figure 7.16: Strain rate predictions and $\dot{\epsilon}$ versus $\sinh(\sigma-\sigma_0)$ plot for system 2

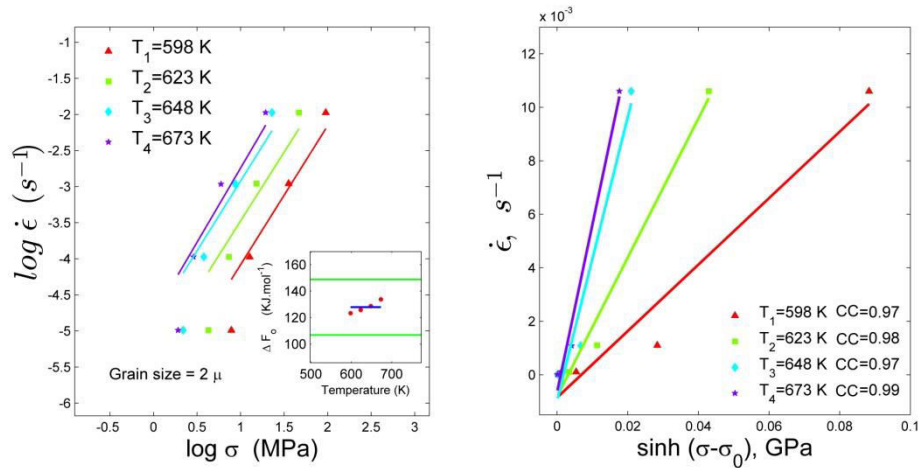


Figure 7.17: Strain rate predictions and $\dot{\epsilon}$ versus $\sinh(\sigma-\sigma_0)$ plot for system 3

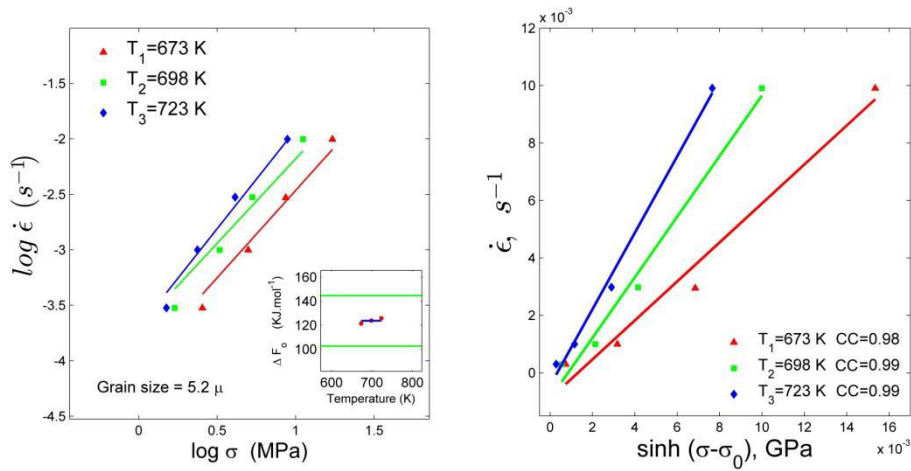


Figure 7.18: Strain rate predictions and $\dot{\epsilon}$ versus $\sinh(\sigma-\sigma_0)$ plot for system 4

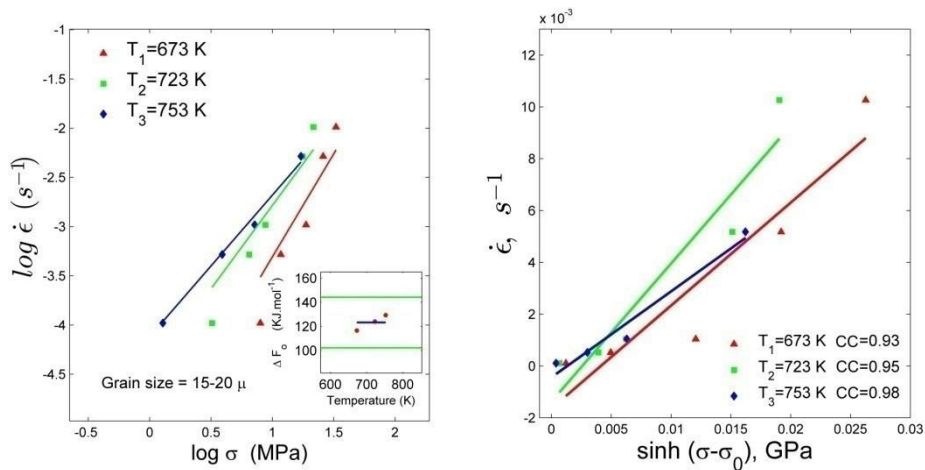


Figure 7.19: Strain rate predictions and $\dot{\epsilon}$ versus $\sinh(\sigma-\sigma_0)$ plot for system 5

7.5 Titanium-Aluminum intermetallics

Three Ti-Al intermetallics [48,59,60] were analyzed. The experimental ranges are: Temperature range: 1073 K to 1373 K; grain size range 0.9 μm to 5 μm ; reported values of activation energy, 240 $\text{kJ}\cdot\text{mol}^{-1}$ to 390 $\text{kJ}\cdot\text{mol}^{-1}$; stress was in the range of 5.98 MPa to 336.72 MPa; strain rate in the range of $9.33 \times 10^{-6} \text{ s}^{-1}$ to $5.1 \times 10^{-3} \text{ s}^{-1}$; $m \sim 0.6$; maximum reported elongation was $\sim 533\%$.

Refs. [48,59] also report an analysis based on Equation 7.5 [58, 78]. Activation energy was calculated from the slope of a plot of strain rate versus the inverse of the temperature $Q = -Rd \ln(\dot{\epsilon}) / d(1/T)$. (This would be correct in a range within which m does not vary with stress/ strain-rate.) Lattice diffusion was suggested as the RCM. Based on the values of the strain-rate sensitivity index and the activation energy, GBS was suggested as the RCM at low strain-rates and dislocation creep glide at higher strain rates. Here also the discussions are qualitative and the drawbacks pointed out with regard to the analyses for the other systems (please see above) apply in this case also.

Results of the analysis: Table 7.8 presents the results for the Ti-Al systems. Table 7.9 presents the constants for the Ti-Al systems in terms of Equation 7.1.

Table 7.8: Details of the strain-rate predictions using the m-GBS model

System	T, K	ΔF_0 $\text{kJ}\cdot\text{mol}^{-1}$	γ_0	σ_0 MPa	MT	SD	AE	CC
1	1163	285.1	0.1222	17.2108	1.03	0.0017	0.0008	0.999
	1273		0.1312	6.75030	1.13	0.0125	0.0063	0.9938
	1373		0.1409	3.72510	1.17	0.0195	0.0098	0.9969
2	1073	270.0	0.1131	39.6285	1.45	0.0109	0.0049	0.9124
	1123		0.1179	17.2646	2.03	0.0110	0.0049	0.9245
	1173		0.1222	9.49290	2.06	0.0096	0.0043	0.9605
3	1273	286.7	0.1305	20.8433	1.55	0.0092	0.0029	0.9748
	1323		0.1353	9.78730	1.63	0.0100	0.0033	0.9850
	1373		0.1413	5.29170	1.86	0.0115	0.0035	0.9797

Table 7.9: Fitting constants and the correlation coefficient for Equation 7.1

System		T_{hom}	Fitting constants		CC
			$P_1 \times 10^{-3}$	$P_2 \times 10^{-3}$	
1	Ti 48Al	0.7503	1.4726	-3.4747	0.99
		0.8213	13.596	-63.6492	0.99

		0.8858	69.2243	-147.774	0.99
		0.6923	1.7501	-88.7115	0.9
2	Ti 46.8Al 2.2Cr	0.7245	2.7759	-91.2615	0.92
		0.7568	3.8154	-49.5168	0.95
		0.8213	4.1669	-66.2571	0.97
3	Ti 43Al	0.8535	9.2534	-68.6535	0.98
		0.8858	16.486	-103.591	0.97

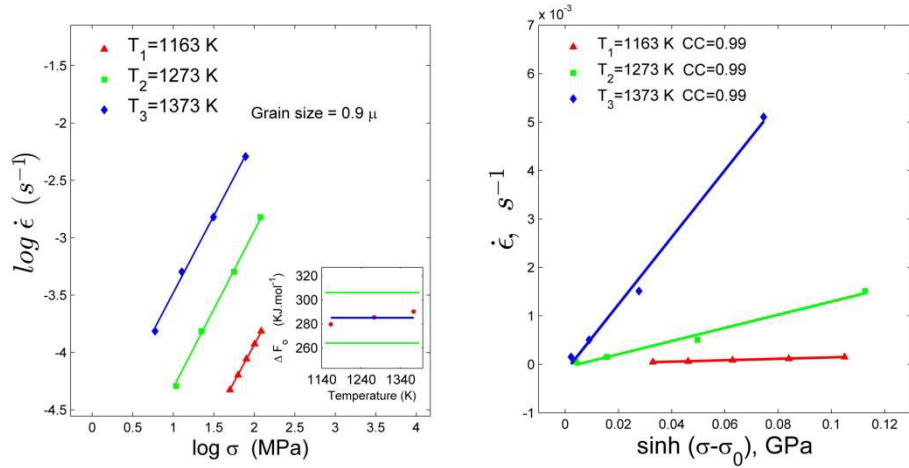


Figure 7.20: Strain rate predictions and $\dot{\epsilon}$ versus $\sinh(\sigma-\sigma_0)$ plot for system 1

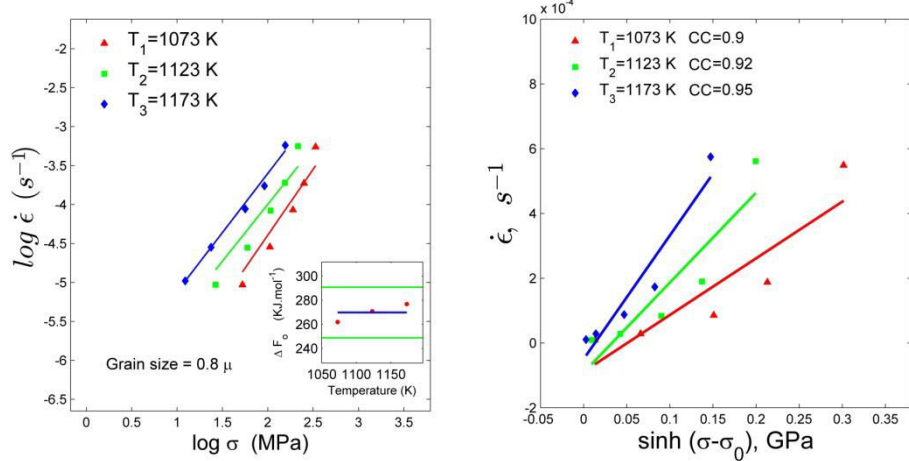


Figure 7.21: Strain rate predictions and $\dot{\epsilon}$ versus $\sinh(\sigma-\sigma_0)$ plot for system 2

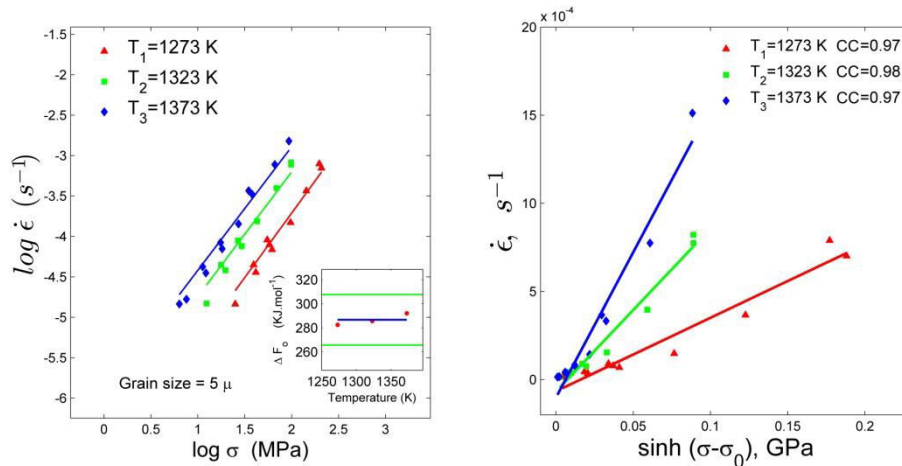


Figure 7.22: Strain rate predictions and $\dot{\epsilon}$ versus $\sinh(\sigma-\sigma_0)$ plot for system 3

From Table 7.8 it is seen that m-GBS model leads to very satisfactory predictions. Parameters like the free energy of activation, the threshold stress for the onset of mesoscopic boundary sliding, σ_0 , and the unit shear strain, γ_0 , also follow the expected trends (σ_0 decreases with increasing temperature, while γ_0 increases). Table 7.9 amply reveals the satisfactory nature of the constitutive equation, Equation 7.1. The detailed results are plotted in Figures 7.20-7.22, wherein the experimental results are compared with the predictions. Evidently the fits are good.

7.6. Titanium-based alloys

Superplastic deformation of two titanium alloys [38,61] is analyzed here. The experimental parameters were: stress 5.8 MPa to 51 MPa; strain rate $14.59 \times 10^{-6} \text{ s}^{-1}$ to $0.47 \times 10^{-3} \text{ s}^{-1}$; grain size $0.68 \text{ }\mu\text{m}$ to $2.5 \text{ }\mu\text{m}$; temperature 1033 K to 1173 K; reported values of the activation energy are $150 \text{ kJ}\cdot\text{mol}^{-1}$ to $240 \text{ kJ}\cdot\text{mol}^{-1}$.

Ref. [61] has used Equation 7.5 to describe the superplastic deformation. Dislocation motion accommodated by GBS is suggested to be the RCM.

From Table 7.10 it can be seen that good predictions could be made using the m-GBS model. Consistent with Arrhenius kinetics, the values of the free energy of activation are close, the threshold stress for the onset of mesoscopic boundary sliding and the unit shear strain follow the expected trends when the deformation temperature is changed.

Table 7.10: Details of the strain-rate predictions using the m-GBS model

System	T, K	ΔF_0 kJ.mol ⁻¹	γ_0	σ_0 MPa	MT	SD	AE	CC
1	1033	235.9	0.1369	4.2705	1.14	0.01	0.0045	0.9958
	1113		0.1454	4.264	1.29	0.0167	0.0083	0.9885
	1173		0.1524	3.9208	2.22	0.0277	0.0139	0.9681
2	1073	246.0	0.1430	8.6999	1.11	0.0082	0.0041	0.9915
	1123		0.1496	7.8124	1.23	0.0058	0.0029	0.997
	1173		0.1555	6.8838	1.31	0.0069	0.0035	0.9965

From Table 7.11, it can be seen that good fits could be obtained using the Constitutive Equation 7.1, which is the mathematical form of the m-GBS model.

Table 7.11: Fitting constants and the correlation coefficient for Equation 7.1

System	T_{hom}	Fitting constants		CC
		$P_1 \times 10^{-3}$	$P_2 \times 10^{-3}$	
Ti 6Al 4V	0.5344	23.4495	-60.7849	0.99
	0.5758	55.3287	92.017	0.98
	0.6068	156.3973	-350.068	0.96
	0.5551	11.413	-29.5702	0.99
42	0.581	15.8752	-12.4784	0.99
	0.6068	26.6418	-19.6275	0.99

The detailed results are plotted in Figures 7.23 and 7.24.

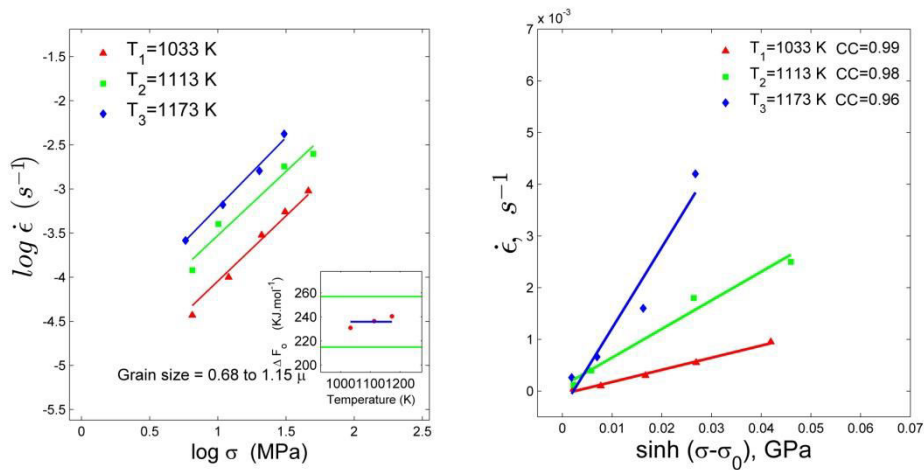


Figure 7.23: Strain rate predictions and $\dot{\epsilon}$ versus $\sinh(\sigma - \sigma_0)$ plot for system 1

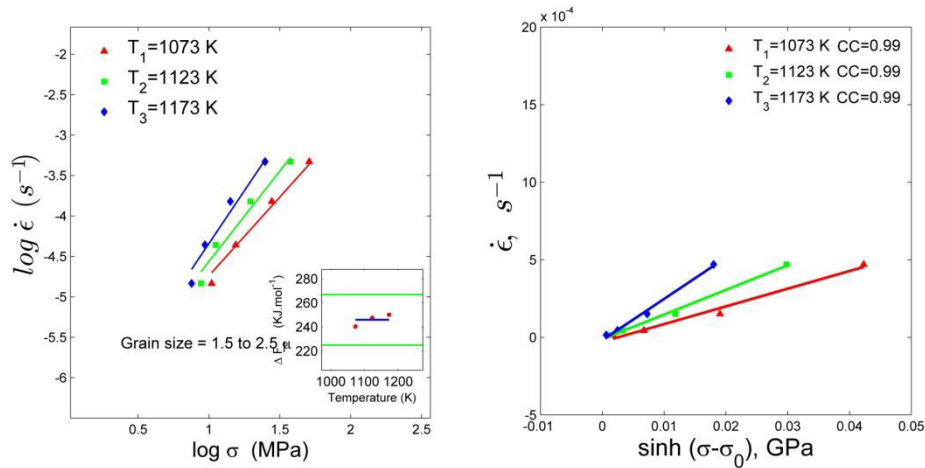


Figure 7.24: Strain rate predictions and $\dot{\epsilon}$ versus $\sinh(\sigma-\sigma_0)$ plot for system 2

7.7 Quasi-single phase copper alloy

The experimental parameters for the copper-based alloys studied in [45] are: the maximum strain rate sensitivity index was ~ 0.35 ; stress was between 8 MPa and 128 MPa; strain rate between $3.16 \times 10^{-6} \text{ s}^{-1}$ and $7.55 \times 10^{-3} \text{ s}^{-1}$; temperature range was between 673 K and 873 K; grain size between 3 μm and 7 μm . Experiments for superplastic deformation are normally performed in the tensile mode. However, Ref. [45] has superimposed for a given material data from the tensile mode on those from the double shear mode and has reported good agreement. The activation energy was calculated using Equation 7.8.

$$Q = -R \left[\frac{\delta(\ln \dot{\gamma} G^{n-1} T)}{\delta(1/T)} \right]_{d, \dot{\epsilon}} \quad 7.8$$

The value of activation energy was calculated as $\sim 120 \text{ kJ.mol}^{-1}$. Lattice self-diffusion was suggested to be the RCM. As these authors also used Equation 7.5, the same criticisms applicable to the earlier cases apply here also.

Results of the present analysis: Table 7.12 presents the results for both the quasi-single phase copper alloys analyzed.

Table 7.12: Details of the strain-rate predictions using the m-GBS model

System	T, K	ΔF_0 kJ.mol ⁻¹	γ_0	σ_0 MPa	MT	SD	AE	CC
1	723	168.3	0.0996	27.5906	1.17	0.0021	0.0011	0.9785
	773		0.1016	15.936	1.42	0.0037	0.0017	0.956
	823		0.1033	10.1771	1.54	0.0049	0.002	0.9705
	873		0.1046	7.5319	2.45	0.0114	0.004	0.9444
2	673	153.2	0.0955	26.4044	1.93	0.0072	0.0029	0.9744
	723		0.0961	17.6492	4.77	0.0212	0.0067	0.9421
	773		0.0979	13.336	6.80	0.0304	0.0092	0.9417
	823		0.1004	9.4851	8.58	0.0314	0.0095	0.9288

Table 7.13: Fitting constants and the correlation coefficient for Equation 7.1

System	T_{hom}	Fitting constants		CC
		$P_1 \times 10^{-3}$	$P_2 \times 10^{-3}$	
1	0.5332	0.7936	-2.1459	0.97
	0.5701	2.093	-8.5713	0.95
	0.6069	5.3854	-17.2568	0.97
	0.6438	19.8802	-100.093	0.94
2	0.4963	3.5944	-26.5183	0.97
	0.5332	26.0883	-335.492	0.94
	0.5701	67.1942	-720.882	0.94
	0.6069	107.2735	-875.233	0.92

Table 7.12 reveals that the m-GBS model results in good predictions. The free energy of activation, threshold stress for the onset of mesoscopic boundary sliding and the unit shear strain follow the expected trends with changes in temperature. Table 7.13 presents the constants calculated for Equation 7.1. Good correlation coefficient values have been obtained. The near-identical stress-strain rate relationship obtained in tension as well as in double shear demonstrates that superplastic flow is approximately isotropic (establishes the validity of the von Mises criterion). The results for the quasi-single phase copper alloys are plotted in detail in Figures 7.25-7.26.

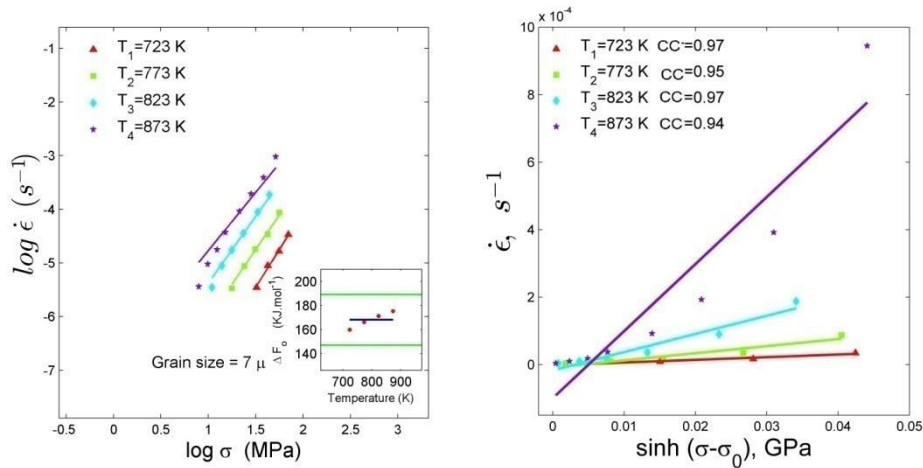


Figure 7.25: strain rate predictions and $\dot{\epsilon}$ versus $\sinh(\sigma-\sigma_0)$ plot for system 1

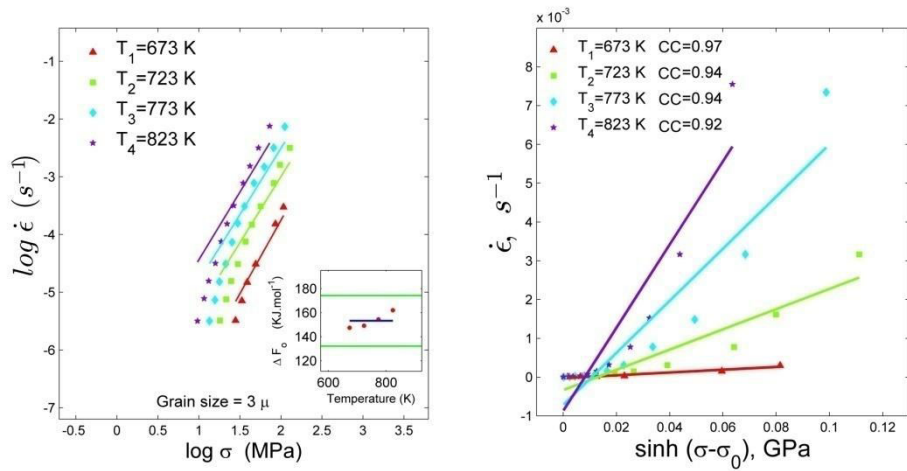


Figure 7.26: strain rate predictions and $\dot{\epsilon}$ versus $\sinh(\sigma-\sigma_0)$ plot for system 2

7.8. Nickel-based intermetallic

One Ni_3Si intermetallic system [62] was analyzed. The experimental parameters were: grain size $\sim 15 \mu\text{m}$, temperature range 1323 K to 1373 K, reported value of activation energy was $555 \text{ kJ}\cdot\text{mol}^{-1}$; strain rate varied from $36.99 \times 10^{-6} \text{ s}^{-1}$ to $1 \times 10^{-3} \text{ s}^{-1}$; stress varied from 2.07 MPa to 45.36 MPa; strain rate sensitivity ~ 0.5 ; maximum reported elongation $\sim 650\%$; the activation energy was calculated from the slope of a plot of $\log \dot{\epsilon}$ versus $1/T$. Equation 7.7 (iso-structural form of Equation 7.5) was used to describe superplastic deformation. It is suggested that the RCM at higher temperatures and lower strain rates changes from GBS to a diffusion mechanism, e.g. Coble or Nabarro-Herring creep and the change is attributed to accommodation of slip by gliding. Once again the analysis is

based on Equation 7.5/ 7.7, the discussion is qualitative and the same criticisms as in the earlier cases apply.

Results of the present analysis: Table 7.14 presents the results for the nickel-based system analyzed.

Table 7.14: Details of the strain-rate predictions using the m-GBS model

System	T, K	ΔF_0 kJ.mol ⁻¹	γ_0	σ_0 MPa	MT	SD	AE	CC
1	1323	223.8	0.1482	12.3609	1.19	0.0463	0.0267	0.9669
	1353		0.1499	7.5828	1.35	0.1192	0.0688	0.9816
	1373		0.1532	0.8330	1.42	0.0647	0.0323	0.9721

Table 7.15: Fitting constants and the correlation coefficient for Equation 7.1

System	T_{hom}	Fitting constants		CC
		$P_1 \times 10^{-3}$	$P_2 \times 10^{-3}$	
1 Ni 9Si 3.1V 2Mo	0.8818	320.8015	-577.796	0.96
	0.9018	1058.392	-4339.07	0.98
	0.9151	1025.573	-2271.22	0.97

From Table 7.14 it is seen that that good predictions are obtained using the m-GBS model. As expected, the threshold stress for the onset of mesoscopic boundary sliding decreases with increasing temperature and the unit shear strain increases with increasing temperature. Good fitting constants for Equation 7.1 have also been obtained. The results are plotted in detail in Figure 7.27.

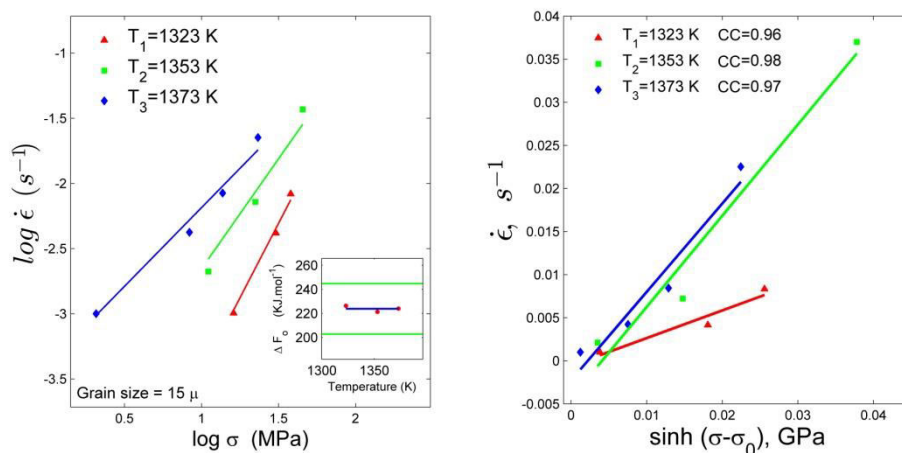


Figure 7.27: Strain rate predictions and $\dot{\epsilon}$ versus $\sinh(\sigma-\sigma_0)$ plot for system 1

7.9. Cobalt-based intermetallic

Experimental parameters for the cobalt-based intermetallic system studied here [47] were: grain size 24 μm , temperature was in the range of 1173 K to 1273 K, the activation energy in region II of superplastic deformation was estimated as 80 $\text{kJ}\cdot\text{mol}^{-1}$; maximum elongation was $\sim 350\%$. Also in the same system, but when the grain size was reduced to 10 μm , the maximum elongation increased to $\sim 550\%$; strain rate ranged from $32 \times 10^{-6} \text{ s}^{-1}$ to $1.6 \times 10^{-3} \text{ s}^{-1}$; stress ranged from 34.59 MPa to 2.93 MPa; the strain rate sensitivity was ~ 0.6 ; the constitutive equation suggested to describe the flow was similar to Equation 7.7/7.5. In region II, relevant to the current study, n was calculated to be 1.7. The reported activation energy was calculated using an Arrhenius plot; dynamic recrystallization and GBS are suggested to be responsible for deformation in higher and lower strain rate regions respectively. Again, the discussions are qualitative.

Results of the present analysis: Table 7.16 presents the results for superplastic deformation in the cobalt-based intermetallic in terms of the m-GBS model.

Table 7.16: Details of the strain-rate predictions using the m-GBS model

System	T, K	ΔF_0 $\text{kJ}\cdot\text{mol}^{-1}$	γ_0	σ_0 MPa	MT	SD	AE	CC
1	1173	224.8	0.1288	5.7373	1.76	0.014	0.0063	0.9507
	1223		0.134	2.6424	1.83	0.0161	0.0066	0.9486
	1273		0.1397	2.0119	1.89	0.018	0.0081	0.9484

Table 7.17: Fitting constants and the correlation coefficient for Equation 7.1

System	T_{hom}	Fitting constants		CC
		$P_1 \times 10^{-3}$	$P_2 \times 10^{-3}$	
1 Co 22Ti	0.8925	28.6802	-147.522	0.95
	0.9305	53.1694	-210.838	0.94
	0.9686	96.1300	-257.923	0.94

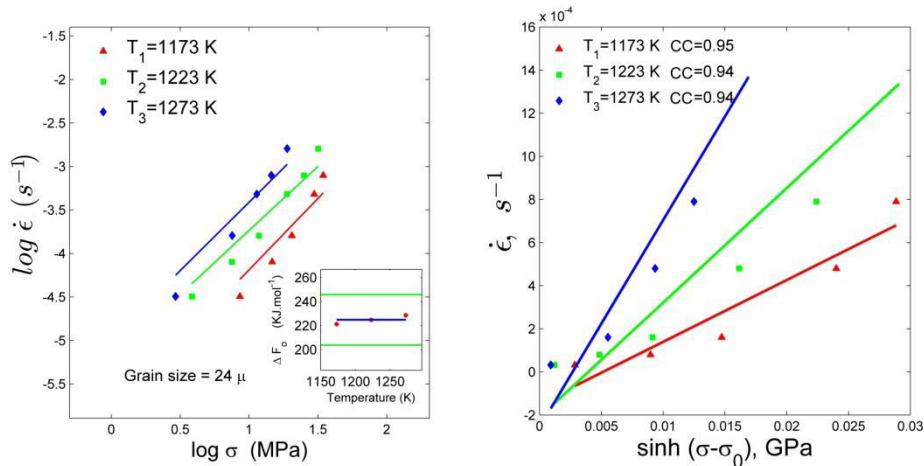


Figure 7.28: Strain rate predictions and $\dot{\epsilon}$ versus $\sinh(\sigma-\sigma_0)$ plot for system 1

From Tables 7.16- 7.17 it can be seen that that good predictions have been obtained using the m-GBS model. The threshold stress for the onset of mesoscopic boundary sliding decreases with increasing temperature and the unit shear strain increases with increasing temperature. Good fitting constants for Equation 7.1 have also been obtained. The results are plotted in detail in Figure 7.28.

7.10 Zirconia-based ceramics

Seven Zirconia-based systems [63–67] were analyzed. Deformation data for a constant temperature, but varying grain size are also available. Reported values of strain rate sensitivity index is ~ 0.5 ; activation energy values reported ranged from $343 \text{ kJ}\cdot\text{mol}^{-1}$ to $\sim 683 \text{ kJ}\cdot\text{mol}^{-1}$; strain rates ranged between $1.9 \times 10^{-6} \text{ s}^{-1}$ and $1.1 \times 10^{-3} \text{ s}^{-1}$; stress ranged between 2.62 MPa and 757.64 MPa; experiments were performed in a temperature range of 1323 K to 1723 K; grain size ranged between 65 nm and $1.10 \mu\text{m}$.

Ref. [63] has proposed a model in which both diffusion and interface reaction act sequentially. GBS is suggested to be the accommodating mechanism and at lower grain sizes, where superplasticity is observed, interface reaction is considered to be the RCM. Further, the investigators have proposed Equation 7.9 and suggest that it fits the experimental results fairly well.

$$\frac{1}{\dot{\epsilon}} = \frac{1}{\dot{\epsilon}_D} + \frac{1}{\dot{\epsilon}_i} ; \text{ where } \frac{1}{\dot{\epsilon}_D} = \frac{A\sigma}{d^2} \text{ and } \frac{1}{\dot{\epsilon}_i} = \frac{B\sigma^2}{d} \quad 7.9$$

Equation 7.9 is typical of summation of parallel processes. But, the model [63] assumes sequential operation. A contradiction is present here. Ref. [64] conjectures the formation of amorphous phases at triple points to release the stress concentration caused by GBS and facilitate superplastic deformation. The paper contains the results for the deformation of pure zirconia and zirconia in which impurities are present. A higher strain- rate sensitivity index results when impurities are present. When the weight percentage of alumina drops from 0.065% to 0.005%, m drops from 0.5 to 0.3. Higher percentage of alumina is said to lead to the presence of an amorphous phase at grain boundaries. Hence, increased impurities facilitate superplastic deformation (possibly by lowering the melting point of the material). Diffusion is suggested to be the RCM by both Refs. [64,65] and Equation 7.7 is chosen to explain the deformation behavior. Ref. [66] uses Equation 7.5 instead. (As already pointed out, both are similar equations.) The investigators report a behavior similar to that of the Zn-22Al alloy. Grain boundary diffusion is suggested as the rate-limiting mechanism. Both the values of n and p in Equation 7.5 are taken as 2.5. Ref. [67] also assumes the dependence of strain rate as shown in Equation 7.7. The value for p , calculated as the slope of the line obtained by plotting $\log \dot{\epsilon}$ versus $\log d$, is reported as 2.2. The stress exponent, n , calculated as the slope of the line obtained by plotting $\log \dot{\epsilon}$ versus $\log \sigma$, is deduced as ~ 0.5 . Arrhenius plot of $\log \dot{\epsilon}$ versus $1/T$ was used to calculate the activation energy. Finally, Ref. [67] concludes that at both low and high stresses diffusion accommodates flow. At low stresses, it is said to accommodate interfacial reaction and at high stresses, GBS.

Results of the present analysis: Table 7.18 presents the results for the zirconia-based ceramics analyzed in this study. Apart from system 2, where the threshold stress does not follow the expected trend at one temperature, for the remaining systems, the threshold stress for the onset of mesoscopic boundary sliding and the unit shear strain follow the expected trends when there is a temperature change. Likewise, consistent with the theoretical requirement, σ_0 increases with decreasing grain size. The values of the free

energy of activation are very close to each other in all the cases, which is good evidence for the robustness of the analysis.

Table 7.19 presents constants of superplastic flow, as described by the constitutive equation, Equation 7. 1. Good correlation coefficient is observed in all cases.

Table 7.18: Details of the strain-rate predictions using the m-GBS model

System	T, K	ΔF_0 kJ.mol ⁻¹	γ_0	σ_0 MPa	MT	SD	AE	CC
1	1523	379.4	0.0959	12.9094	1.30	0.0022	0.0008	0.9859
	1573		0.0964	12.9027	1.32	0.0044	0.0017	0.9871
	1623		0.0981	8.2414	1.33	0.0065	0.0027	0.9908
	1673		0.0991	7.9680	1.39	0.0098	0.0040	0.9914
	1723		0.1023	2.4011	2.09	0.0106	0.0035	0.9675
2	1523	385.4	0.0967	3.4499	1.85	0.0022	0.0007	0.9857
	1573		0.0976	3.4480	2.13	0.0045	0.0013	0.9863
	1623		0.0990	2.1949	2.20	0.0060	0.0018	0.9861
	1673		0.1002	2.1938	2.36	0.0109	0.0033	0.9586
	1723		0.1021	2.2541	2.44	0.0094	0.0031	0.9752
3	1723	373.1	0.0992	6.8651	1.45	0.0357	0.0126	0.9617
	1723		0.0995	6.8638	2.25	0.0339	0.0169	0.9994
	1723		0.1013	6.8611	2.38	0.0113	0.0051	0.9828
4	1573	372.8	0.0963	6.4000	1.21	0.0029	0.0010	0.9986
	1623		0.0973	6.2600	1.46	0.0042	0.0015	0.9921
	1673		0.0987	6.2500	1.47	0.0059	0.0021	0.995
	1723		0.1000	6.2400	1.48	0.0098	0.0035	0.9942
	1773		0.1013	3.1600	1.65	0.0257	0.0091	0.9863
5	1273	342.9	0.0795	103.1361	1.78	0.0135	0.0060	0.9814
	1323		0.0814	59.9498	1.90	0.0144	0.0065	0.9744
	1373		0.0830	46.1385	2.18	0.0132	0.0059	0.9765
6	1323	344.7	0.0802	71.4000	1.64	0.0162	0.0072	0.9755
	1323		0.0820	71.3789	2.01	0.0087	0.0043	0.9882
	1323		0.0823	71.3743	4.13	0.0090	0.0045	0.9745
7	1573	364.0	0.0961	7.1985	1.38	0.0034	0.0014	0.9258
	1623		0.0968	5.2334	1.45	0.0058	0.0024	0.964
	1673		0.0971	3.3787	1.48	0.0105	0.0043	0.9678
	1723		0.0976	3.0077	1.50	0.0266	0.0109	0.9231

Table 7.19: Fitting constants and the correlation coefficient for Equation 7.1

System	T_{hom}	Fitting constants		CC
		$P_1 \times 10^{-3}$	$P_2 \times 10^{-3}$	
1 ZrO ₂ 3Y ₂ O ₃	0.5097	0.9594	-0.0039	0.98
	0.5264	3.8492	-0.0165	0.98

		0.5432	8.0142	-0.0285	0.99
		0.5599	21.0356	-0.0684	0.99
		0.5766	24.3316	-0.0884	0.96
		0.5097	0.5229	-0.0028	0.98
		0.5264	1.7767	-0.0135	0.98
2	ZrO ₂ 4Y ₂ O ₃	0.5432	4.4666	-0.0216	0.98
		0.5599	12.5954	-0.0839	0.95
		0.5766	17.4807	-0.0661	0.97
		0.5766	129.2258	-0.847	0.96
3	ZrO ₂ 3Y ₂ O ₃	0.5766	50.9903	-0.143	0.99
		0.5766	15.4222	-0.098	0.98
		0.5264	2.8212	4.5305	0.99
		0.5432	8.9724	-4.3583	0.99
4	ZrO ₂ 8Y ₂ O ₃	0.5599	18.8543	-1.4103	0.99
		0.5766	48.5755	-87.4941	0.99
		0.5934	142.4123	-926.354	0.98
		0.4260	1.4703	-0.1037	0.97
5	ZrO ₂	0.4428	2.6235	-0.1249	0.97
		0.4595	3.8369	-0.0981	0.97
		0.4428	2.6103	-0.0940	0.97
6		0.4428	0.8178	-0.0427	0.98
		0.4428	0.5966	-0.0578	0.97
		0.5264	2.3864	-9.4079	0.92
7	ZrO ₂ 8Y ₂ O ₃	0.5432	7.8049	-33.8547	0.96
		0.5599	24.2874	-139.869	0.96
		0.5766	128.5281	-751.202	0.92

The obtained results are plotted in Figures 7.29 to 7.35.

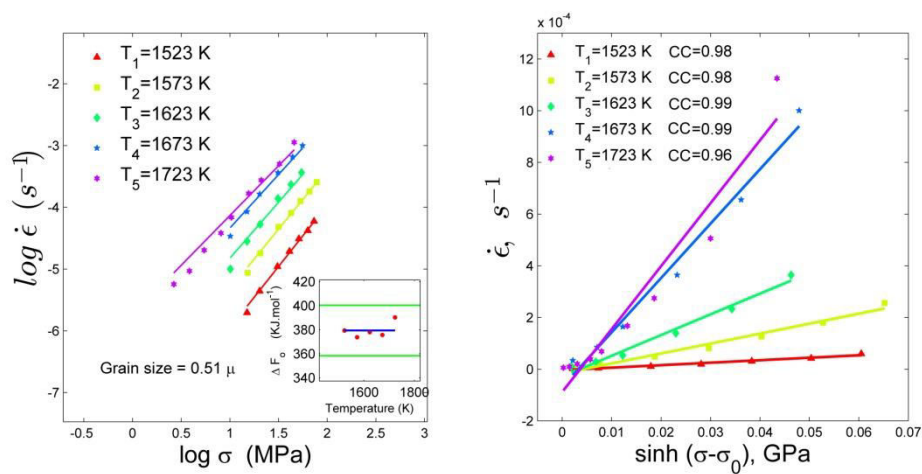


Figure 7.29: Strain rate predictions and $\dot{\epsilon}$ versus $\sinh(\sigma-\sigma_0)$ plot for system 1

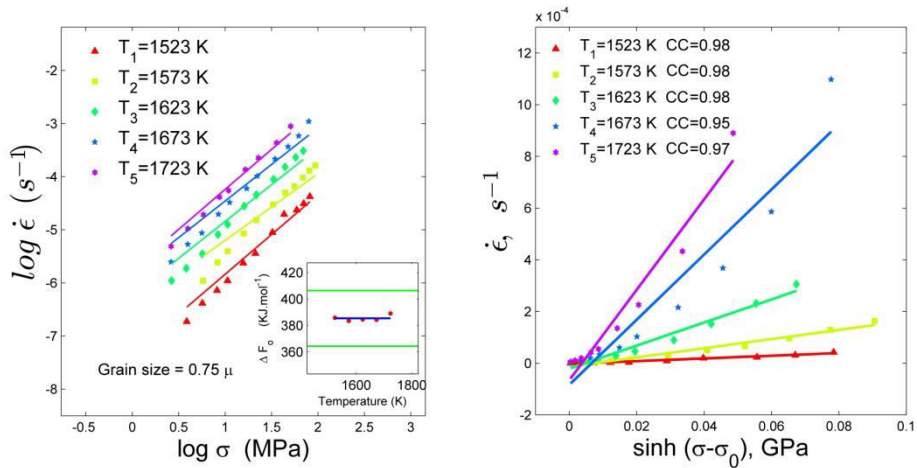


Figure 7.30: Strain rate predictions and $\dot{\epsilon}$ versus $\sinh(\sigma-\sigma_0)$ plot for system 2

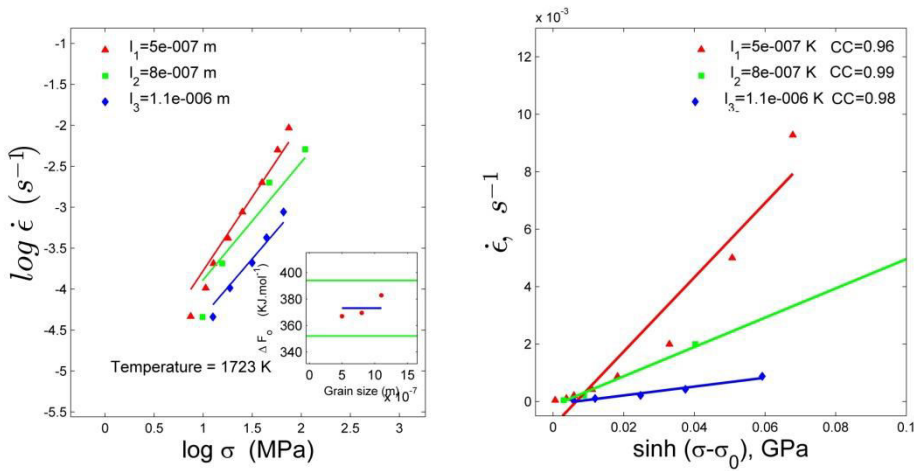


Figure 7.31: Strain rate predictions and $\dot{\epsilon}$ versus $\sinh(\sigma-\sigma_0)$ plot for system 3

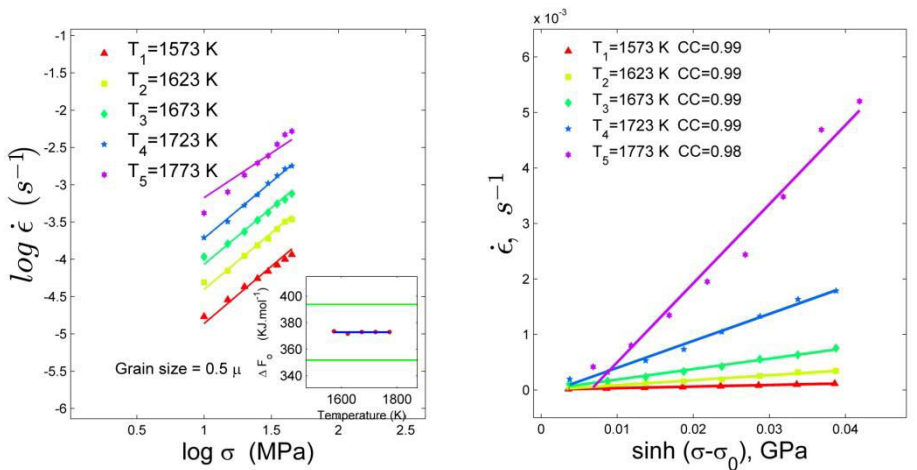


Figure 7.32: Strain rate predictions and $\dot{\epsilon}$ versus $\sinh(\sigma-\sigma_0)$ plot for system 4

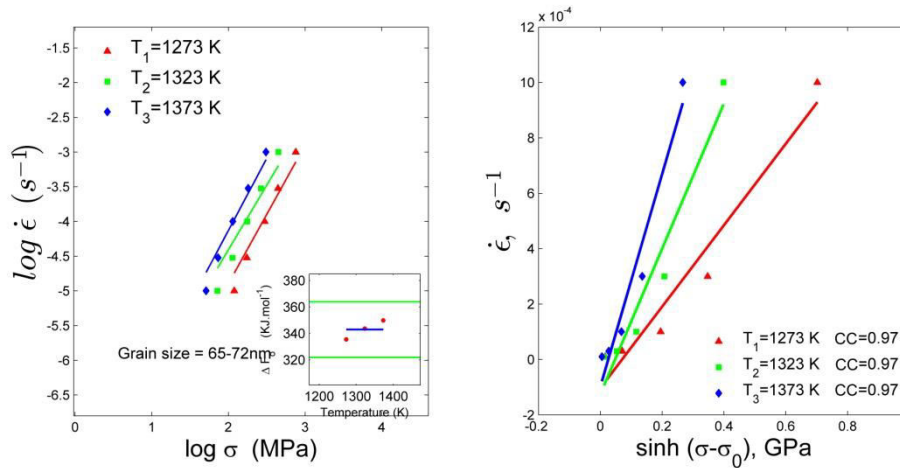


Figure 7.33: Strain rate predictions and $\dot{\epsilon}$ versus $\sinh(\sigma-\sigma_0)$ plot for system 5

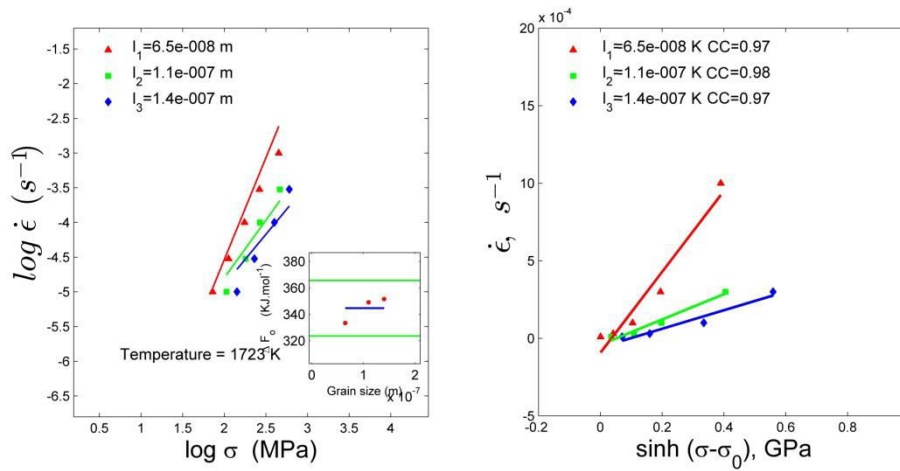


Figure 7.34: Strain rate predictions and $\dot{\epsilon}$ versus $\sinh(\sigma-\sigma_0)$ plot for system 6

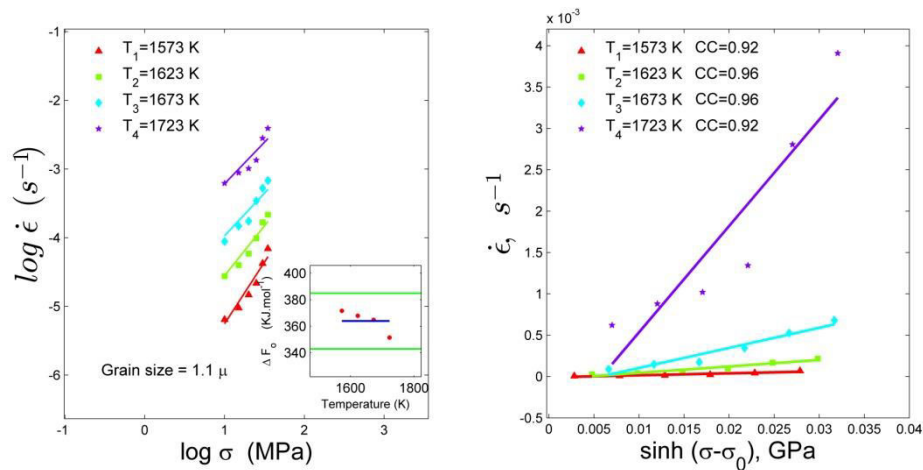


Figure 7.35: Strain rate predictions and $\dot{\epsilon}$ versus $\sinh(\sigma-\sigma_0)$ plot for system 7

7.11 Alumina-based ceramics

Three Alumina-based ceramics [68–70] were analyzed. Experimental parameters were: grain size varied from 0.39 μm to 1.30 μm ; temperature from 1623 K to 1773 K; strain rate from $3.63 \times 10^{-6} \text{ s}^{-1}$ to $9.27 \times 10^{-3} \text{ s}^{-1}$; stress from 5.00 MPa to 50.00 MPa; maximum m was ~ 0.7 .

Refs. [65, 66] suggests a model for superplastic flow which gives rise to an equation similar to Equation 7.7. However in Ref. [69] a threshold stress is introduced and the stress term in Equation 7.7 becomes $(\sigma - \sigma_0)$. Dislocation motion accommodated by GBS is suggested to be the RCM. Also, the reported activation energy is calculated as the slope of a plot of $\log(\sigma/G)$ versus $1/T$ (not in line with conventional Arrhenius kinetics where $\log \dot{\epsilon}$ is plotted against $(1/T)$; also, the temperature dependences of σ and G are not identical and so both x and y axes will be functions of T , which makes the plot devoid of physical significance). The deformation behavior is suggested to be similar to that of Zn-22%Al alloys. Ref. [70] proposes interface reaction controlled, diffusion accommodated GBS as the dominant deformation mechanism. In these cases also, Equation 7.5 is used to describe the deformation with the value of p as between 1 and 3; $n \sim 1.7$. As the basis of the analysis in these cases also is Equation 7.5, the same problems listed in the earlier cases would be applicable here as well.

Results of the present analysis: Table 7.20 presents the detailed results for the three alumina-based systems analyzed using the m-GBS model. It can be seen that the threshold stress for the onset of mesoscopic boundary sliding and the unit shear strain follow the expected trends with temperature variations and the values of the free energy of activation for the three alumina-based systems are fairly close, which is evidence for the robustness of the analysis.

Table 7.20: Details of the strain-rate predictions using the m-GBS model

System	T, K	ΔF_0 kJ.mol ⁻¹	γ_0	σ_0 MPa	MT	SD	AE	CC
1	1673	358.7	0.0881	19.5800	1.44	0.028	0.014	0.9972
	1723		0.0886	17.4200	1.59	0.0229	0.0114	0.9945
	1773		0.0894	3.3600	4.11	0.0442	0.0221	0.9960

2	1673	374.6	0.0898	7.4385	1.56	0.0047	0.0014	0.9882
	1723		0.0904	5.7491	1.82	0.0152	0.0046	0.9749
	1773		0.0917	4.6019	1.89	0.0298	0.0099	0.9665
3	1623	375.2	0.0796	9.4542	1.04	0.0008	0.0003	0.9998
	1648		0.0797	9.2143	1.08	0.0012	0.0005	0.9996
	1673		0.0798	8.8145	1.08	0.0016	0.0006	0.9996
	1698		0.0800	8.6147	1.02	0.0013	0.0005	0.9997
	1723		0.0801	4.0975	1.05	0.0028	0.0011	0.9949

Table 7.21: Fitting constants and the correlation coefficient for Equation 7.1

	System	T_{hom}	Fitting constants		CC
			$P_1 \times 10^{-3}$	$P_2 \times 10^{-3}$	
1	Al ₂ O ₃ 30ZrO ₂ 30Al ₁₆ Si ₂ O ₁₃	0.7233	7.2865	35.958	0.99
		0.7449	57.4951	91.9791	0.99
		0.7665	250.3922	-2642.29	0.99
2	Al ₂ O ₃ 30ZrO ₂ 30Al ₁₆ Si ₂ O ₁₃	0.7233	6.6130	-23.2809	0.98
		0.7449	48.6727	-217.045	0.97
		0.7665	216.8111	-860.89	0.96
3	Al ₂ O ₃ 25NiAl ₂ O ₄ 25ZrO ₂	0.7017	0.6864	0.9524	0.99
		0.7125	1.2391	2.2615	0.99
		0.7233	2.9425	4.0455	0.99
		0.7341	4.7465	-1.52	0.99
		0.7449	7.7078	-7.045	0.99

Table 7.21 presents the results for the systems analyzed as per Equation 7.1, which is the mathematical form of the m-GBS model. Good correlation coefficients have been obtained. The results are plotted in detail in Figures 7.36-7.38.

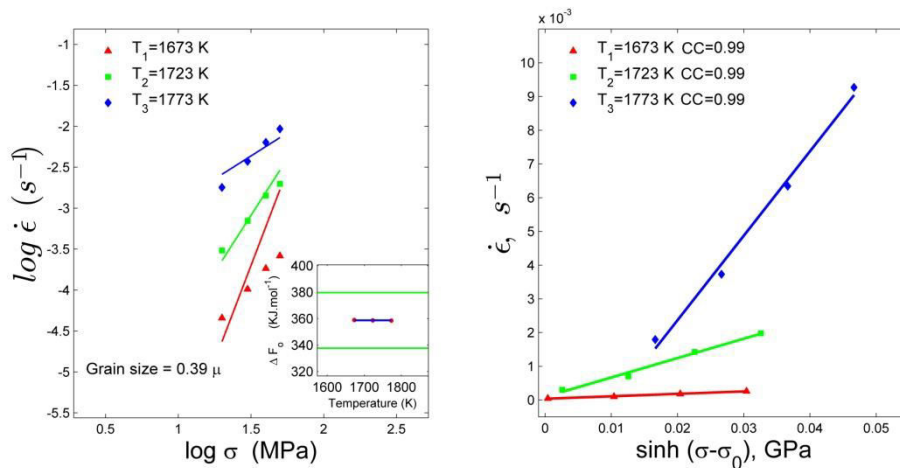


Figure 7.36: Strain rate predictions and $\dot{\epsilon}$ versus $\sinh(\sigma-\sigma_0)$ plot for system 1

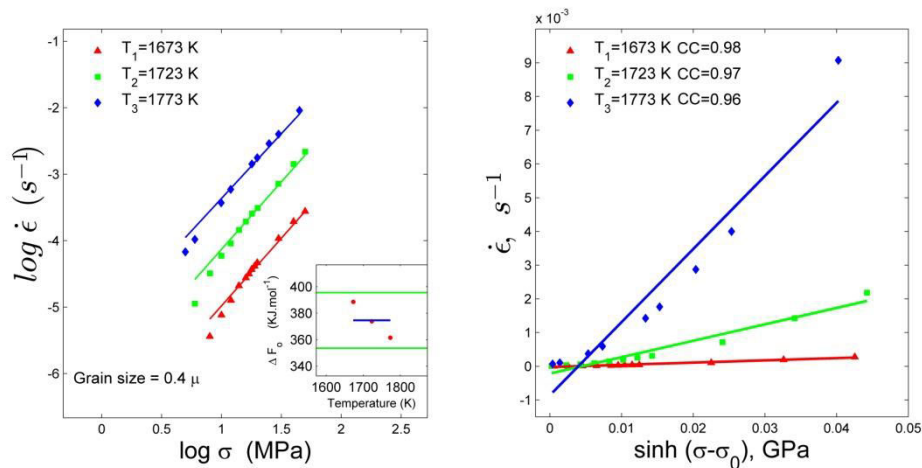


Figure 7.37: Strain rate predictions and $\dot{\epsilon}$ versus $\sinh(\sigma-\sigma_0)$ plot for system 2

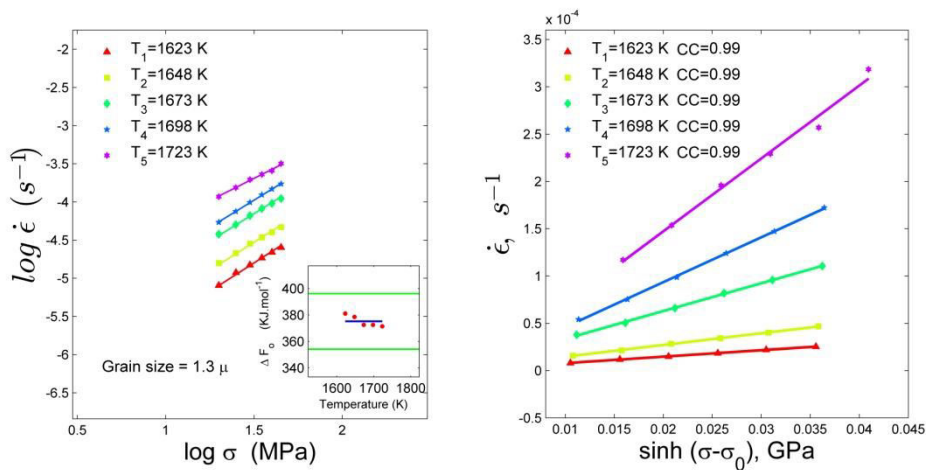


Figure 7.38: Strain rate predictions and $\dot{\epsilon}$ versus $\sinh(\sigma-\sigma_0)$ plot for system 3

7.12 Silicon-based ceramics

A silicon nitride ceramic [71] was analyzed here. Experimental parameters were: stress 10.07 MPa to 223.27 MPa; strain rate $6.03 \times 10^{-6} \text{ s}^{-1}$ to $0.89 \times 10^{-3} \text{ s}^{-1}$; temperature: 1723 K-1873 K; grain size 68 nm; maximum $m \sim 0.5$. Equation 7.7 was used by the investigators to interpret the results. Interface-controlled solution-precipitation with two dimensional nucleation was suggested to be the RCM at low stresses and GBS accommodated by diffusion-controlled solution-precipitation at higher stresses. Arrhenius plot of $\log \dot{\epsilon}$ versus $(1/T)$ was used to compute the activation energy. This analysis also is phenomenological, lacks in topological and microstructural evidence and suffers from the same limitations as the other analyses based on Equations 7.5/ 7.7.

Results of the analysis using the m-GBS model: Table 7.22 presents the results for the analysis based on the m-GBS model. Good tolerance values were obtained. The threshold stress for the onset of mesoscopic boundary sliding and the unit shear strain followed the expected trends with a change in the test temperature. All the values of the free energy of activation were fairly close to each other making the findings consistent with Arrhenius kinetics.

Table 7.22: Details of the strain-rate predictions using the m-GBS model

System	T, K	ΔF_0 kJ.mol ⁻¹	γ_0	σ_0 MPa	MT	SD	AE	CC
1	1723	444.8	0.1285	12.4299	1.19	0.0027	0.0010	0.9936
	1773		0.1287	8.3220	1.26	0.0065	0.0026	0.9981
	1823		0.1287	3.7248	1.26	0.0059	0.0024	0.9967
	1873		0.1289	3.2416	1.14	0.0058	0.0026	0.9984

From the Table 7.23 it can be concluded that Equation 7.1 satisfactorily describes optimal superplastic flow. Excellent values for the correlation coefficient were obtained.

Table 7.23: Fitting constants and the correlation coefficient for Equation 7.1

System	T_{hom}	Fitting constants		CC
		P_1	$P_2 \times 10^{-3}$	
1 Si_3N_4 $5Y_2O_3$ $2Al_2O_3$	0.7929	0.5939	4.1133	0.99
	0.8159	1.7834	13.0443	0.99
	0.8389	4.8779	18.2629	0.99
	0.8619	15.3412	21.3169	0.99

The obtained results are plotted in detail in Figure 7.39.

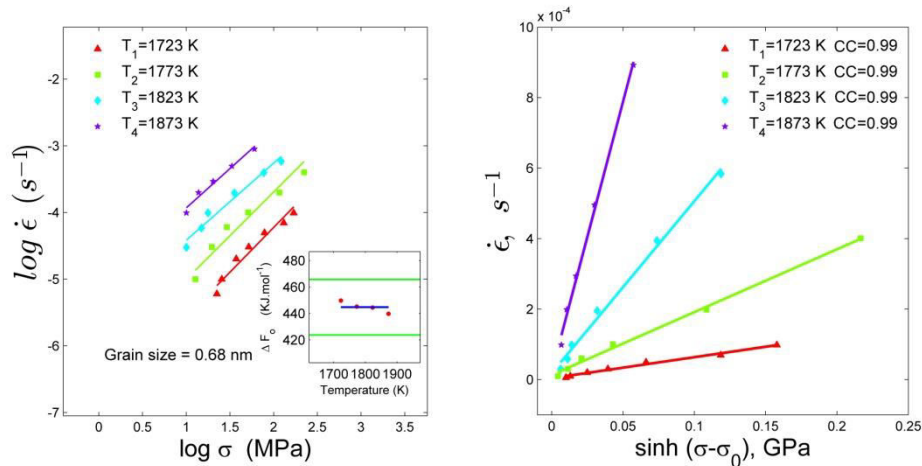


Figure 7.39: Strain rate predictions and $\dot{\epsilon}$ versus $\sinh(\sigma-\sigma_0)$ plot for system 1

7.13 Olivine

Results for the superplastic deformation of Olivine reported in Ref. [76] were considered for the present analysis. The experimental parameters were: strain rate $1.22 \times 10^{-6} \text{ s}^{-1}$ to $97.76 \times 10^{-6} \text{ s}^{-1}$; stress 161 MPa to 420 MPa; grain size $5.4 \mu\text{m}$; temperature range 1423 K-1523 K; reported value of activation energy 445 kJ.mol^{-1} . Equation 7.7 was used to describe the flow. However, to scale to the mantle conditions, a pressure term was introduced by replacing Q by $E+PV$ in Equation 7.7. The values of n and p are suggested as 2.9 and 0.7; GBS is suggested to be the dominant deformation mechanism. The basis of the analysis, viz. Equation 7.7, makes it susceptible to the same criticisms as the analyses discussed above.

Results of the present analysis: Table 7.24 presents the results obtained using the m-GBS model. It can be seen that consistent with Arrhenius kinetics, almost identical values for the free energy of activation have been predicted, the unit shear strain and the threshold stress for the onset of mesoscopic boundary sliding follow the expected trends with a change in the temperature of deformation. Good tolerance values were also obtained. However, compared with the values pertaining to metallic materials and ceramics, the predicted values of the unit shear strain were substantially higher than the value of ~ 0.1 , assumed based on bubble raft experiments. The complex structure and composition of Olivine – a mineral - could be the reason. But, this is yet to be proved.

Table 7.24: Details of the strain-rate predictions using the m-GBS model

System	T, K	ΔF_0 kJ.mol ⁻¹	γ_0	σ_0 MPa	MT	SD	AE	CC
1	1423	344.8	0.3991	143.8200	1.24	0.0015	0.0008	0.9599
	1473		0.4000	107.9910	1.51	0.0049	0.0022	0.9600
	1523		0.4011	82.9150	1.85	0.0047	0.0027	0.9825

Table 7.25 presents the values of the constants in the constitutive equation, Equation 7.1. It can be seen that very good values for the correlation coefficient are obtained and the equation represents optimal superplastic flow accurately.

Table 7.25: Fitting constants and the correlation coefficient for Equation 7.1

System	T_{hom}	Fitting constants		CC
		$P_1 \times 10^{-3}$	$P_2 \times 10^{-3}$	
1 San Carlos Olivine	0.6549	0.0587	-1.4519	0.96
	0.6779	0.3591	-26.4098	0.96
	0.7009	0.6124	-20.8976	0.98

The detailed results are presented in Figure 7.40.

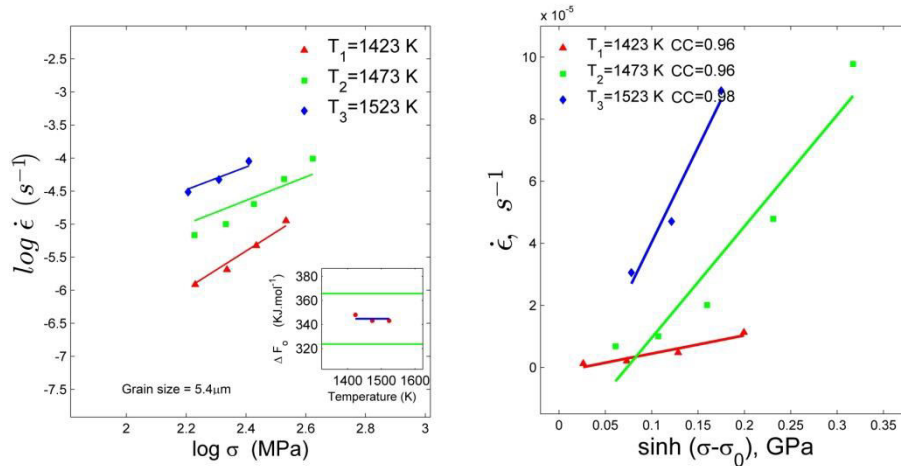


Figure 7.40: Strain rate predictions and $\dot{\epsilon}$ versus $\sinh(\sigma - \sigma_0)$ plot for system 1

7.14 Limestone

Superplastic deformation of limestone, reported in Ref. [77], was chosen for the analysis. Experimental parameters were: stress 1 MPa to 169.3 MPa, strain rate $5.2 \times 10^{-6} \text{ s}^{-1}$ to $6.4 \times 10^{-3} \text{ s}^{-1}$; grain size 4.2 μm ; temperature 973 K to 1173 K; reported value of activation energy $\sim 210 \text{ kJ.mol}^{-1}$. Equation 7.7 was used to describe the flow. The value of n varied from ~ 2 to ~ 4 ; grain boundary diffusion accommodated by GBS is suggested as the RCM. The limitations in the analysis are the same as in the other interpretations discussed earlier.

Results of the analysis using the m-GBS model are presented in Table 7.26. It can be seen that the tolerance levels are well below the permissible limit of an order of magnitude, the unit shear strain and the threshold stress for the onset of mesoscopic boundary sliding follow the expected trends with a change in the test temperature.

Table 7.26: Details of the strain-rate predictions using the m-GBS model

System	T, K	ΔF_0 kJ.mol ⁻¹	γ_0	σ_0 MPa	MT	SD	AE	CC
1	973	230.4	0.0727	12.9654	5.69	0.0267	0.0074	0.8449
	1073		0.0774	6.2727	6.17	0.0335	0.0093	0.8049
	1173		0.0824	0.9700	7.09	0.013	0.0041	0.8198

Table 7.27 presents the details of the analysis in terms of the constitutive Equation 7.1. It can be seen that very good values for the correlation coefficient are obtained vindicating the accuracy of the chosen equation.

Table 7.27: Fitting constants and the correlation coefficient for Equation 7.1

System	T_{hom}	Fitting constants		CC
		$P_1 \times 10^{-3}$	$P_2 \times 10^{-3}$	
1 Limestone	0.8862	28.5832	-754.261	0.81
	0.9772	67.666	-1004.58	0.79
	1.0683	37.3668	-14.7838	0.81

The detailed results are plotted in Figure 7.38.

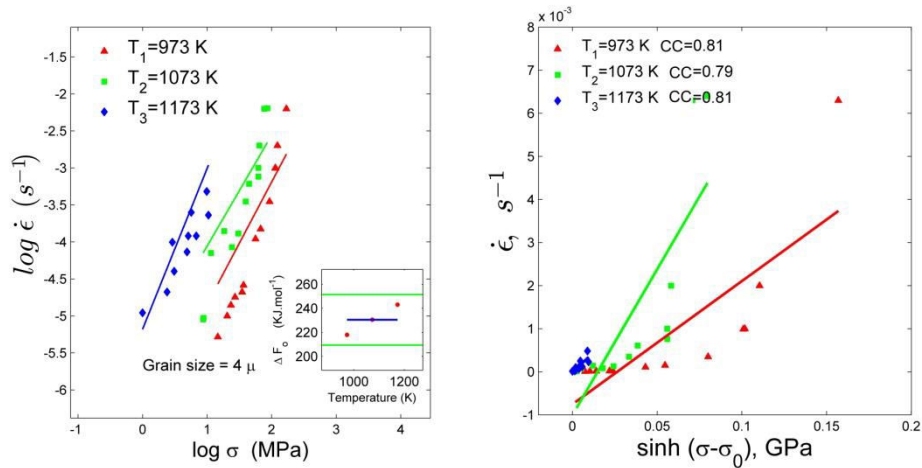


Figure 7.41: Strain rate predictions and $\dot{\epsilon}$ versus $\sinh(\sigma-\sigma_0)$ plot for system 1

7.15 Anorthite-Diopside

Superplastic deformation of two forms of synthetic Anorthite-Diopside, dry and wet [78], were analyzed. Experimental parameters were: grain size $\sim 3.05 \mu\text{m}$; temperature range 1273 K-1473 K; strain rate $0.6 \times 10^{-6} \text{ s}^{-1}$ to $71 \times 10^{-6} \text{ s}^{-1}$; stress from 15 MPa to 0.51 GPa; activation energy from 363 kJ.mol^{-1} to 571 kJ.mol^{-1} . GBS accommodated by dislocation is suggested to be the RCM. Power law creep, similar to Equation 7.7, was used for the analysis, but with the introduction of an additional pressure term, as in the case of Olivine, for obtaining the activation energy.

Table 7.28 presents the details of the analysis carried out in terms of the m-GBS model. It can be seen that good predictions have been made. The threshold stress for the onset of mesoscopic boundary sliding and the unit shear strain follow the expected trends with a change in the temperature of deformation.

Table 7.28: Details of the strain-rate predictions using the m-GBS model

System	T, K	ΔF_0 kJ.mol^{-1}	γ_0	σ_0 MPa	MT	SD	AE	CC
1	1323	329.2	0.4816	6.4683	1.08	0.0013	0.0005	0.9817
	1373		0.4845	4.5613	1.24	0.0010	0.0004	0.9977
	1423		0.4864	0.0165	1.45	0.0014	0.0006	0.9981
2	1223	311.5	0.4600	8.4240	1.12	0.0007	0.0003	0.9630
	1323		0.4657	5.0414	1.15	0.0015	0.0007	0.9986

1373	0.4695	2.2885	1.18	0.0026	0.0013	0.9955
------	--------	--------	------	--------	--------	--------

Table 7.29 presents the fitting constants for Equation 7.1 for both the Anorthite-Diopside systems and it can be seen that very good correlation coefficients have been obtained vindicating the choice of Equation 7.1 to describe optimal superplastic flow in the system.

Table 7.29: Fitting constants and the correlation coefficient for Equation 7.1

	System	T_{hom}	Fitting constants		CC
			$P_1 \times 10^{-3}$	$P_2 \times 10^{-3}$	
1	Anorthite-Diopside, dry	0.7257	0.0378	-1.3555	0.98
		0.7532	0.2756	-0.6525	0.99
		0.7806	0.8574	1.7636	0.99
2	Anorthite-Diopside, wet	0.6709	0.0206	0.1649	0.96
		0.7257	0.3665	-1.4907	0.99
		0.7532	1.2421	-5.9204	0.99

The detailed results are plotted in Figures 7.42 and 7.43.

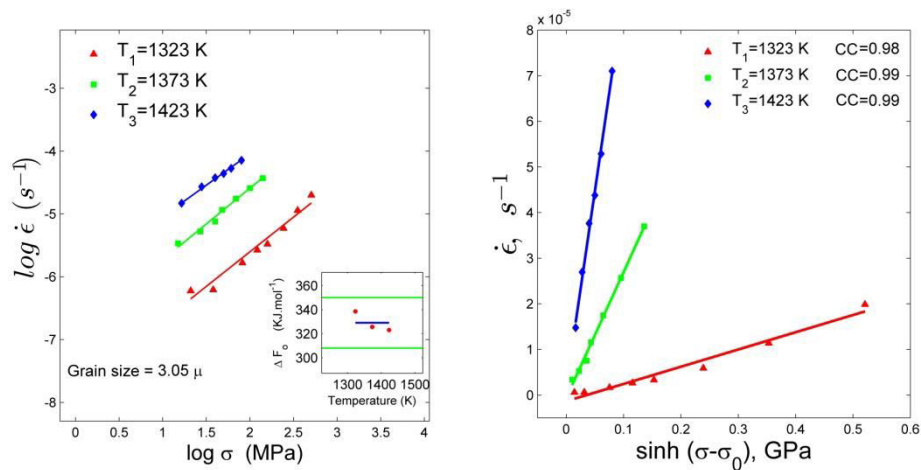


Figure 7.42: Strain rate predictions and $\dot{\epsilon}$ versus $\sinh(\sigma-\sigma_0)$ plot for system 1

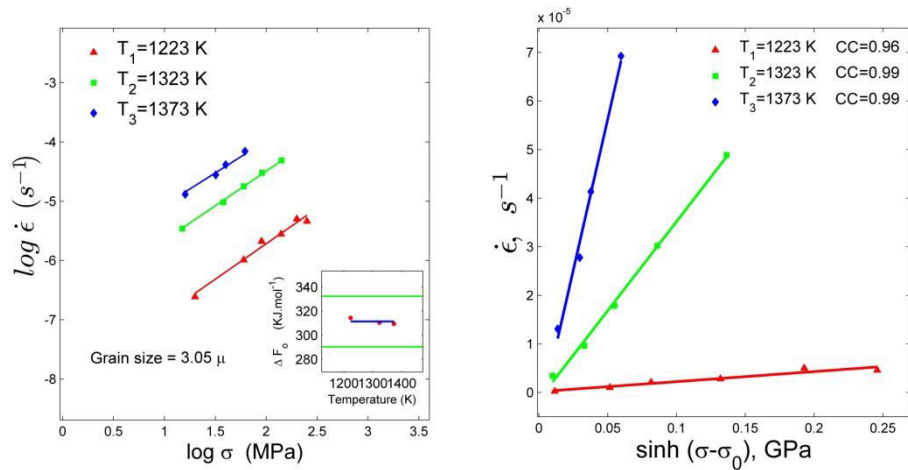


Figure 7.43: Strain rate predictions and $\dot{\epsilon}$ versus $\sinh(\sigma-\sigma_0)$ plot for system 1

7.16 Fine Grained Ice

Superplastic deformation of fine grained ice, reported in Ref. [79], was analyzed. Experimental parameters were: strain rate $28.1 \times 10^{-9} \text{ s}^{-1}$ to $3 \times 10^{-6} \text{ s}^{-1}$; stress 0.75 MPa to 7.8 MPa; grain size 10 μm ; temperature range 199 K to 220 K; reported value of activation energy is 49 kJ.mol^{-1} . Discussions on the mechanisms of superplastic deformation are speculative.

From Table 7.30 it can be seen that good predictions have been made using the m-GBS model. Consistent with Arrhenius kinetics, the predicted values of the free energy of activation at all temperatures were very close and the unit shear strain and the threshold stress for the onset of mesoscopic boundary sliding followed the expected trends with a change in temperature. However, the correlation coefficient obtained at one temperature was rather poor and this could be due to the significant scatter present in the experimental results at that temperature.

Table 7.28: Details of the strain-rate predictions using the m-GBS model

System	T, K	ΔF_0 kJ.mol^{-1}	γ_0	σ_0 MPa	MT	SD	AE	CC
1	199	53.1	0.0696	2.5228	1.46	0.0002	0.0001	0.9789
	219		0.0717	0.6170	3.33	0.0009	0.0003	0.4674
	220		0.0717	0.4192	4.77	0.0006	0.0002	0.9024

Table 7.29 presents the fitting constants in terms of Equation 7.1. Here also the correlation coefficient at the same single temperature is rather low. At the other two temperatures, however, good fits were obtained.

Table 7.31: Fitting constants and the correlation coefficient for Equation 7.1

System	T_{hom}	Fitting constants		CC
		P_1	$P_2 \times 10^{-3}$	
1 Fine grained ice	0.7285	0.0413	-0.8334×10^{-3}	0.97
	0.8018	0.1143	0.3918	0.46
	0.8054	0.4449	-0.2642	0.90

The detailed results are plotted in Figure 7.44.

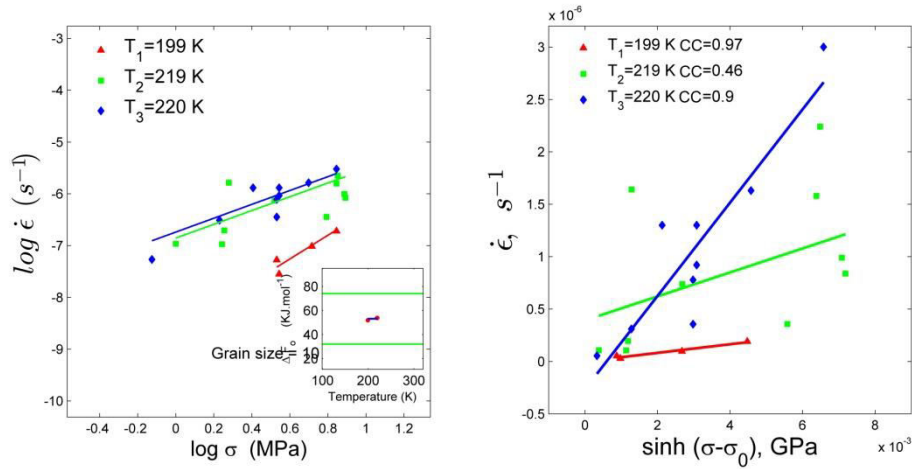


Figure 7.44: Strain rate predictions and $\dot{\epsilon}$ versus $\sinh(\sigma-\sigma_0)$ plot for system 1

7.17 Conclusion

Based on a detailed analysis involving 42 superplastic material systems, it could be concluded that the mesoscopic grain boundary sliding controlled flow model is able to describe optimal superplastic flow accurately with the help of two fitting constants, ΔF_0 and σ_0 . The model also suggests a way of calculating these two constants *ab initio*.

Historically, Backofen and coworkers [84] found many similarities between superplastic flow and that of hot polymers. Therefore, they chose to represent the flow of superplastics in terms of the well-known equation $\sigma = K \dot{\epsilon}^m$ or $\dot{\epsilon} = K_1 \sigma^n$, which is common in the polymer literature, and this description has persisted over several decades. This has meant that even in the optimal range (regions I and IIa of the isothermal $\log \sigma - \log \dot{\epsilon}$ curve), superplastic flow has to be represented as a non-linear curve (quadratic, as m is very low in region I, but rapidly rises in IIa). As a result of the present analysis, it has been possible to demonstrate that there is actually a linear relationship between the strain-rate and the “effective stress” ($\sigma - \sigma_0$); Equation 7.1). In the language of continuum mechanics, a material which obeys an equation similar to Equation 7.1 would be known as a Bingham solid. Therefore, it becomes possible to place the mechanics of optimal superplastic flow as a clearly defined domain within the field of Mechanics of Solids. Development of this

idea to obtain a yield criterion for optimal superplastic flow which has frame of reference indifference, e.g. the von Mises criterion in plasticity, then becomes possible. This aspect is beyond the scope of the present thesis.

8. Use of the m-GBS model for understanding the Inverse Hall-Petch effect

Hall-Petch (alternatively, grain boundary) strengthening is a phenomenon in the presence of which the yield stress of a material increases with decreasing grain size. Some of the earliest reported cases of the Hall-Petch effect can be found in Refs. [84,85]. The mathematical form of the Hall-Petch effect is represented as,

$$\sigma_y = \sigma_0 + \frac{k_y}{\sqrt{L}} \quad 8.1$$

However, below a certain grain size in the lower end of the nanometer range, inverse (or reverse) Hall-Petch effect comes into play and decreasing the grain size decreases the hardness or has an effect similar to that of increasing the temperature [3]. Inverse Hall-Petch (IHP) effect is often seen when the grain size is less than 10-15 nm (invariably below ~50 nm). As decreasing the grain size decreases hardness, it could be conjectured that creep/ superplasticity-like behavior could be observed even at room temperature, provided the grain size is on the lower end of the nanometer level. Based on a micromechanics approach, Refs [24,86] have presented an explanation for the IHP effect using a refined m-GBS controlled flow model.

Briefly, grain boundary sliding and crystallographic slip dominated deformation are essentially independent deformation mechanisms and the process that requires less stress for its commencement will be the favored deformation mode under a given set of experimental conditions. When crystallographic deformation is dominant, grain refinement will strengthen the material due to which the Hall-Petch effect is observed. However, when grain boundary sliding is dominant, the material will be weakened by grain refinement and hence inverse Hall-Petch effect is observed.

Chapters 5 and 7 contain a detailed description of the mesoscopic grain boundary sliding controlled flow model, as relevant to superplastic deformation. In brief, as mentioned earlier, the high-angle grain boundary is divided into a number of atomic scale ensembles that contain free volume. A basic sliding unit is constructed around each of these free volume sites. The basic sliding unit is assumed to lie symmetrically on either side of the

grain boundary. The basic sliding units are assumed to operate simultaneously, independent of each other. When the basic sliding units situated on a boundary slide sequentially, a boundary offset will result when the end of the boundary is reached. Such a sliding process (at a boundary) will get blocked at a steric hindrance, e.g., a triple junction. For substantial sliding to occur on a mesoscopic scale, two or more grain boundaries should join together to form a plane interface (by the flattening of the “hills” and “valleys” present along the grain boundaries), which by further interconnection with similar plane interfaces results in long range sliding. A portion of the energy supplied by the externally applied stress is used to form the plane interfaces, i.e. a long range threshold stress, τ_0 , should be overcome before the onset of mesoscopic boundary sliding. Mathematical development of the ideas leads to the conclusion that τ_0 is given by Equation 8.2 [24,26,30,31].

$$\tau_0 = \frac{2G\Gamma_B(\Delta A / A)}{\alpha_f \sqrt{NA}} \quad 8.2$$

For the calculations, the shape of the grain is assumed to be rhombic dodecahedron [27]. Therefore, the term ΔA in Equation 8.2 is given by Equation 8.3.

$$\Delta A = 2^{-2.5} L^2 \left(1 - \frac{2W\sqrt{6}}{L} \right) \quad 8.3$$

From Equation 8.3 it is obvious that $\Delta A=0$, when $L=L_0=2W6^{0.5}$. Considering $L_1=2^{1.5}3^{0.75}N\Gamma_B/(G\alpha_f)$, Equation 8.2 can be rewritten as Equations 8.4-8.6.

$$\tau_0 = G \left(\frac{L_1}{L} \left(1 - \frac{L_0}{L} \right) \right)^{0.5} ; \text{ when } L > L_0 \quad 8.4$$

$$\tau_0 = 0 ; \text{ when } L < L_0 \quad 8.5$$

$$\tau_0 = G \left(\frac{L_1}{L} \right)^{0.5} ; \text{ when } L \gg L_0 \quad 8.6$$

Details of the analysis: In this study, a total of 7 systems, displaying inverse Hall-Petch effect were analyzed using the m-GBS model. Four of them were intermetallics, one was quasi-crystalline and the other two were nanocrystalline systems [87–92]. Further, as the shear modulus for only two systems (one intermetallic and the other quasi-crystalline) were available, for the rest the data were extracted from the NIMS (National Institute of Materials Science, Tsukuba, Japan) database. In case of two (nanocrystalline) systems, computations were performed assuming the shear modulus to be 0.70G, 0.75G and 0.80G, where G is the shear modulus of the material when the grain size is in the micron range. (It is well known that the shear modulus decreases drastically (by ~ 20 - 30%) when the grain size is in the lower range of the nm scale [93]. The strain-rate of deformation in none of the hardness tests has been recorded. Therefore, following Ref. [94], the strain rate was assumed to lie in the range of $5 \times 10^{-4} \text{ s}^{-1}$ to $5 \times 10^{-2} \text{ s}^{-1}$. Therefore, the free energy of activation was computed for these extreme values. Using the computed values of the free energy of activation, the unit shear strain values were refined. The procedure adopted is explained below in detail.

Procedure adopted: The relationship between the steady state hardness, H_v , and the instantaneous hardness, H_0 , is as shown in Equation 8.7 [24,86].

$$H_v = H_0 - \frac{m_2}{L} (L - L_0)^{0.5} \quad 8.7$$

Hence, m_2 is the slope of the plot of H_v versus $(L - L_0)^{0.5}/L$ and is equal to $GL_1^{0.5}/C$. Here, C (≈ 3) is the conversion factor from hardness to tensile stress, as the material yield behavior is assumed to be that of a von Mises solid [49]. N , which is assumed to be a constant within the narrow grain size range, is computed using the value of L_1 , already defined as $L_1 = 2^{1.5} 3^{-0.75} N \Gamma_B / (G \alpha_f)$. (Strictly, over a large range of grain size and temperature, N is a strong function of both grain size and temperature. Here the temperature is kept constant and so the approximation of L_1 to be a constant is only over a small grain size range). The values of Γ_B is approximated as 1 J.m^{-2} [23,25,26] and the form factor, α_f is taken as ~unity. The computed value of L_1 is used in Equation 8.7 to compute the hardness equivalent of the threshold stress needed for the onset of mesoscopic GBS (the second term on the RHS of Equation 8.7). Alternatively, the long

range threshold shear stress, τ_0 , can also be computed using Equation 8.4. Equations 8.8 and 8.9, which result from a mathematical development of the ideas concerning the m-GBS model [22,23,95,96] are used to compute the free energy of activation for the rate controlling process and the refined values of γ_0 , for the strain rate values given above (see Chapters 5 and 7 also).

$$\dot{\gamma} = \frac{2W\gamma_0v}{L} \sinh\left(\frac{(\tau - \tau_0)\gamma_0 V_0}{2kT}\right) \exp\left(-\frac{\Delta F_0}{kT}\right) \quad 8.8$$

$$\Delta F_0 = (\beta_1\gamma_0^2 + \beta_2\varepsilon_0^2)GV_0 \quad 8.9$$

It can be readily seen that the values of ΔF_0 and σ_0 are inter-dependent. Therefore, their stable values are obtained by iteration.

Results and discussion: The results of the analysis are presented in Table 8.1.

Table 8.1: Results of the analysis								
N	L, nm	τ_0 , GPa	γ_0	ΔF_0 , kJ.mol ⁻¹				
				$\dot{\gamma} = 5 \times 10^{-2} \text{s}^{-1}$	$\dot{\gamma} = 5 \times 10^{-4} \text{s}^{-1}$			
System: Al 25Cu 12.5Fe, G=74GPa [87]								
1.4	38.8	1.36						
	23.6	1.68	0.0688	184	197			
	20.6	1.78						
	17.6	1.89						
System: Ni 18Fe, G=79.2GPa [88]								
18.0	13.9	0.95	0.70G	0.0795				
20.7	12.7	0.98	0.75G	0.0768	117			
23.6	11.0	1.03	0.80G	0.0743				
System: Zn, G=43GPa [89]								
7.8	11.0	0.92	0.70G	0.0812				
8.9	7.9	0.99	0.75G	0.0784	85			
10.1	6.0	1.00	0.80G	0.0758	98			
System: TiAl, G=61.8GPa [90]								
75.7x10 ⁻³	21.4	3.62						
	18.7	3.82						
	17.1	3.94	0.0698	202	214			
	12.5	4.38						
	12.1	4.42						
	11.0	4.55						
System: NiAl ₃ , G=50.6GPa [86]								

15.4x10 ⁻³	60.9	2.81	0.0925	146	158
	53.0	3.00			
	49.4	3.10			
	45.0	3.24			
	42.0	3.34			
25.6	4.17				
System: NbAl ₃ , G=15.4GPa [91]					
1.8x10 ⁻³	34.0	3.43	0.1475	185	198
	30.4	3.60			
	27.0	3.79			
	25.4	3.88			
	22.0	4.12			
System: Al ₅ Fe ₂ , G=61.8GPa [92]					
0.85	32.0	1.52	0.0711	158	170
	23.6	1.73			
	11.0	2.27			
	10.0	2.33			

When the correlation coefficient between the measured and the predicted values of H_v (Equation 8.7; prediction: H_v versus $(L-L_0)^{0.5}/L$ is linear) was calculated, in all cases, but one, the value of the correlation coefficient was >0.9 . But, in case of Ni18Fe it was ~ 0.8 . This is good support for the usefulness of the m-GBS model in explaining the inverse Hall-Petch Effect. However, it was also found that the correlation coefficient had similar values if hardness versus $\log(L)$ or hardness versus L was plotted [19, 20]. These values are also presented in Table 8.2.

Table 8.2: Results of the analysis

System	L, nm	H_v , GPa	Correlation coefficient for H_v versus		
			Log (L)	L	$(L-L_0)^{0.5}/L$
1 Al 25Cu 12.5Fe [87]	38.8	11.41	0.95	0.92	0.96
	23.6	10.46			
	20.6	9.31			
	17.6	8.56			
2 Ni 18Fe [88]	13.9	6.15	0.79	0.81	0.78
	12.7	5.70			
	11.0	5.71			
3 Zn [89]	11.0	1.06	0.99	0.98	0.99
	7.9	0.84			
	6.0	0.58			
4 TiAl [90]	21.4	12.08	0.99	0.99	0.99
	18.7	11.25			
	17.1	10.69			

		12.6	8.50			
		12.1	8.25			
		11.0	7.08			
		60.9	11.47			
		53.0	10.72			
5	NiAl ₃ [86]	49.4	10.06	0.99	0.99	0.99
		45.0	8.67			
		42.0	8.06			
		25.6	4.50			
		34.0	10.28			
		30.4	9.86			
6	NbAl ₃ [91]	27.0	9.36	0.90	0.88	0.91
		25.4	9.14			
		22.0	6.42			
		32.0	8.78			
7	Al ₅ Fe ₂ [92]	23.6	8.08	0.97	0.95	0.97
		11.0	5.69			
		10.0	4.17			

This last finding clearly underlines the risk of choosing a physics-based/ atomistic model based solely on macroscopic correlations. However, in the analysis of Conrad and Naryan [97,98] (where H_v is a function of L or $\log(L)$, depending on the degree of approximation employed), the effective stress is taken as equal to the applied stress, i.e. the strain rate sensitivity index, $m=1$. But, in nanocrystalline systems, particularly under the conditions of the present tests, the value of m is in the range of 0.02 to 0.08 [99], which brings into question the relevance of the model presented in [90, 91]. In contrast, in the m -GBS model, depending on the experimental conditions, m can range from very low values to unity and it is readily seen that for the sets of data analyzed in this chapter m is in the range required by the experiments.

In Table 8.1, a significant spread in the value of N is observed, i.e., from 0.076 to 23.4. It is noteworthy that values of N distinctly greater than unity are seen only when the grain size is less than 15 nm, which is where the role of diffusion in accommodation of the GBS is likely to be significant. It is yet another supporting piece of evidence for the m -GBS model. Moreover, the values of the unit shear strain in case of all the systems are close to ~ 0.1 , the approximate value suggested by the bubble raft experiments and MD simulations [30,31].

9. Conclusions and suggestions for future work

Conclusions:

1. Universality in the mechanical response of superplastic materials is demonstrated using the dimensionless parameters: $\sigma/\sigma_{\text{opt}} - \dot{\epsilon}/\dot{\epsilon}_{\text{opt}} - m/m_{\text{opt}} - \Delta F_0/T_m - \eta_{\text{app}}/\eta_{\text{abs}}$. It is shown that the sigmoidal $\log(\sigma)$ versus $\log(\dot{\epsilon})$ curve, when both the stress and the strain-rate are normalized with respect to their optimal values for all the materials, a universal curve results, which is independent of the material involved. Fits were attempted for the normalized stress, strain-rate and temperature data for the different systems in terms of
 - a. The equation often used to describe superplasticity in the literature, viz. $\dot{\epsilon} \propto \sigma$ with $m = 0.5$ and
 - b. The m-GBS controlled flow model proposed from our research group. A good fit of 0.95 was obtained for the m-GBS model, while the fit was poor at 0.7 for the model based on the Dorn equation, with $m = 0.5$.
 - c. When the stress, strain-rate and temperature data for the different systems are fitted using a 2nd order regression equation also a good coefficient of correlation of 0.96 was obtained. But, such a regression equation lacks physical significance. Thus, the universality in the sigmoidal nature of stress versus strain-rate curve for superplastic deformation for different materials could be established.

When the “absolute” viscosity was computed for the ideal case of $n = 1$ in the normalized stress-strain rate space and that value was used to normalize the apparent viscosity at different stress levels, temperatures etc., for different materials, a good correlation coefficient of ~ 0.95 was obtained for the normalized viscosity versus the normalized strain-rate versus temperature plot, presented as a universal curve.

It had already been shown in an earlier work that when the strain-rate sensitivity index is normalized with respect to its optimal value and plotted against the normalized strain-rate, a universal curve resulted which involved many systems. This was re-established in this work using more data points. Here, in addition the effect of temperature on the value of m was also considered as the third variable.

It was seen that the correlation coefficient in two dimensions, i.e. normalized strain rate sensitivity index versus normalized strain rate, was significantly higher than for the three dimensional case, i.e. normalized strain rate sensitivity index versus normalized strain rate versus normalized temperature. It is suggested that, as methods for determining the strain rate sensitivity index do influence its value and as values reported by various investigators have been considered for the analysis here, a correlation coefficient of ~ 0.80 only could result for the three dimensional case, whereas the minimum correlation coefficient in two dimensions was ~ 0.90 .

It could also be seen that when the free energy of activation for the rate controlling process, ΔF_0 is normalized with respect to RT_m , a very similar / comparable value is obtained for many superplastic systems. As the strength of the inter-atomic bonds is proportional to the melting temperature, if optimal superplasticity arises in the different material systems because of the same rate controlling process (of m-GBS, in our view), it would stand to reason that the ratio ($\Delta F_0/RT_m$) is nearly constant for the different systems, which again is a demonstration of the universality of the phenomenon of superplasticity.

2. The mesoscopic-grain boundary sliding controlled flow model for superplastic deformation has been shown to be applicable to systems of a wide range of grain sizes ranging from 65 nm to 24 μm , to different classes of materials including metals and alloys, intermetallics, ceramics, geological materials, ice, metals with a quasi-crystalline phase, metals of a quasi-single phase and also over a wide range of strain-rates ranging from $\sim 10^{-6} \text{ s}^{-1}$ to $\sim 10 \text{ s}^{-1}$ and temperature ranges. Although predictions within an order of magnitude are considered to be very good in studies of this kind, most of the predictions were well within the limiting factor of 10. Also, the unit shear strain associated with unit boundary sliding event followed the expected trend of increasing with increasing temperature in all the cases. The long-range threshold stress for the onset of mesoscopic boundary sliding followed the expected trend of decreasing magnitude with increasing temperature in all but for one ZrO_2 system at one temperature. This exception could be due to inaccuracies in the experimental measurements. The free energy of activation for similar materials, calculated from the experimental data reported by different

investigators turn out to be similar/ comparable, as should be the case in a sound analysis.

3. Mesoscopic-grain boundary sliding has been used to satisfactorily explain the phenomenon of inverse Hall-Petch effect. Seven systems exhibiting IHP were considered here for the analysis. Although, the correlation coefficient in different cases i.e. H_v versus $\log(L)$, L (these first two corresponding to a model due to Conrad and Narayan) and $(L-L^0)^{0.5}/L$ (for the mesoscopic GBS model) was similar and good in all the cases, this study demonstrates the risk inherent in choosing atomistic models based solely on macroscopic correlations. Unlike in the model of Conrad and Narayan, where effective stress and the applied stress are considered to be the same, which makes $m = 1$ (totally unsupported by experimental data), using the m-GBS model to analyze the experimental data can account for the low values of m found in the experimental studies.

Future work:

1. It is planned to use the mathematical form of the m-GBS model as the constitutive equation for developing FEM packages for industrial forming processes that exploit superplasticity. This will allow variations in the m values during forming to be taken into account, essential for efficient process control.
2. As GBS control has been shown to be a mechanism distinct from diffusion control, it is proposed to identify regions of GBS control in deformation mechanism maps, beginning with the material, Nickel, for which sufficient data exist.
3. It is proposed to construct the universal maps for superplastic deformation in much greater detail by analyzing more systems belonging to different classes of material. This way, it is hoped that the dependence on the experimental variables of the phenomenon of superplasticity will be brought out very clearly.

10. References

- [1] C. Pearson et al. The Viscous Properties of Extruded Eutectic Alloys of Lead-Tin and Bismuth-Tin. *Journal of the Institute of Metals*, 54 (1934) 111–124.
- [2] T.G. Langdon, J. Wadsworth, Superplasticity in Advanced Materials, in: S. Hori, M. Tokzane, N. Furushiro (Eds.), Osaka JSRS, Japan Society for Research on Superplasticity, Osaka, Japan, 1991: p. 847.
- [3] K.A. Padmanabhan, R.A. Vasin, F.U. Enikeev, Superplastic Flow: Common Basis for a Ubiquitous Phenomenon, Springer, 2001.
- [4] J.Y. Huang, S. Chen, Z.Q. Wang, K. Kempa, Y.M. Wang, S.H. Jo, G. Chen, M.S. Dresselhaus, Z.F. Ren, Superplastic Carbon Nanotubes, *Nature*. 439 (2006) 281–281.
- [5] B. Gun, K.J. Laws, M. Ferry, Superplastic flow of a Mg-based Bulk Metallic Glass in the Supercooled Liquid Region, *Journal of Non-Crystalline Solids*. 352 (2006) 3896–3902.
- [6] J. Buenz, K.A. Padmanabhan, G. Wilde, On the Applicability of a Mesoscopic Interface Sliding Controlled Model for Understanding Superplastic Flow in Bulk Metallic Glasses, *Intermetallics*. 60 (2015) 50–57.
- [7] K.A. Padmanabhan, H. Gleiter, A Mechanism for the Deformation of Disordered States of Matter, *Current Opinion in Solid State and Material Science*. 16 (2012) 243–253.
- [8] H. Watanabe, T. Mukai, K. Ishikawa, M. Mabuchi, K. Higashi, Realization of high-strain-rate superplasticity at low temperatures in a Mg–Zn–Zr alloy, *Mater. Sci. Eng. A*. 307 (2001) 119–128.
- [9] K.A. Padmanabhan, G.J. Davies, Superplasticity: mechanical and structural aspects, environmental effects, fundamentals and applications, Springer-Verlag, 1980.
- [10] J.W. Edington, K.N. Melton, C.P. Cutler, Superplasticity, *Prog. Mater. Sci.* 21 (1976) 61–170.
- [11] R.A. Vasin, F.U. Enikeev, M.I. Mazurski, Method to determine the strain-rate sensitivity of a superplastic material from the initial slopes of its stress–strain curves, *J. Mater. Sci.* 33 (1998) 1099–1103.

- [12] D. Wilkinson, Grain size effects in superplasticity, in: B. Baudelet, M. Suery (Eds.), Superplasticity, Centre National de la Recherche Scientifique, Paris, 1985: pp. 1–13.
- [13] H.J. Frost, M.F. Ashby, Deformation-mechanism maps: the plasticity and creep of metals and ceramics, Pergamon Press, 1982.
- [14] R.L. Stocker, M.F. Ashby, On the empirical constants in the dorn equation, *Scr. Metall.* 7 (1973) 115–120.
- [15] K.A. Padmanabhan, J. Leuthold, G. Wilde, S.S. Bhattacharya, On the power law description of low-stress uni-axial steady-state high-homologous-temperature deformation, *Mech. Mater.* 91, Part 1 (2015) 177–193.
- [16] L.N. McCartney, Constitutive relations describing creep deformation for multi-axial time-dependent stress states, *J. Mech. Phys. Solids.* 29 (1981) 13–33.
- [17] F.R.N. Nabarro, Do we have an acceptable model of power-law creep?, *Mater. Sci. Eng. A.* 387–389 (2004) 659–664.
- [18] R.W. Rohde, J.C. Swearingen, Mechanical Testing for Deformation Model Development: A Symposium Sponsored by ASTM Committee E-28 on Mechanical Testing, Bal Harbour, Fla., 12-13 Nov. 1980, ASTM International, 1982.
- [19] T.G. Nieh, J. Wadsworth, O.D. Sherby, Superplasticity in Metals and Ceramics, Cambridge University Press, 1997.
- [20] O.A. Kaibyshev, Superplasticity of Alloys, Intermetallides, and Ceramics, Springer-Verlag, 1992.
- [21] K.A. Padmanabhan, A theory of structural superplasticity, *Mater. Sci. Eng.* 29 (1977) 1–18.
- [22] K.A. Padmanabhan, Grain boundary sliding controlled flow and its relevance to superplasticity in metals, alloys, ceramics and intermetallics and strain-rate dependent flow in nanostructured materials, *J. Mater. Sci.* 44 (2009) 2226–2238.
- [23] K.A. Padmanabhan, H. Gleiter, Optimal structural superplasticity in metals and ceramics of microcrystalline- and nanocrystalline-grain sizes, *Mater. Sci. Eng. A.* 381 (2004) 28–38.
- [24] H. Hahn, K.A. Padmanabhan, A model for the deformation of nanocrystalline materials, *Philos. Mag. Part B.* 76 (1997) 559–571.

- [25] T.A. Venkatesh, S.S. Bhattacharya, K.A. Padmanabhan, J. Schlipf, Model for grain boundary sliding and its relevance to optimal structural superplasticity, *Mater. Sci. Technol.* 12 (1996) 635–643.
- [26] K.A. Padmanabhan, J. Schlipf, Model for grain boundary sliding and its relevance to optimal structural superplasticity Part 1 – Theory, *Mater. Sci. Technol.* 12 (1996) 391–399.
- [27] J. (ed) Gittus, Creep, viscoelasticity, and creep fracture in solids, in: Applied Science, 1975.
- [28] T.G. Nieh, L.M. Hsiung, J. Wadsworth, R. Kaibyshev, High strain rate superplasticity in a continuously recrystallized Al–6%Mg–0.3%Sc alloy, *Acta Mater.* 46 (1998) 2789–2800.
- [29] J.D. Eshelby, The Determination of the Elastic Field of an Ellipsoidal Inclusion, and Related Problems, *Proc. R. Soc. Lond. Ser. Math. Phys. Sci.* 241 (1957) 376–396.
- [30] D. Wolf, Structure-energy correlation for grain boundaries in F.C.C. metals—III. Symmetrical tilt boundaries, *Acta Metall. Mater.* 38 (1990) 781–790.
- [31] D. Wolf, Structure-energy correlation for grain boundaries in f.c.c. metals—IV. Asymmetrical twist (general) boundaries, *Acta Metall. Mater.* 38 (1990) 791–798.
- [32] S. Sripathi, K.A. Padmanabhan, On the experimental validation of a mesoscopic grain boundary sliding-controlled flow model for structural superplasticity, *J. Mater. Sci.* 49 (2014) 199 – 210
- [33] F.A. Mohamed, M.M.I. Ahmed, T.G. Langdon, Factors influencing ductility in the superplastic Zn-22 Pct Al eutectoid, *Metall. Trans. A.* 8 (1977) 933–938.
- [34] N. Kumar, K.S. Raman, D.H. Sastry, E.A. Little, Investigation of superplasticity by the impression creep technique, *J. Mater. Sci.* 25 (1990) 753–755.
- [35] F. Musin, R. Kaibyshev, Y. Motohashi, G. Itoh, High strain rate superplasticity in a commercial Al–Mg–Sc alloy, *Scr. Mater.* 50 (2004) 511–516.
- [36] S. Komura, Z. Horita, M. Furukawa, M. Nemoto, T.G. Langdon, An evaluation of the flow behavior during high strain rate superplasticity in an Al-Mg-Sc alloy, *Metall. Mater. Trans. A.* 32 (2001) 707–716.
- [37] H. Watanabe, T. Mukai, K. Ishikawa, T. Mohri, M. Mabuchi, K. Higashi, Superplasticity of a Particle-Strengthened WE43 Magnesium Alloy, *Mater. Trans.* 42 (2001) 157–162.

- [38] J. Babu, A. Dutta, Low temperature superplasticity through grain refinement in Ti-6Al-4V by a novel route of quench-roll-recrystallise, *J. Mater. Res. Technol.* 4 (2015) 348–352.
- [39] R.A. Vasin, V.K. Berdin, R.M. Kashaev, On the Universal Curve in Superplasticity Mechanics, *Strength Mater.* 33 (2001) 509–515.
- [40] A. Smolej, B. SkAzA, M. FAzArinc, Determination of the strain-rate sensitivity and the activation energy of deformation in the superplastic aluminium alloy Al-Mg-Mn-Sc Določevanje indeksa občutljivosti na preoblikovalno hitrost in aktivacijske energije za deformacijo superplastične aluminijeve, *Orig. Sci. Pap. Znan. Članki Determ. Strain-Rate Sensit. Act. Energy Deform. Superplast. Alum. Alloy Al-Mg-Mn-Sc.* 56 (2009) 389–399.
- [41] S. Fernandez, M.J.Q. Hernández, J.O. García, L.F.V. González, R. González, J.V. González, Superplasticity of ultrafine grained low-alloy steels, *Mem. Trab. Difus. Científica Téc.* (2012) 45–56.
- [42] K.A. Padmanabhan, G.J. Davies, Numerical analysis of superplasticity data for use in metal forming applications, *J. Mech. Phys. Solids.* 18 (1970) 261–275.
- [43] Y. Kawamura, T. Nakamura, A. Inoue, T. Masumoto, High-Strain-Rate Superplasticity due to Newtonian Viscous Flow in La₅₅Al₂₅Ni₂₀ Metallic Glass, *Mater. Trans. JIM.* 40 (1999) 794–803.
- [44] I. Charit, R.S. Mishra, Low temperature superplasticity in a friction-stir-processed ultrafine grained Al-Zn-Mg-Sc alloy, *Acta Mater.* 53 (2005) 4211–4223.
- [45] S.-A. Shei, T.G. Langdon, The mechanical properties of a superplastic quasi-single phase copper alloy, *Acta Metall.* 26 (1978) 639–646.
- [46] H. Yan, R. Chen, E. Han, Superplasticity of Mg-5.8Zn-1Y-Zr alloy sheet fabricated by combination of extrusion and hot-rolling processes, *Sci. China Ser. E Technol. Sci.* 52 (2009) 166–171.
- [47] W.-Y. Kim, S. Hanada, T. Takasugi, Flow behavior and microstructure of Co₃Ti intermetallic alloy during superplastic deformation, *Acta Mater.* 46 (1998) 3593–3604.
- [48] T.G. Nieh, J. Wadsworth, Microstructural characteristics and deformation properties in superplastic intermetallics, *Mater. Sci. Eng. A.* 239–240 (1997) 88–96.

- [49] T.G. Langdon, Grain boundary sliding revisited: Developments in sliding over four decades, *J. Mater. Sci.* 41 (2006) 597–609.
- [50] T.G. Langdon, A unified approach to grain boundary sliding in creep and superplasticity, *Acta Metall. Mater.* 42 (1994) 2437–2443.
- [51] D.W. Chung, J.R. Cahoon, Superplasticity in aluminium-silicon eutectic, *Met. Sci.* 13 (1979) 635–640.
- [52] K. Matsuki, K. Minami, M. Tokizawa, Y. Murakami, Superplastic behaviour in nominally single-phase and two-phase Al-Cu alloys., *Met. Sci.* 13 (1979) 619–626.
- [53] S. Fujino, N. Kuroishi, M. Yoshino, T. Mukai, Y. Okanda, K. Higashi, High-strain-rate superplastic behavior in a super-rapidly-solidified Al-Si system alloy, *Scr. Mater.* 37 (1997) 673–678.
- [54] T. Wang, J. Huang, High Strain Rate Superplasticity in 6061 Alloy with 1% SiO₂ Nano-Particles, *Mater. Trans.* 42 (2001) 1781–1789.
- [55] Y. Nishida, I. Sigematsu, H. Arima, J.-C. Kim, T. Ando, Superplasticity of SiC whisker reinforced 7075 composite processed by rotary-die equal-channel angular pressing, *J. Mater. Sci. Lett.* 21 (2002) 465–468.
- [56] R. Kaibyshev, E. Avtokratova, A. Apollonov, R. Davies, High strain rate superplasticity in an Al–Mg–Sc–Zr alloy subjected to simple thermomechanical processing, *Scr. Mater.* 54 (2006) 2119–2124.
- [57] Y. Kim, D. Bae, Superplasticity in a Fine-Grained Mg-Zn-Y-Zr Alloy Containing Quasicrystalline Particles, *Mater. Trans.* 45 (2004) 3298–3303.
- [58] G. m. Xie, Z. y. Ma, L. Geng, R. s. Chen, Microstructural evolution and enhanced superplasticity in friction stir processed Mg–Zn–Y–Zr alloy, *J. Mater. Res.* 23 (2008) 1207–1213.
- [59] G. Wegmann, R. Gerling, F.-P. Schimansky, H. Clemens, A. Bartels, High-temperature mechanical properties of hot isostatically pressed and forged gamma titanium aluminide alloy powder, *Intermetallics.* 10 (2002) 511–517.

- [60] J. Sun, Y.H. He, J.S. Wu, Characterization of low-temperature superplasticity in a thermomechanically processed TiAl based alloy, *Mater. Sci. Eng. A*. 329–331 (2002) 885–890.
- [61] J. Warren, L.M. Hsiung, H.N.G. Wadley, High temperature deformation behavior of physical vapor deposited Ti-6Al-4V, *Acta Metall. Mater.* 43 (1995) 2773–2787.
- [62] T.G. Nieh, W.C. Oliver, Superplasticity of a nickel silicide, Ni₃Si, *Scr. Metall.* 23 (1989) 851–854.
- [63] F. Wakai, T. Nagano, Effects of solute ion and grain size on superplasticity of ZrO₂ polycrystals, *J. Mater. Sci.* 26 (1991) 241–247.
- [64] G.Q. Tong, K.C. Chan, L. Gao, Z.R. Lin, The grain size dependency of compressive deformation of a superplastic 3 mol% yttria stabilized tetragonal zirconia, *Mater. Sci. Eng. A*. 336 (2002) 263–269. doi:10.1016/S0921-5093(01)01985-2.
- [65] A.A. Sharif, M.L. Mecartney, Superplasticity in cubic yttria-stabilized zirconia with intergranular silica, *Acta Mater.* 51 (2003) 1633–1639.
- [66] M. Yoshida, Y. Shinoda, T. Akatsu, F. Wakai, Superplasticity-like Deformation of Nanocrystalline Monoclinic Zirconia at Elevated Temperatures, *J. Am. Ceram. Soc.* 87 (2004) 1122–1125.
- [67] A.A. Sharif, M.L. Mecartney, Superplasticity in cubic yttria stabilized zirconia with 10 wt.% alumina, *J. Eur. Ceram. Soc.* 24 (2004) 2041–2047.
- [68] T. Chen, M.L. Mecartney, A High-Strain-Rate Alumina-Based Ceramic Composite, *J. Am. Ceram. Soc.* 88 (2005) 1004–1006.
- [69] T. Chen, F.A. Mohamed, M.L. Mecartney, Threshold stress superplastic behavior and dislocation activity in a three-phase alumina–zirconia–mullite composite, *Acta Mater.* 54 (2006) 4415–4426.
- [70] R.P. Dillon, D.-K. Kim, J.E. Trujillo, W.M. Kriven, M.L. Mecartney, Creep characteristics of alumina, nickel aluminate spinel, zirconia composites, *J. Mater. Res.* 23 (2008) 556–564.
- [71] X. Xu, T. Nishimura, N. Hirosaki, R.-J. Xie, Y. Yamamoto, H. Tanaka, Superplastic deformation of nano-sized silicon nitride ceramics, *Acta Mater.* 54 (2006) 255–262.

- [72] B.S. Bokshstein, S.Z. Bokshstein, A.A. Zhukhovitskiĭ, Thermodynamics and kinetics of diffusion in solids, Oxonian Press, 1985.
- [73] A. Kelly, Strong Solids, Clarendon P., 1966.
- [74] W.F. Gale, T.C. Totemeier, Smithells Metals Reference Book, Butterworth-Heinemann, 2003.
- [75] A.S. Argon, Plastic deformation in metallic glasses, *Acta Metall.* 27 (1979) 47–58.
- [76] L.N. Hansen, M.E. Zimmerman, D.L. Kohlstedt, Grain boundary sliding in San Carlos olivine: Flow law parameters and crystallographic-preferred orientation, *J. Geophys. Res. Solid Earth.* 116 (2011) B08201.
- [77] S.M. Schmid, Rheological evidence for changes in the deformation mechanism of Solenhofen limestone towards low stresses, *Tectonophysics.* 31 (1976) T21–T28.
- [78] A. Dimanov, E. Rybacki, R. Wirth, G. Dresen, Creep and strain-dependent microstructures of synthetic anorthite–diopside aggregates, *J. Struct. Geol.* 29 (2007) 1049–1069.
- [79] W.B. Durham, L.A. Stern, S.H. Kirby, Rheology of ice I at low stress and elevated confining pressure, *J. Geophys. Res. Solid Earth.* 106 (2001) 11031–11042.
- [80] G.E. Dieter, D. Bacon, Mechanical Metallurgy, McGraw-Hill, 1988.
- [81] F.A. Mohamed, T.G. Langdon, Deformation mechanism maps based on grain size, *Metall. Trans.* 5 (1974) 2339–2345.
- [82] S.J. Rothman, N.L. Peterson, L.J. Nowicki, L.C. Robinson, Tracer Diffusion of Magnesium in Aluminum Single Crystals, *Phys. Status Solidi B.* 63 (1974) K29–K33.
- [83] S.C. Cheng, J. Wolfenstine, O.D. Sherby, Superplastic behavior of two-phase titanium aluminides, *Metall. Trans. A.* 23 (1992) 1509–1513.
- [84] W.A. Backofen, I.R. Turner, D.H. Avery, Superplasticity in an Al-Zn alloy, *Trans ASM.* 57 (1964) 980–990.
- [85] E.O. Hall, The Deformation and Ageing of Mild Steel: III Discussion of Results, *Proc. Phys. Soc. Sect. B.* 64 (1951) 747.

- [86] N. Petch, The cleavage strength of polycrystals, *J Iron Steel Inst.* 174 (1953) 25–28.
- [87] K.A. Padmanabhan, R. Nitsche, H. Hahn, On the Deformation of Nanocrystalline Metals and Ceramics, in: *Fourth Eur. Conf Adv. Mater. Process.*, Associazione Italiana Di Metallurgia, Milano, 1995: pp. 289–298.
- [88] N.K. Mukhopadhyay, F. Ali, S. Scudino, M.S. Khoshkhoo, M. Stoica, V.C. Srivastava, V. Uhlenwinkel, G. Vaughan, C. Suryanarayana, J. Eckert, Grain size softening effect in Al_{62.5}Cu₂₅Fe_{12.5} nanoquasicrystals, *Appl. Phys. Lett.* 103 (2013) 201914.
- [89] C. Cheung, F. Djuanda, U. Erb, G. Palumbo, Electrodeposition of nanocrystalline Ni-Fe alloys, *Nanostructured Mater.* 5 (1995) 513–523.
- [90] K.A. Padmanabhan, Mechanical properties of nanostructured materials, *Mater. Sci. Eng. A.* 304–306 (2001) 200–205.
- [91] H. Chang, H.J. Höfler, C.J. Altstetter, R.S. Averback, Synthesis, processing and properties of nanophase TiAl, *Scr. Metall. Mater.* 25 (1991) 1161–1166.
- [92] D.K. Kim, K. Okazaki, Nano-Crystalline Consolidation of MA Powders by EDC, *Mater. Sci. Forum.* 88–90 (1992) 553–560.
- [93] M.R. Basariya, V.C. Srivastava, N.K. Mukhopadhyay, Inverse Hall–Petch like behaviour in a mechanically milled nanocrystalline Al₁₅Fe₂ intermetallic phase, *Philos. Mag.* (2016) 1–12.
- [94] M. Grewer, J. Markmann, R. Karos, W. Arnold, R. Birringer, Shear softening of grain boundaries in nanocrystalline Pd, *Acta Mater.* 59 (2011) 1523–1529.
- [95] V. Maier, K. Durst, J. Mueller, B. Backes, H.W. Höppel, M. Göken, Nanoindentation strain-rate jump tests for determining the local strain-rate sensitivity in nanocrystalline Ni and ultrafine-grained Al, *J. Mater. Res.* 26 (2011) 1421–1430.
- [96] K.A. Padmanabhan, M.I.R. Basariya, A mesoscopic grain boundary sliding controlled flow model for superplasticity in intermetallics, *Int. J. Mater. Res. Former. Z. Fuer Met.* 100 (2009) 1543–1551

- [97] K.A. Padmanabhan, M.R. Basariya, Mesoscopic grain boundary sliding as the rate controlling process for high strain rate superplastic deformation, *Mater. Sci. Eng. A.* 527 (2009) 225–234.
- [98] H. Conrad, J. Narayan, Mechanism for grain size softening in nanocrystalline Zn, *Appl. Phys. Lett.* 81 (2002) 2241–2243.
- [99] H. Conrad, J. Narayan, Mechanisms for grain size hardening and softening in Zn, *Acta Mater.* 50 (2002) 5067–5078.
- [100] S. Varam, K.V. Rajulapati, K. Bhanu Sankara Rao, Strain rate sensitivity studies on bulk nanocrystalline aluminium by nanoindentation, *J. Alloys Compd.* 585 (2014) 795–799.

Universality of the Phenomenology of Structural Superplasticity

Sriharsha Sripathi^{1, a *} and K. A Padmanabhan^{2, b}

¹School of Engineering Sciences and Technology, University of Hyderabad, Gachibowli,
Hyderabad – 500 046, India

²Centre for Nanotechnology, University of Hyderabad, Gachibowli, Hyderabad – 500 046, India

^asripathi1@yahoo.com, ^bananthaster@gmail.com

Keywords: Structural superplasticity, strain rate sensitivity, universal superplasticity curve, activation energy, optimal strain rate, viscosity.

Abstract: The equation $\sigma = K\dot{\epsilon}^m$, where σ is the applied stress, $\dot{\epsilon}$ is the strain rate, K and m are material constants that depend on stress / strain rate, temperature and grain size is often used to describe structural superplasticity. The general shape of the $\log \sigma - \log \dot{\epsilon}$ curve is sigmoidal. Based on limited data, it was suggested by us earlier that a universal $\sigma - \dot{\epsilon}$ curve could exist in a properly normalized space. $\dot{\epsilon}$ and m are normalized with respect to $\dot{\epsilon}_{opt}$ and m_{max} , the strain rate at which m is a maximum and the maximum m value respectively. Here a multi-dimensional relationship involving $\sigma / \sigma_{opt} - \dot{\epsilon} / \dot{\epsilon}_{opt} - m / m_{max} - \Delta F_o / kT - \eta / \eta_{opt}$ is developed; σ_{opt} corresponds to $\dot{\epsilon}_{opt}$, ΔF_o is the free energy of activation for the rate controlling mechanism, k the Boltzmann constant, T the absolute test temperature, η the (apparent) viscosity of the superplastic alloy and η_{opt} is the viscosity of the same alloy for $m=1$ in a dimensionless $\sigma - \dot{\epsilon}$ space. Using data concerning many systems, the phenomenology of structural superplasticity in all classes of materials is shown to be unique.

Introduction

Structural superplasticity, observed usually in micron- and sub-micron grained materials at high homologous temperatures ($T \geq 0.4 T_m$, where T is the experimental temperature and T_m is the absolute melting temperature of the material being tested) is a strain-rate sensitive phenomenon. Mathematically, it is often represented as $\sigma = K\dot{\epsilon}^m$, where σ is the externally applied stress, $\dot{\epsilon}$ the corresponding strain rate, m the strain rate sensitivity index (>0.3 for superplastic flow under uniaxial stressing) and K is a grain size-, temperature- and material-dependent parameter [1, 2]. Experimentation over a wide range has revealed that the $\ln \sigma - \ln \dot{\epsilon}$ curve has a sigmoidal shape; hence a maximum appears in the $m - \ln \dot{\epsilon}$ curve at an intermediate strain rate, which is the strain-rate up to which optimal superplasticity is observed [2]. Using limited experimental data, universality in the normalized values of m in isothermal superplasticity was proposed earlier [2]. The influence of T on universal superplastic behavior is examined here.

A mesoscopic grain boundary sliding controlled flow model for optimal superplastic deformation was presented [3-5]. This was verified in several systems and recently a standardized procedure for experimental validation involving the use of a numerical solution has been outlined [6]. It is well understood that the rheological response of superplastic alloys in the optimal range is visco-plastic, with viscosity decreasing with increasing strain rate (non-Newtonian) [1, 7]. As the physical mechanism controlling the rate of superplastic flow is regarded to be the same for different classes of materials like metals and alloys, ceramics, metal- and ceramic- based composites, intermetallics, nanostructured materials, bulk metallic glasses etc., a case could be advanced that the phenomenology of this process also is universal. In this paper this hypothesis is tested.

Analytical Procedure

It was pointed out earlier that a universal curve could exist when the values of the strain rate sensitivity index are normalized with respect to the optimal value of the strain rate sensitivity index and plotted against a normalized strain rate [2]. But, m depends on the temperature of deformation as well and here the effect of the homologous temperature on this universal curve is also examined. Bringing temperature of deformation into the analysis allows one to determine in addition the free energy of activation (ΔF_0), and the apparent viscosity (η), which varies with both strain rate ($\dot{\epsilon}$) and temperature (T). Evidently when ΔF_0 is normalized with respect to (kT), where k is the Boltzmann constant, such values for all superplastic systems should fall within a narrow band. As for the values of the apparent viscosity of materials, in this paper, it is normalized as a function of the viscosity in the strain rate – normalized stress space at which $m = 1.0$ [8] and plotted against the normalized strain rate ($\dot{\epsilon}/\dot{\epsilon}_{opt}$). In fact, this should be a three dimensional plot, with the homologous temperature (T/T_m) being plotted along the third axis. Work with regard to this extension is in progress.

Experimental results published by [9-19] are used here.

Results and Discussions

Strain rate sensitivity index: Experimental results reported in [9–13] were analyzed and the melting temperature was obtained from [20]. Fig. 1 shows the universal superplastic curve, which has a quadratic shape, and in Table 1, the coefficient of correlation for a second degree fit for each homologous temperature is presented. It is noted that in Fig. 1 the approximate curves drawn do demonstrate a “band” which is dependent on temperature. And most of the data points fall within the band.

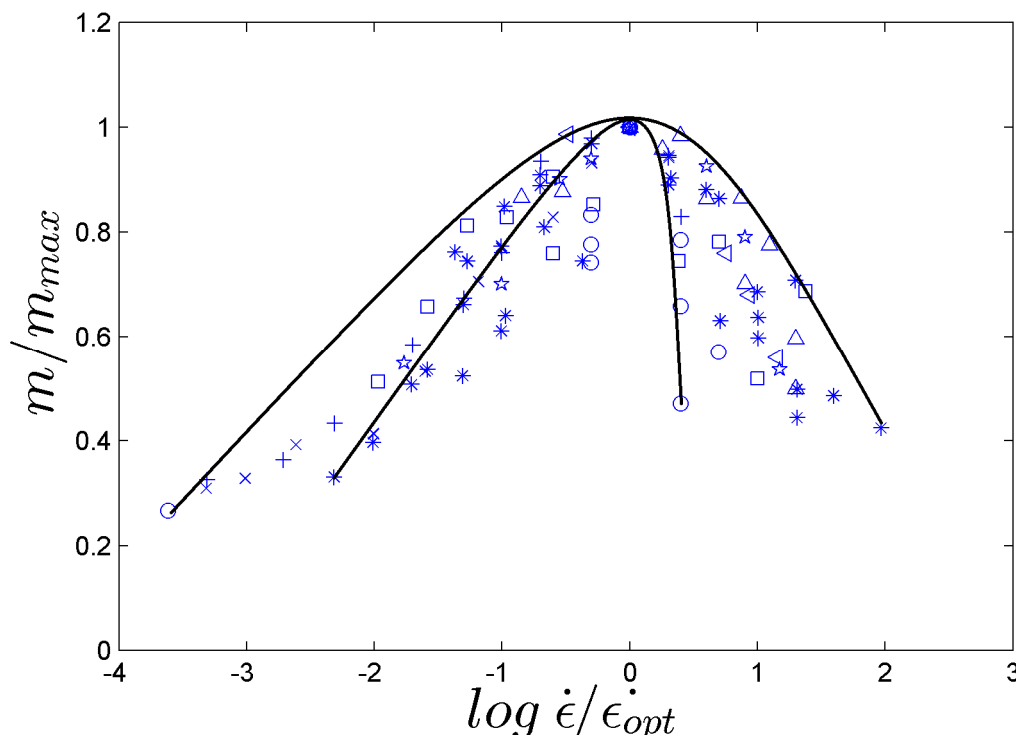


Figure 1: Universal superplastic curve

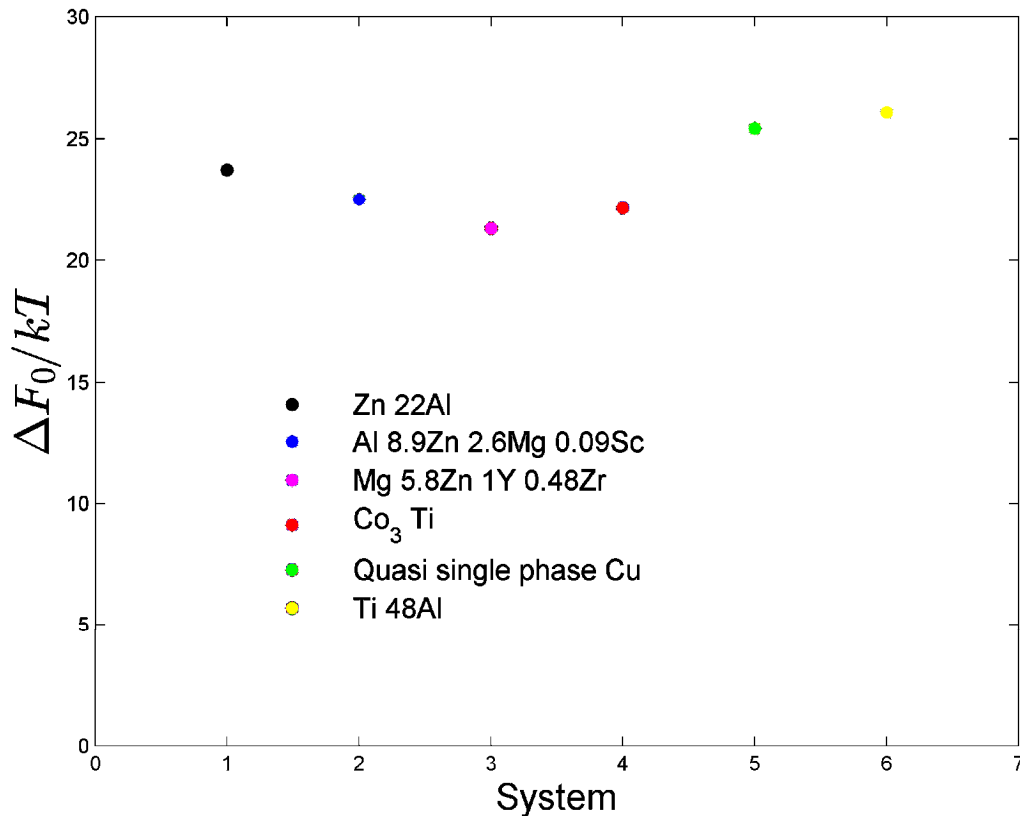
Table 1: Coefficient of correlation for the systems in Fig. 1

Sl. No	System composition	Homologous Temperature	Coefficient of correlation
1	Al 5.7Mg 0.32Sc 0.3Mn	0.56	0.98
2	Fe 0.168C 1.361 Mn 0.453 Si	0.59	0.61
3	Al 5.7Mg 0.32Sc 0.3Mn	0.61	0.95
4	Al 5.7Mg 0.32Sc 0.3Mn	0.67	0.88
5	Al 5.7Mg 0.32Sc 0.3Mn	0.72	0.96
6	Al 33Cu	0.74	0.90
7	Al 6Mg 0.3Sc	0.77	0.93
8	Al 6Mg 0.3Sc	0.80	0.66
9	Al 6Mg 0.3Sc	0.82	0.91

Coefficient of correlation is calculated as:
$$\frac{\sum XY - \sum X \sum Y}{\left(n \sum X^2 - (\sum X)^2 \right)^{0.5} \left(n \sum Y^2 - (\sum Y)^2 \right)^{0.5}};$$

where $X = \dot{\epsilon} / \dot{\epsilon}_{opt}$ and $Y = m / m_{max}$

Free energy of activation: Fig. 2 presents the values of the free energies of activation for the experimental data taken from [14–19], normalized with respect to the temperature of deformation, i.e., the $(\Delta F_0/kT)$ values are plotted for the different systems. It is seen that the normalized activation energy for the metallic systems studied fall within a narrow band. But, the absolute value of the normalized activation energy was different for ceramics. A study is presently underway to check if the normalized free energy of activation is different for different classes of materials or if a better unification that would be applicable to all classes of materials can be achieved.

**Figure 2:** Normalized free energy of activation

Viscosity: Systems [14-19] were chosen for the viscosity analysis. The procedure to obtain the viscosity, η_{opt} , at which in a normalized stress – strain rate space $m = 1.0$ is explained in [8]. Fig. 3 shows the results. It is seen that systems of different compositions deforming at widely different temperatures exhibit a very similar viscosity variation in the dimensionless viscosity – normalized strain rate space.

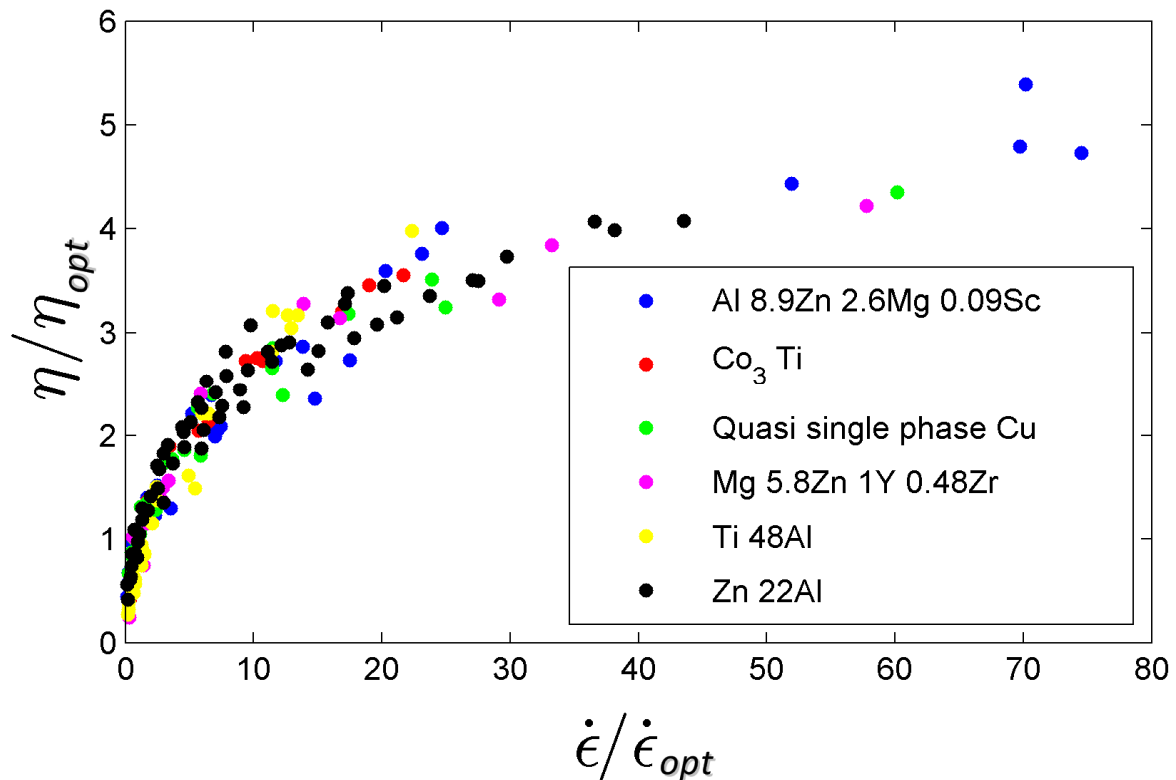


Figure 3: Viscosity versus strain rate

Conclusions

From a physical standpoint, the mesoscopic grain boundary sliding model, suggested a while ago as controlling the rate of superplastic flow, has been validated for many alloys and classes of materials [4, 21]. Here it is shown that phenomenologically the strain rate sensitivity index, free energy of activation and viscosity display a universal behavior in respective normalized spaces. This understanding should lead to an efficient design of new superplastic alloys that can be formed at convenient temperatures. Practical examples are presently being worked out.

References

- [1] K.A. Padmanabhan, G.J. Davies, Superplasticity: mechanical and structural aspects, environmental effects, fundamentals and applications. Springer-Verlag; 1980. Reference to a chapter in an edited book:
- [2] K.A. Padmanabhan, R.A. Vasin, F.U. Enikeev, Superplastic Flow: Phenomenology and Mechanics, Springer; 2001.
- [3] K.A. Padmanabhan, J. Schlipf, Model for grain boundary sliding and its relevance to optimal structural superplasticity Part 1 – Theory, Mater. Sci. Technol. 12 (1996) 391–9.
- [4] K.A. Padmanabhan, Grain boundary sliding controlled flow and its relevance to superplasticity in metals, alloys, ceramics and intermetallics and strain-rate dependent flow in nanostructured materials, J. Mater. Sci. 44 (2009) 2226–2238.

- [5] K.A. Padmanabhan, H. Gleiter, A mechanism for the deformation of disordered states of matter, *Curr. Opin. Solid State Mater. Sci.* 16 (2012) 243–253.
- [6] S. Sripathi, K.A. Padmanabhan, On the experimental validation of a mesoscopic grain boundary sliding-controlled flow model for structural superplasticity, *J. Mater. Sci.* 49 (2014) 199–210.
- [7] Y. Kawamura, T. Nakamura, A. Inoue, T. Masumoto, High-strain rate superplasticity due to newtonian viscous flow in $\text{La}_{55}\text{Al}_{25}\text{Ni}_{20}$ Metallic Glass, *Mater. Trans. JIM* 40 (1999) 794–803.
- [8] K.A. Padmanabhan, A theory of structural superplasticity, *Mater. Sci. Eng.* 29 (1977) 1–18.
- [9] A. Smolej, B. Skaza, M. Fazarinc, Determination of the strain-rate sensitivity and the activation energy of deformation in the superplastic aluminium alloy, *RMZ – Materials and Geoenvironment*, 56 (2009) 389–399.
- [10] F. Musin, R. Kaibyshev, Y. Motohashi, G. Itoh, High strain rate superplasticity in a commercial Al–Mg–Sc alloy, *Scr. Mater.* 50 (2004) 511–516.
- [11] T.G. Nieh, L.M. Hsiung, J. Wadsworth, R. Kaibyshev, High strain rate superplasticity in a continuously recrystallized Al–6%Mg–0.3%Sc alloy, *Acta. Mater.* 46 (1998) 2789–800.
- [12] S. Fernandez, M.J.Q. Hernández, J.O. García, L.F.V. González, R. González, J.V. González, Superplasticity of ultrafine grained low-alloy steels, *Mem. Trab. Difus. Científica. Téc.* 10 (2012) 45–56.
- [13] K.A. Padmanabhan, G.J. Davies, Numerical analysis of superplasticity data for use in metal forming applications, *J. Mech. Phys. Solids.* 18 (1970) 261–275.
- [14] N. Kumar, K.S. Raman, D.H. Sastry, E.A. Little, Investigation of superplasticity by the impression creep technique, *J. Mater. Sci.* 25 (1990) 753–755.
- [15] I. Charit, R.S. Mishra, Low temperature superplasticity in a friction-stir-processed ultrafine grained Al–Zn–Mg–Sc alloy, *Acta. Mater.* 53 (2005) 4211–4223.
- [16] S.A. Shei, T.G. Langdon, The mechanical properties of a superplastic quasi-single phase copper alloy, *Acta. Metall.* 26 (1978) 639–646.
- [17] H. Yan, R. Chen, E. Han, Superplasticity of Mg-5.8Zn-1Y-Zr alloy sheet fabricated by combination of extrusion and hot-rolling processes, *Sci. China Ser. E Technol. Sci.* 52 (2009) 166–171.
- [18] W.Y. Kim, S. Hanada, T. Takasugi, Flow behavior and microstructure of Co_3Ti intermetallic alloy during superplastic deformation, *Acta. Mater.* 46 (1998) 3593–3604.
- [19] T.G. Nieh, J. Wadsworth, Microstructural characteristics and deformation properties in superplastic intermetallics, *Mater. Sci. Eng. A* 239–240 (1997) 88–96.
- [20] H.J. Frost, M.F. Ashby, *Deformation-mechanism maps: the plasticity and creep of metals and ceramics*, Pergamon Press, 1982.
- [21] K.A. Padmanabhan, H. Gleiter, Optimal structural superplasticity in metals and ceramics of microcrystalline- and nanocrystalline-grain sizes, *Mater. Sci. Eng. A* 381 (2004) 28–38.



Grain size softening effect in intermetallics



M. Raviathul Basariya^a, N.K. Mukhopadhyay^a, Sriharsha Sripathi^b, K.A. Padmanabhan^{c,*}

^a Department of Metallurgical Engineering, Indian Institute of Technology, Banaras Hindu University, Varanasi, 221 005, India

^b School of Engineering Sciences and Technology, University of Hyderabad, Prof. C.R. Rao Road, Hyderabad, 500 046, India

^c Centre for Nanotechnology, University of Hyderabad, Prof. C.R. Rao Road, Hyderabad, 500 046, India

ARTICLE INFO

Article history:

Received 16 December 2015

Received in revised form

23 February 2016

Accepted 29 February 2016

Available online 2 March 2016

Keywords:

Intermetallics

Nanostructured materials

Grain boundaries

Mechanical properties

ABSTRACT

Inverse Hall–Petch/grain size softening effect is a phenomenon, which when present, leads to a decrease in flow stress with a decrease in grain size. The manifestation of this phenomenon at room temperature in nanostructured intermetallics, including some of our new results, is discussed here. Following earlier work, the IHP effect is attributed to the loss of intra-crystalline dislocation motion control to mesoscopic (\geq a grain diameter) grain/interphase boundary sliding controlled flow, which evidently is confined to the grain/interphase boundary regions. Equations for estimating the free energy of activation (same as the activation energy) for the rate controlling process, the free volume fraction present in a basic sliding unit and the average number of grain boundaries that align to form a plane interface during superplastic deformation, derived in earlier papers, are used to account for this phenomenon quantitatively in the present case also.

© 2016 Elsevier B.V. All rights reserved.

1. Introduction

Nanocrystalline intermetallics are produced by different techniques [1–6]. The observed transition in material response from hardening to softening with decreasing grain size in the nanometer range (the so called “inverse Hall–Petch (IHP)” or “grain size softening effect”) in this class of materials at room temperature is an interesting phenomenon and appears to be independent of the processing route so long as contamination and significant changes in density due to processing are not present. In this paper, we have examined the phenomenon of inverse Hall–Petch effect at room temperature in some nanostructured intermetallics. Here, in view of the ambient temperature employed, grain size stability in the nanostructured intermetallics, after processing, is assured. In addition, so far as we could see, contamination and related issues were absent. Therefore, to the best of our judgment, the inverse Hall–Petch relationship observed in this class of materials is genuine. In our earlier works [7–13], optimal structural superplasticity was attributed to the onset of a mesoscopic (\sim a grain diameter or more) grain/interphase (in duplex or multi-phase materials) boundary sliding flow process. The usefulness of this

model was demonstrated earlier [8,10] for explaining the IHP effect in some metallic and nanostructured, quasi-crystalline materials. As stated above, the same model is used here to explain the IHP effect in intermetallics. While doing this, those aspects of the model, so far not emphasized, will be brought into focus. In addition, some new results on IHP in a nanocrystalline intermetallic, Al_5Fe_2 , obtained by us (unpublished) will be presented and shown to obey the same relationship. A full account of the mesoscopic grain boundary sliding controlled flow process and the validation procedures used are presented elsewhere [7–9,12,13]. For completeness, in the next section, a brief description of the mesoscopic grain/interphase boundary sliding controlled flow process is presented.

2. A brief description of a mesoscopic grain boundary sliding controlled flow model

It is well known that when deformation mechanisms operate in sequence, the slowest process will control the strain rate of deformation. In a coupled process like grain boundary sliding (GBS) – GB diffusion, which one of the two processes is regarded as rate controlling is a matter of choice on the part of the author [14,15]. The final aim is/should be to account for the experimental observations in as many systems as possible with the same minimum set of assumptions. In our model, it is assumed that during optimal superplastic flow, GBS, accompanied by diffusion in and/or

* Corresponding author.

E-mail addresses: kapse@uohyd.ernet.in, ananthaster@gmail.com (K.A. Padmanabhan).

dislocation emission from the sliding grain/interphase boundaries develops to a mesoscopic scale. (The grain interior is considered to be quasi-rigid, with practically no deformation present in this region, except for what is needed in the grain boundary neighborhoods, to ensure coherency of deformation). The former (GBS) is assumed to be the slower and hence the rate controlling process. The actual accommodation process (diffusion in, dislocation or partial dislocation emission from the sliding grain boundary regions) will depend on the nature and strength of the obstacles present in the grain boundaries and the experimental conditions like strain rate, grain size and temperature.

Several experiments have demonstrated that high-angle grain boundaries are very conducive to superplastic flow (for a summary, see Refs. [16,17]). With increasing strain, low-angle boundaries favorably oriented to the stress axis, will gradually be transformed into high-angle grain boundaries. Those that are unfavorably oriented will be bypassed by grain rotation, arising from the unbalanced shear stresses at the grain boundaries which slide at different rates that depend on the resolved shear stresses acting on these boundaries [18]. In other words, in this model superplastic deformation is rate controlled by mesoscopic grain/interphase boundary sliding along high-angle grain boundaries that are favorably oriented to the stress axis. The repeated observation that superplastic tendency is far less in materials with microstructures in which high-angle grain boundary fraction is rather low [19] vindicates this viewpoint. After a detailed survey of literature [13,20] it has also been concluded that solitons like vacancies, dislocations etc. get delocalized in high-angle boundaries and, therefore, it is not necessary –in fact, not meaningful– to invoke dislocation glide (based on crystallographic notions) along high-angle grain boundaries as a concomitant of the GBS process.

In this model, GBS is analyzed as a two-scale process: (a) atomistic, and (b) mesoscopic.

For mathematical development at the level of atomistics, the basic sliding unit present in the boundary is assumed to be an oblate spheroid of about 5 atomic diameters in the boundary plane and 2.5 atomic diameters in height (\approx average grain boundary width, see below) in a direction perpendicular to the boundary plane [7,9]. This way, it has been possible to explain superplastic flow in crystalline materials as well as bulk metallic glasses on a common basis [11]. This atomic ensemble is located symmetrically about the plane of the boundary with one half falling in each of the two grains that meet to form the boundary (Fig. 1 (a), (b)). The choice of shape (oblate spheroid) is due to the fact that the strain field inside a deformed oblate spheroid is uniform, with the help of which many useful engineering properties can be determined [21]. As has been pointed out, any deviation present in the real shape of the atom ensemble from the idealized (oblate spheroid) shape is taken care of by a form factor, α , which has a magnitude, ~ 1.0 [7]. The average shear strain associated with a unit sliding event (Fig. 1 (c) – (e)) is ~ 0.1 (arrived at based on bubble raft experiments and molecular dynamics simulations [22–25]), when the ensemble moves from one stable/metastable position to the next. It must be noted, however, that the actual shear strain associated with a unit boundary sliding event will be a function of the nature and strength of the interatomic forces present among the atoms that constitute the boundary. However, the bubble raft experiments reveal the order of magnitude value that could be associated with the unit shear strain (~ 0.1). (An examination of Fig. 1 (d), (e) reveals that after unit sliding shear strain, a circular dislocation loop (in the Volterra sense) of Burgers vector zero, will be left on the grain boundary plane, although crystallographic notions cannot be associated with such a deformation process (as the atom shuffling will involve only a very small fraction of the inter-atomic distance). Thus, a formal (not physical) case can be made for the propagation

of extrinsic dislocations along the boundary during the sliding process to reconcile this approach with that of Rybin, Nazarov and Valiev (for a summary, see Ref. [26]).

Based on an extensive analysis of experimental data concerning many metals, the grain boundary width is assumed to be 2–3 atomic diameters [25]. The elastic energy of the shear and momentary volumetric distortions (as the basic sliding unit is embedded inside a solid matrix) accompanying the unit shear event, ΔF_0 , constitutes the free energy of activation for the GBS process (arrived at by considering the deforming unit and the surroundings as a whole; same as the activation energy for the rate controlling process, often discussed in the literature, which only looks at the deforming unit [12]). Sliding at an individual grain/interphase boundary described above is rendered ineffective by steric hindrance, e.g. the presence of a triple junction.

For large scale sliding, the process has to develop to a mesoscopic scale (Fig. 2(a)) and form a plane interface (Fig. 2 (b)). When such plane interface formation is present simultaneously at different locations in a test specimen, inter-connection of such plane interfaces will result in large-scale boundary sliding and significant specimen elongation, i.e., superplasticity is observed. The length of the plane interfaces so formed is likely to be a strong function of grain size and temperature. It (the length of the plane interface) can be of the order of one or more grain diameters. (See later for a mathematical expression.)

During mesoscopic plane interface formation a portion of the energy supplied by the applied stress is spent in rearranging matter in the grain boundary region (Fig. 2 (b)). This gives rise to a long-range threshold stress, τ_0 , needed for the onset of mesoscopic boundary sliding. The driving force for plane interface formation is the minimization of the total free energy of the deforming system and the fact that for this configuration the work done by the external stress is a maximum, as required by Taylor's principle of maximum work [7,13]. (In Fig. 2 (c) it is very easy to show using Herring's equation for equilibrium at a triple junction that extending the boundary and increasing the magnitude of the included angle at the triple junction leads to a lowering of the total free energy of the system [9]). The long-range threshold stress necessary for plane interface formation is calculated assuming the grain shape to be rhombic dodecahedron (Fig. 2 (a)), the shape considered to be the closest to real crystals in polycrystalline materials [7,8]. As the grain boundary area per unit volume increases with a decrease in grain size, τ_0 increases with decreasing grain size (the number of boundaries aligning to form a plane interface increases with decreasing grain size). In contrast, as the inter-atomic bonds become weaker with increasing temperature, the rearrangement of matter in the boundary regions becomes easier and τ_0 decreases with increasing temperature. Experimental support for these two inferences is available [16,17].

A survey of literature reveals that this model has received considerable positive attention in the literature dealing with the deformation of nanocrystalline materials. This is because, in view of the very fine grain size, the grain boundary regions constitute a very significant fraction of the total volume of a material and thus, the idea of viewing the grain interior as a strong phase A and the grain boundary region as a weaker phase B is very much in vogue. Recently, the significance of this idea has been recognized beyond the domain of nanostructured materials. For example [27], have observed grain boundary sliding at room temperature in severe plastic deformed aluminum. They have suggested that the grain boundary region constitutes a weaker, high wetting component (component B) between high strength Al–Al grains (component A). In other words, the presence of thin GB layers is considered to serve as an inter-granular lubricant. Such GB layers can also form due to the so-called pseudo-incomplete GB wetting (see, for example [28],

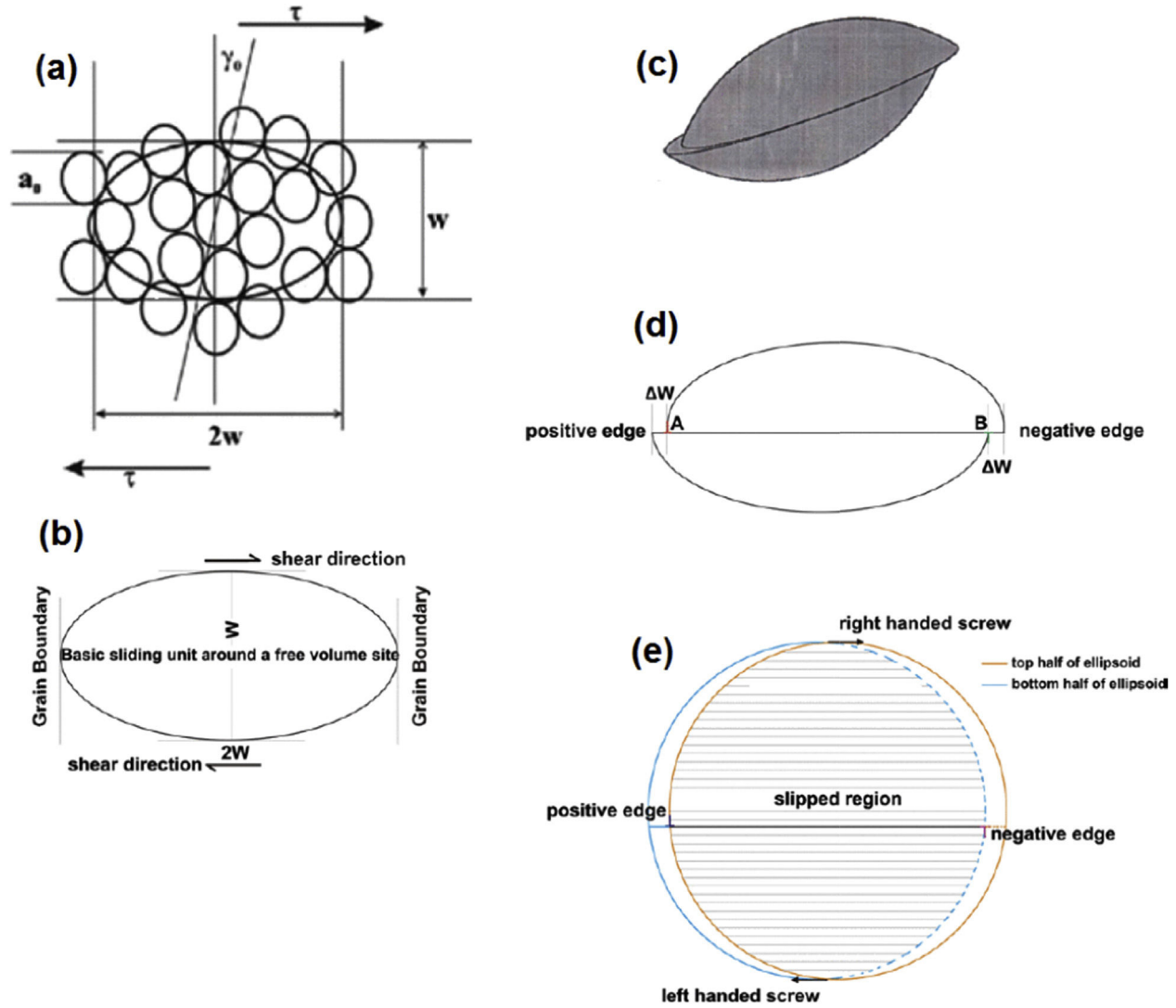


Fig. 1. (a) Basic boundary sliding unit, (b) elevation view of undeformed basic sliding unit, (c) isometric view of the deformed basic sliding unit, (d) elevation view of the deformed basic sliding unit, (e) plan view of the deformed basic sliding unit.

and references cited therein) and facilitate grain boundary deformation processes at ambient temperatures. It is, therefore, heartening to see that the general relevance of our ideas is getting appreciated across domains now.

Such a description leads to Eq. (1) and Eq. (2) [7,9].

$$\dot{\gamma} = \frac{2W\gamma_0\nu}{L} \sin h\left(\frac{(\tau - \tau_0)\gamma_0 V_0}{2kT}\right) \exp\left(-\frac{\Delta F_0}{kT}\right) \quad (1)$$

where $\dot{\gamma}$ is the shear strain rate, L the average grain size, γ_0 the mean shear strain associated with a unit-sliding event, ΔF_0 is the free energy of activation for the rate controlling process (same as the activation energy), V_0 the volume of the basic sliding unit, which, for an oblate spheroid, is given by $V_0 = (2/3)\pi W^3$, with W the grain boundary width ($\sim 2.5 a_0$), where a_0 is the atomic diameter [21], ν the thermal vibration frequency (10^{13} s^{-1} or $(kT/h) \text{ s}^{-1}$, with h Planck's constant), k the Boltzmann constant, T the absolute temperature of deformation, τ the applied shear stress and τ_0 is the long-range threshold shear stress necessary to be overcome for the onset of mesoscopic boundary sliding. And

$$\Delta F_0 = \frac{1}{2} (\beta_1 \gamma_0^2 + \beta_2 \varepsilon_0^2) G V_0 \quad (2)$$

with G the shear modulus, and, as shown by Eshelby [21], for the oblate spheroid shape $\beta_1 = 0.944(1.590 - p)/(1 - p)$ and $\beta_2 = 4(1 + p)/9(1 - p)$, where p is the Poisson ratio. It is recalled that in isotropic materials, e.g. texture-free nanostructured materials, the hardness is approximately equal to three times the uniaxial tensile or compressive yield stress. For the isothermal case, assuming von Mises criterion, Eq. (1) can be rewritten as [8,9],

$$H_V = H_{V_0} - \frac{m_2}{L} (L - L_0)^{0.5} \quad (3)$$

where H_V is the measured steady state hardness value, H_{V_0} is the instantaneous hardness recorded on load application and L_0 is the limiting small grain size at which τ_0 will be equal to zero ($= 2\sqrt{6} W$) [8,9,24]. m_2 and L_1 are constants, defined as:

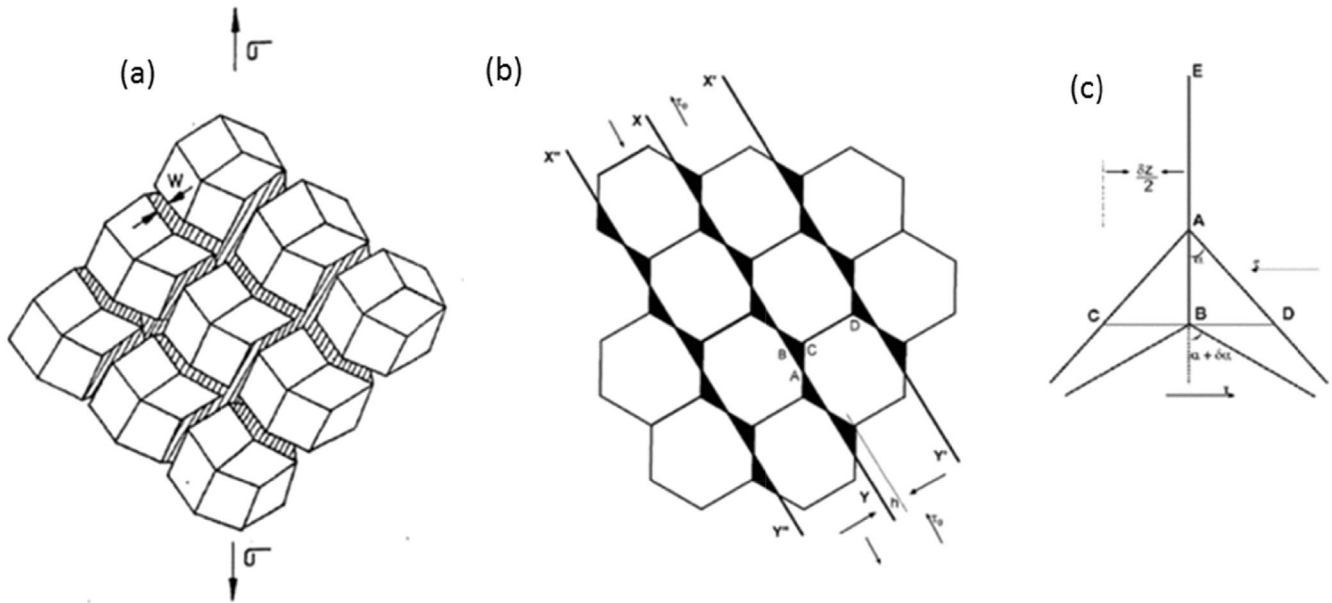


Fig. 2. (a) Shaded grain boundaries of rhombic dodecahedral grains within which the rate controlling deformation process is confined, (b) planar interfaces resulting from mesoscopic boundary sliding (XY, X'Y', X''Y'' etc.) in 2D sections of aggregate of grains of equal size and rhombic dodecahedral shape. When atoms located in the shaded regions are moved by a shear stress parallel to the sliding boundaries to extend the boundary perpendicular to the shear stress direction to reach the sliding interface, a plane interface results. (c) Shear-stress driven movement of a boundary triple junction to lower the overall free energy of the system.

$$m_2 = \frac{GL_1^{0.5}}{C} \quad L_1 = 2^{1.5} 3^{-0.75} N^{-0.5} \frac{\gamma_B}{G\alpha_f}$$

where C is a conversion factor (for conversion from shear stress to hardness; it is $3\sqrt{3}$ for the von Mises criterion), α_f a form factor of the order of unity (to account for the real shape of the basic sliding unit, which could be different from that of an oblate spheroid), γ_B the specific grain-boundary energy, which for a nanostructured material is $\approx 1 \text{ J}\cdot\text{m}^{-2}$ [29] and N is the number of grain boundaries that align to form a plane interface.

From Eq. (3) it follows that m_2 is the slope of the hardness versus $[(L-L_0)^{0.5}/L]$ plot. Therefore, using experimental hardness - grain size data, L_1 and N could be computed.

The threshold stress, in turn, is calculated as [8,9]:

$$\tau_0 = G \left[\frac{L_1}{L} \left(1 - \frac{L_0}{L} \right) \right]^{0.5}, \quad L \geq L_0 \quad (4)$$

Using this value of τ_0 , the free energy of activation, ΔF_0 , in Eq. (1) is calculated. It has also been shown further [9] that

$$\tau_0 = \left(\frac{2^{1.5} \gamma_B}{30.75} \right)^{0.5} \frac{(L - L_0)^{0.5}}{LN^{0.25}} \quad (5)$$

3. Results and discussion

The first two authors of the present paper have recently observed IHP in the intermetallic Al_5Fe_2 (unpublished). Earlier, IHP was reported in other intermetallics like TiAl [30], NiAl_3 [31] and NbAl_3 [32]. The experimental data presented in these papers were analyzed using the models of Conrad and Narayan [33] (who have also presented a model for explaining this phenomenon) and the present authors.

The coefficient of correlation for all the three expressions H_v vs.

$\ln(L)$, H_v vs. L (these two dependences correspond to the rigorous and the approximate forms of the relationship due to Conrad and Narayan [33]) and H_v vs. $(L-L_0)^{0.5}/L$ (our model) is very similar and the findings are presented in Table 1. On this basis, both the models are acceptable.

A major limitation of the former analysis [33] is that the effective stress is taken as the applied stress, i.e., the strain-rate sensitivity index, $m = 1.0$. However, in nanocrystalline intermetallics at room temperature the values of m are in the range 0.02–0.08 [34,35]. Other limitations of that model have already been pointed out in Ref. [10].

Using our approach, in addition to the prediction that H_v vs. $[(L-L_0)^{0.5}/L]$ is a straight line (validated in Table 1), further insights into the deformation process could be obtained. The experimental data analyzed here were generated either using a micro- or a nano-indenter. Following earlier authors [36], the strain rate in the hardness tests is assumed to be in the range of $5 \times 10^{-2} \text{ s}^{-1}$ – $5 \times 10^{-4} \text{ s}^{-1}$. While the shear modulus value for Al_5Fe_2 is available from our experiments, for the other systems the values were taken from the NIMS (National Institute for Materials Science, Tsukuba, Japan) database. Using Eq. (1) and Eq. (2) and assuming von Mises criterion, the free energy of activation, ΔF_0 , for the rate controlling process and the accurate values of γ_0 (which depends on the nature and strength of inter-atomic bonds present in a material and the boundary misorientation) were determined for the four systems as a function of the two strain rates, following the numerical procedure explained in Ref. [12]. The results are

Table 1
Degree of fit for the three relations: $H_v \alpha \ln(L)$, $H_v \alpha L$ and $H_v \alpha (L-L_0)^{0.5}/L$.

System	Correlation coefficient of H vs		
	$\ln(L)$	L	$(L-L_0)^{0.5}/L$
TiAl [30]	0.995	0.987	0.994
NiAl ₃ [31]	0.992	0.990	0.988
NbAl ₃ [32]	0.905	0.876	0.911
Al_5Fe_2 (unpublished)	0.970	0.949	0.968

Table 2

Average shear strain in the basic unit of sliding, the number of grain boundaries that align to form a plane interface during mesoscopic boundary sliding and the free energy of activation for the rate controlling GBS process.

System	N	L, nm	τ_0 , GPa	γ_0 , Refined	ΔF_0 kJ.mol ⁻¹	
					$\dot{\gamma} = 5 \times 10^{-2} \text{ s}^{-1}$	$\dot{\gamma} = 5 \times 10^{-4} \text{ s}^{-1}$
TiAl [30]	0.0757	21.4	3.62	0.0698	201.72	214.36
		18.7	3.82			
		17.1	3.94			
		12.5	4.38			
		12.1	4.42			
NiAl ₃ [31]	0.0154	11.0	4.55	0.0925	145.66	158.30
		60.8	2.81			
		53.0	2.99			
		49.4	3.09			
		45.0	3.23			
		42.0	3.34			
NbAl ₃ [32]	0.0018	25.6	4.17	0.1475	185.00	197.64
		34.0	3.42			
		30.4	3.59			
		27.0	3.79			
		25.4	3.88			
		22.0	4.12			
Al ₅ Fe ₂ (unpublished)	0.8458	32.0	1.52	0.0711	157.73	170.37
		23.6	1.74			
		11.0	2.27			
		10.0	2.33			

G for: TiAl = 75 GPa, NiAl₃ = 50.62 GPa, NbAl₃ = 15.41 GPa, Al₅Fe₂ = 61.8 GPa.

*As the strain rates in the indentation tests are in the range of $5 \times 10^{-2} \text{ s}^{-1}$ – $5 \times 10^{-4} \text{ s}^{-1}$ [36], γ_0 values were obtained for the mean values of ΔF_0 at the two extreme strain rates. Bubble raft experiments reveal that $\gamma_0 \sim 0.10$. Its accurate values were determined using the method of [12].

presented in Table 2. The fit is very satisfactory. Therefore, it could be concluded that the observed IHP effect in intermetallics is understandable in terms of the mesoscopic boundary sliding controlled flow process.

With the help of Table 2 some features of the model, so far not discussed, are brought into focus. While optimal structural superplasticity in intermetallics was accounted for in terms of the mesoscopic boundary sliding controlled flow model in an earlier paper [12], this is the first time that this model has been used to explain inverse Hall–Petch effect in nanocrystalline intermetallics in a systematic manner. So far as the latter (IHP) phenomenon is concerned, the relevance of the model has been tested on four grounds: (a) a good fit for the prediction that H_v versus $((L-L_0)^{0.5}/L)$ is linear (Table 1; experimental correlation is also good). (b) The value of N in Eq. (5). If it is greater than 1.0, the accommodation during plane interface formation is predominantly by diffusion. If it is equal to or less than 1.0, it is mostly by dislocation/partial dislocation emission from the sliding boundaries. The values of N for all the systems analyzed here is less than one. It follows from the model [7,9,24] that plane interface formation in the grain size ranges present in the systems studied is accommodated by the (faster than GBS) emission of dislocations from the deforming boundaries, which then traverse the grain to get absorbed at the opposite boundaries [7,9]. The significant spread in the values of N (all below 1.0, but falling in the range 0.002–0.846) indicates the fraction of a boundary that is involved at a time to form a plane interface on a local scale. This would lead to a prediction that the misfit produced by a basic boundary sliding event in NbAl₃ will be greater than in Al₅Fe₂. There is scope for verifying this prediction in a future study involving the use of molecular dynamics simulations. (c) The value of γ_0 . The values of the unit shear strain associated with a basic sliding event in the four intermetallics analyzed here vary from 0.07 to 0.14. This implies that the mean value of 0.10 arrived at based on bubble raft experiments (which ignores the system-dependent strength and nature of the interatomic bonds in the boundary regions) is a realistic value for order of magnitude calculations. (d) Consistent with experimental results, the presence

of a long range threshold stress, needed for the onset of mesoscopic grain boundary sliding in the model ensures that the values of m in these alloys are well below unity. Based on these four criteria/tests, the usefulness of the model in explaining the inverse Hall–Petch effect in the presently analyzed nanocrystalline intermetallics is established. Finally, it could be said that at the present level of understanding explaining optimal superplasticity/IHP effect amounts to solving a two-constant problem, viz., ΔF_0 and τ_0 are obtained from experiments, c.f. the mathematical theory of elasticity, where the shear modulus and Poisson's ratio are obtained from experiments. However, in the present analysis, it is possible to predict these two constants of ΔF_0 and τ_0 ab initio and this aspect will be considered in a future publication.

Acknowledgment

NK Mukhopadhyay thanks the Indian National Academy of Engineering (INAE) for support under its Chair Professorship scheme.

References

- [1] H. Chang, C.J. Altstetter, R.S. Averback, Characteristics of nanophase TiAl produced by inert gas condensation, *J. Mater. Res.* 7 (1992) 2962–2970, <http://dx.doi.org/10.1557/JMR.1992.2962>.
- [2] C.C. Koch, Y.S. Cho, Nanocrystals by high energy ball milling, *Nanostruct. Mater.* 1 (1992) 207–212, [http://dx.doi.org/10.1016/0965-9773\(92\)90096-G](http://dx.doi.org/10.1016/0965-9773(92)90096-G).
- [3] T. Christman, M. Jain, Processing and consolidation of bulk nanocrystalline titanium–aluminide, *Scr. Metall. Mater.* 25 (1991) 767–772, [http://dx.doi.org/10.1016/0956-716X\(91\)90222-M](http://dx.doi.org/10.1016/0956-716X(91)90222-M).
- [4] G. Palumbo, U. Erb, K.T. Aust, Triple line disclination effects on the mechanical behaviour of materials, *Scr. Metall. Mater.* 24 (1990) 2347–2350, [http://dx.doi.org/10.1016/0956-716X\(90\)90091-T](http://dx.doi.org/10.1016/0956-716X(90)90091-T).
- [5] X.D. Liu, B.Z. Ding, Z.Q. Hu, K. Lu, Y.Z. Wang, Properties of nanocrystalline Fe–Cu–Si–B alloys generated by crystallization of the amorphous alloy, *Phys. B Condens. Matter* 192 (1993) 345–350, [http://dx.doi.org/10.1016/0921-4526\(93\)90009-U](http://dx.doi.org/10.1016/0921-4526(93)90009-U).
- [6] X.D. Liu, J.T. Wang, B.Z. Ding, Preparation and properties of nanocrystalline (Fe_{0.99}Mn_{0.01})₇₈Si₈B₁₃ alloys, *Scr. Metall. Mater.* 28 (1993) 59–64, [http://dx.doi.org/10.1016/0956-716X\(93\)90537-3](http://dx.doi.org/10.1016/0956-716X(93)90537-3).
- [7] K.A. Padmanabhan, J. Schlipf, Model for grain boundary sliding and its relevance to optimal structural superplasticity Part 1 – theory, *Mater. Sci. Technol.* 12 (1996) 391–399, <http://dx.doi.org/10.1179/026708396790165920>.

- [8] H. Hahn, K.A. Padmanabhan, A model for the deformation of nanocrystalline materials, *Philos. Mag. Part B* 76 (1997) 559–571, <http://dx.doi.org/10.1080/01418639708241122>.
- [9] K.A. Padmanabhan, H. Gleiter, Optimal structural superplasticity in metals and ceramics of microcrystalline- and nanocrystalline-grain sizes, *Mater. Sci. Eng. A* 381 (2004) 28–38, <http://dx.doi.org/10.1016/j.msea.2004.02.054>.
- [10] K.A. Padmanabhan, S. Sripathi, H. Hahn, H. Gleiter, Inverse Hall–Petch effect in quasi- and nanocrystalline materials, *Mater. Lett.* 133 (2014) 151–154.
- [11] J. Buenz, K.A. Padmanabhan, G. Wilde, On the applicability of a mesoscopic interface sliding controlled model for understanding superplastic flow in bulk metallic glasses, *Intermet* 60 (2015) 50–57, <http://dx.doi.org/10.1016/j.intermet.2015.01.007>.
- [12] S. Sripathi, K.A. Padmanabhan, On the experimental validation of a mesoscopic grain boundary sliding-controlled flow model for structural superplasticity, *J. Mater. Sci.* 49 (2014) 199–210, <http://dx.doi.org/10.1007/s10853-013-7693-y>.
- [13] K.A. Padmanabhan, H. Gleiter, A mechanism for the deformation of disordered states of matter, *Curr. Opin. Solid State Mater. Sci.* 16 (2012) 243–253, <http://dx.doi.org/10.1016/j.cossms.2012.05.001>.
- [14] M.V. Speight, Mass transfer and grain-boundary sliding in diffusion creep, *Acta Metall.* 23 (1975) 779–781, [http://dx.doi.org/10.1016/0001-6160\(75\)90060-7](http://dx.doi.org/10.1016/0001-6160(75)90060-7).
- [15] M.V. Speight, Reply to comments on grain-boundary sliding in diffusion creep, *Scr. Metall.* 10 (1976) 163, [http://dx.doi.org/10.1016/0036-9748\(76\)90141-1](http://dx.doi.org/10.1016/0036-9748(76)90141-1).
- [16] K.A. Padmanabhan, G.J. Davies, *Superplasticity: Mechanical and Structural Aspects, Environmental Effects, Fundamentals and Applications*, Springer-Verlag, 1980.
- [17] T.G. Nieh, J. Wadsworth, O.D. Sherby, *Superplasticity in Metals and Ceramics*, Cambridge University Press, 1997.
- [18] O. Engler, K.A. Padmanabhan, K. Lücke, A model for superplastic flow induced texture annihilation, *Model. Simul. Mater. Sci. Eng.* 8 (2000) 477, <http://dx.doi.org/10.1088/0965-0393/8/4/306>.
- [19] K.A. Padmanabhan, Grain boundary sliding controlled flow and its relevance to superplasticity in metals, alloys, ceramics and intermetallics and strain-rate dependent flow in nanostructured materials, *J. Mater. Sci.* 44 (2009) 2226–2238, <http://dx.doi.org/10.1007/s10853-008-3076-1>.
- [20] K.A. Padmanabhan, H. Gleiter, On the structure of grain/interphase boundaries and interfaces, *Beilstein J. Nanotechnol.* 5 (2014) 1603–1615, <http://dx.doi.org/10.3762/bjnano.5.172>.
- [21] J.D. Eshelby, The determination of the elastic field of an ellipsoidal inclusion, and related problems, *Proc. R. Soc. Lond. A* 241 (1957) 376–396, <http://dx.doi.org/10.1098/rspa.1957.0133>.
- [22] D. Wolf, Structure–energy correlation for grain boundaries in F.C.C. metal—III. Symmetrical tilt boundaries, *Acta Metall. Mater.* 38 (1990) 781–790, [http://dx.doi.org/10.1016/0956-7151\(90\)90030-K](http://dx.doi.org/10.1016/0956-7151(90)90030-K).
- [23] D. Wolf, Structure–energy correlation for grain boundaries in f.c.c. metals—IV. Asymmetrical twist (general) boundaries, *Acta Metall. Mater.* 38 (1990) 791–798, [http://dx.doi.org/10.1016/0956-7151\(90\)90031-B](http://dx.doi.org/10.1016/0956-7151(90)90031-B).
- [24] T.A. Venkatesh, S.S. Bhattacharya, K.A. Padmanabhan, J. Schlipf, Model for grain boundary sliding and its relevance to optimal structural superplasticity, *Mater. Sci. Technol.* 12 (1996) 635–643, <http://dx.doi.org/10.1179/026708396790122486>.
- [25] P. Haasen, *Physical Metallurgy*, Cambridge University Press, 1978.
- [26] A.A. Nazarov, Ensembles of gliding grain boundary dislocations in ultrafine grained materials produced by severe plastic deformation, *Scr. Mater.* 37 (1997) 1155–1161, [http://dx.doi.org/10.1016/S1359-6462\(97\)00230-3](http://dx.doi.org/10.1016/S1359-6462(97)00230-3).
- [27] R.Z. Valiev, M.Y. Murashkin, A. Kilmametov, B. Straumal, N.Q. Chinh, T.G. Langdon, Unusual super-ductility at room temperature in an ultrafine-grained aluminum alloy, *J. Mater. Sci.* 45 (2010) 4718–4724, <http://dx.doi.org/10.1007/s10853-010-4588-z>.
- [28] B.B. Straumal, I. Konyashin, B. Ries, A.B. Straumal, A.A. Mazilkin, K.I. Kolesnikova, et al., Pseudopartial wetting of WC/WC grain boundaries in cemented carbides, *Mater. Lett.* 147 (2015) 105–108, <http://dx.doi.org/10.1016/j.matlet.2015.02.029>.
- [29] D. Wolf, V. Yamakov, S.R. Phillpot, A. Mukherjee, H. Gleiter, Deformation of nanocrystalline materials by molecular-dynamics simulation: relationship to experiments? *Acta Mater.* 53 (2005) 1–40, <http://dx.doi.org/10.1016/j.actamat.2004.08.045>.
- [30] H. Chang, H.J. Höfler, C.J. Altstetter, R.S. Averback, Synthesis, processing and properties of nanophase TiAl, *Scr. Metall. Mater.* 25 (1991) 1161–1166, [http://dx.doi.org/10.1016/0956-716X\(91\)90521-2](http://dx.doi.org/10.1016/0956-716X(91)90521-2).
- [31] K. Okazaki, *Proc. Thermac'97*, 1997.
- [32] D.K. Kim, K. Okazaki, Nano-crystalline consolidation of MA powders by EDC, *Mater. Sci. Forum* 88–90 (1992) 553–560, <http://dx.doi.org/10.4028/www.scientific.net/MSF.88-90.553>.
- [33] H. Conrad, J. Narayan, On the grain size softening in nanocrystalline materials, *Scr. Mater.* 42 (2000) 1025–1030, [http://dx.doi.org/10.1016/S1359-6462\(00\)00320-1](http://dx.doi.org/10.1016/S1359-6462(00)00320-1).
- [34] K.A. Padmanabhan, Mechanical properties of nanostructured materials, *Mater. Sci. Eng. A* 304–306 (2001) 200–205, [http://dx.doi.org/10.1016/S0921-5093\(00\)01437-4](http://dx.doi.org/10.1016/S0921-5093(00)01437-4).
- [35] S. Varam, K.V. Rajulapati, K. BhanuSankaraRao, Strain rate sensitivity studies on bulk nanocrystalline aluminium by nanoindentation, *J. Alloy. Compd.* 585 (2014) 795–799, <http://dx.doi.org/10.1016/j.jallcom.2013.09.116>.
- [36] V. Maier, K. Durst, J. Mueller, B. Backes, H.W. Höppel, M. Göken, Nano-indentation strain-rate jump tests for determining the local strain-rate sensitivity in nanocrystalline Ni and ultrafine-grained Al, *J. Mater. Res.* 26 (2011) 1421–1430, <http://dx.doi.org/10.1557/jmr.2011.156>.



ELSEVIER

Contents lists available at ScienceDirect

Materials Letters

journal homepage: www.elsevier.com/locate/matlet

Inverse Hall–Petch effect in quasi- and nanocrystalline materials

K.A. Padmanabhan^{a,*}, Sriharsha Sripathi^a, H. Hahn^{b,c}, H. Gleiter^b^a School of Engineering Sciences and Technology & Centre for Nanotechnology, University of Hyderabad, Prof. C R Rao Road, Hyderabad 500 046, India^b Karlsruhe Institute of Technology (North Campus), Institute of Nanotechnology, Hermann-von-Helmholtz-Platz 1, 76344 Eggenstein-Leopoldshafen, Germany^c KIT-TUD Joint Research Laboratory Nanomaterials, TU Darmstadt, Jovanka-Bontschits-Strasse 2, 64287 Darmstadt, Germany

ARTICLE INFO

Article history:

Received 13 June 2014

Accepted 25 June 2014

Available online 8 July 2014

Keywords:

Grain size softening/inverse Hall–Petch effect

Grain boundary sliding

Rate controlling process

Quasi-crystals

Nanocrystalline materials

ABSTRACT

Inverse Hall–Petch effect/grain size softening in quasi- and nanocrystalline materials at ambient/low temperatures is attributed to mesoscopic (\sim a grain diameter or more) grain/interphase boundary sliding controlled flow. Equations for estimating the free energy of activation for the rate controlling process, the free volume fraction present in a basic sliding unit and the average number of grain boundaries that align to form a planar interface during superplastic deformation are given in some of our earlier papers. These predictions are verified here using experimental data pertaining to one quasi- and two nanocrystalline systems. The agreement between the predictions and the experimental observations is satisfactory.

© 2014 Elsevier B.V. All rights reserved.

1. Introduction

In micro-mechanics [1] decreasing grain size has a similar effect as increasing temperature so far as creep effects in a material are concerned. Therefore, it is understandable that creep/superplastic effects are seen at room temperature in a high-temperature-melting material like palladium when its micro-structure is nanocrystalline [2]. Koch and Narayan [3] found fault with most of the experimental results in which inverse Hall–Petch (IHP) effect was reported because they noted that the samples used were not defect-free. According to them [3] only four sets of data demonstrated a genuine grain size softening/IHP effect.

Recently, a grain softening effect in an Al–Cu–Fe based nano-/quasicrystalline material was reported [4]. The experimental results (Fig. 3 of [4]) seem to suggest that the grain size dependence of hardness in the region in which the grain softening effect is observed follows IHP relationship, as suggested earlier [5,6]. Notwithstanding this, the authors have interpreted their results in terms of a model [7,8] in which the hardness varies as $\log(L)$ or L , where L is the average grain size, depending on the approximation used.

The present authors [5,6] presented an explanation for the occurrence of IHP effect by refining a model for mesoscopic grain

boundary sliding (mGBS) controlled flow in microcrystalline materials [9] to include the nanocrystalline range as well. The correlation of the flow stress with superplastic strain rates and the method of knowing the atomistic constants, estimating the free energy of activation for the rate controlling process, the threshold stress for the onset of mGBS and the free volume fraction present in a basic unit of sliding were details presented in later works [10–15]. In fact, [7,8] appear to have used an earlier paper of ours [16] extensively, which, like [7,8], deals with grain boundary sliding (GBS) controlled flow. For example, Eq. (2) of [7] becomes identical to Eq. (2) of [16] when it is noted that N_v in [7] is represented as N (the number of sites along the grain boundary at which atomic jumps take place aided by stress and temperature) in [16] and (Ab) [7] as γ [16]. (N_v and N are defined somewhat differently in the two papers, but the physical picture is very similar.) Post-1990, our model was improved upon significantly by introducing many microstructural details concerning the general high-angle boundaries [10–15] because by then the controversies regarding the structure of general high-angle grain boundaries had got settled and understanding in terms of the structural unit model had emerged [17–21].

In brief, in the model the rate controlling processes are assumed to be confined to the grain/interphase boundary regions. High-angle boundaries, along which boundary sliding is concentrated [22,23], are divided into atomic-scale ensembles that surround free volume sites present at discrete locations on the boundary characteristic of misorientation and the nature and magnitude of inter-atomic forces. Due to the presence of free

* Corresponding author. Tel.: +91 40 2313 4455.

E-mail addresses: kapse@uohyd.ernet.in, ananthaster@gmail.com (K.A. Padmanabhan).

volume, these ensembles possess a lower shear modulus compared with the rest of the boundary and hence constitute the basic units of sliding. Microscopic sliding caused by localized shear persists till it is rendered ineffective by steric hindrances like at a triple junction. For GBS to develop to a mesoscopic scale, two or more grain boundaries need to align to form a plane interface, which by further interconnection with other similar plane interfaces will lead to large scale sliding till it gets stopped by an insurmountable barrier like an extra-large grain or a coarse precipitate. This plane interface formation process, brought about by dislocation emission from grain boundaries or diffusion, both of which are regarded as faster than GBS in the model, gives rise to a long-range threshold shear stress, τ_0 , which has to be overcome for mGBS to set in. Free energy minimization and the possibility of the applied stress doing maximum work in this configuration (principle of maximum work) are the reasons for plane interface formation. A mathematical analysis that assumes that the basic sliding unit is of oblate spheroid shape of base diameter ($5a_0$) and height ($2.5a_0$), where a_0 is the inter-atomic distance in the boundary region (\sim equal to the atomic diameter) and that the grain shape is rhombic dodecahedron, leads to Eqs. (1a) and (1b). From bubble raft experiments, the work of Argon [24] and MD simulations [20,21], the free volume fraction inside the basic sliding oblate spheroid is taken in a first order approximation as ~ 0.10 for all superplastic systems.

$$\dot{\gamma} = \frac{2W\gamma_0\nu}{L} \sinh\left(\frac{(\tau - \tau_0)\gamma_0 V_0}{2kT}\right) \exp\left(-\frac{\Delta F_0}{kT}\right) \quad (1a)$$

$$\Delta F_0 = \frac{1}{2}(\beta_1 \gamma_0^2 + \beta_2 \varepsilon_0^2) GV_0 \quad (1b)$$

In Eqs. (1a) and (1b), $\dot{\gamma}$ is the strain rate, W the average grain boundary width ($= 2.5a_0$), γ_0 the free volume fraction present in the basic unit of sliding present in the grain boundaries, which will approximately be equal to the shear strain (dependent on the material; the method of determining it has been given), ν the thermal vibration frequency ($= 10^{13} \text{ s}^{-1}$ or $(kT/h) \text{ s}^{-1}$, with h the Planck constant), τ the applied shear stress, V_0 the volume of the basic sliding unit ($= (2/3)\pi W^3$), k the Boltzmann constant, T the temperature of deformation on the absolute scale, ΔF_0 the free energy of activation for the basic sliding event, G the shear modulus of the basic sliding unit, ε_0 the dilatational strain in a unit sliding event ($= \gamma_0/\sqrt{3}$), if von-Mises yield criterion is assumed) as the oblate spheroid is embedded in a solid matrix, $\beta_1 = 0.944 (1.59 - p/1 - p)$ and $\beta_2 = 4(1 + p)/9(1 - p)$. Where p is Poisson's ratio.

There are no adjustable constants in the analysis. ΔF_0 , and σ_0 , the only unknowns, are obtained directly from the experimental results. (Expressions are available for their theoretical estimation also-Eq. (1b) above and Eqs. (13) and (14) of [10]). The numerical procedures used to solve the transcendental Eq. (1a) with a view to comparing the predictions of the model with experimental findings are also available [10,11,15].

It is known that if von Mises yield criterion is assumed $\tau = H_V/3\sqrt{3}$, when H_V , the hardness of the material, is reported on the Vickers scale. How this relationship gets modified, if other yield criteria like Mohr-Coulomb are used, has also been explained [12,13]. Thus, one obtains Eq. (2) [5,6].

$$H_V = H_{Va} - \frac{m_2}{L} \sqrt{(L - L_0)} \quad (2)$$

here H_V is the measured (steady state) hardness, H_{Va} the hardness equivalent of the applied stress at the moment of load application, m_2 , a constant ($= G\sqrt{L_1}/C$), with C a conversion factor (from shear to hardness, $\tau = CH_V$; $C = 1/3\sqrt{3}$ for von Mises yield criterion), $L_0 (= 2W\sqrt{6})$ the grain size at which τ_0 falls off to zero and L_1 is

Table 1

Degree of fit for the three relations: $H_V \propto \ln(L)$, $H_V \propto L$ and $H_V \propto L^{-0.5}$.

System	L (nm)	H (GPa)	Correlation coefficient of H and		
			ln(L)	L	L ^{-0.5}
Al62.5 Cu2.5 Fe12.5 [4]	38.8	11.41	0.9487	0.9168	0.9623
	23.5	10.46			
	20.6	9.31			
	17.5	8.56			
Zn [25]	11.0	1.06	0.9942	0.9813	0.9979
	7.9	0.84			
	5.9	0.58			
Ni 18Fe [26]	13.9	6.15	0.7867	0.8064	0.7767
	12.7	5.70			
	11.0	5.71			

a convenient notation representing

$$L_1 = 3^{-0.75} 2^{15} N_{\text{pl}}^{-0.5} \frac{\gamma_B}{G\alpha_f} \quad (3)$$

with α_f a form factor (~ 1) and γ_B specific grain boundary energy and N_{pl} the number of grain boundaries that align to form a plane interface at a given value of L . (For obtaining numerical values for N_{pl} using Eq. (2), within a narrow grain size range N_{pl} is treated as independent of L . But in general N_{pl} is a strong function of grain size and temperature.) Using isothermal experimental hardness vs. grain size data reported and Eqs. (2) and (3), not only one can account for the IHP effect, but also predict the number of grains that align to form a plane interface.

In this paper the data presented in [4] and in [25,26] are re-analyzed.

The degree of fit, as determined by coefficient of correlation, for all the three expressions H_V vs. $\ln(L)$, H_V vs. L and H_V vs. $L^{-0.5}$ is very similar—Table 1. On this basis alone it is fair to say that both our approach [5,6] and that of Conrad and Narayan [7,8] account for the experimental results satisfactorily. This finding clearly underlines the dangers in preferring one atomistic mechanism over another merely based on gross correlations.

With reference to the preference of [4] for the model of Conrad and Narayan [7,8] the following observations are in order. (a) Figs. 4 and 5 of [4] suggest that the activation energy for the rate controlling process gets doubled when the same is determined by plotting H_V vs. L instead of H_V vs. $\ln(L)$. This observation is in conflict with the finding [7,8] that very similar activation energy for the rate controlling process result from both types of plots. (b) In the earlier analysis [7,8] the effective stress is taken as \sim the applied stress, i.e., the strain-rate sensitivity index, $m = 1.0$. But, in nanocrystalline materials at room temperature the value of m is in the range 0.02–0.08 [27,28]. In contrast, in our approach [5,6,9–15] the value of m can vary from a very low value to 1.0, depending on the difference between the applied stress and the threshold stress needed to give rise to mesoscopic boundary sliding. Our analysis [5,6,9–15] also suggests (a) a method of calculating the threshold stress, τ_0 (see Eqs. (13) and (14) of [10]) and (b) the strain rate of deformation in terms of the material and experimental parameters, including the free energy of activation, ΔF_0 —Eqs. (1a) and (1b).

In the papers taken up for analysis, the strain rate of the hardness test is not reported. According to [29] this lies in the range of $5 \times 10^{-2} \text{ s}^{-1}$ – $5 \times 10^{-4} \text{ s}^{-1}$. (It is not clear from [4] what value of strain rate was assumed, while determining the activation energy from their Figs. 4 and 5). By assuming that the strain rate range reported [29] is relevant for the results of [4,25,26], a free energy of activation for the rate controlling

Table 2

Average free volume fraction in the basic unit of sliding, the number of grain boundaries that align to form the plane interface during mesoscopic boundary sliding and the free energy of activation for the rate controlling GBS process, according to [9–15].

System: Quasicrystalline Al, L , nm (range) :17.6–38.8					
$G = 74$ GPa		γ_o	N_{PI}	ΔF_o , kJ mol ⁻¹ for	
				$\dot{\gamma} = 5 \times 10^{-2}$, s ⁻¹	$\dot{\gamma} = 5 \times 10^{-4}$, s ⁻¹
1.00G, GPa	74.0	0.0700	1.3689	184.1	198.8
System: Ni–Fe, L , nm (range) :11.0–13.9					
$G = 79.3$ GPa		γ_o	N_{PI}	ΔF_o , kJ mol ⁻¹ for	
				$\dot{\gamma} = 5 \times 10^{-2}$, s ⁻¹	$\dot{\gamma} = 5 \times 10^{-4}$, s ⁻¹
0.70G, GPa	55.5	0.0795	18.0	116.7	129.3
0.75G, GPa	59.5	0.0748	20.7	116.6	129.2
0.80G, GPa	63.4	0.0743	23.6	116.5	129.1
System: Zn, L , nm (range) :6.0–11.0					
$G = 43$ GPa		γ_o	N_{PI}	ΔF_o , kJ mol ⁻¹ for	
				$\dot{\gamma} = 5 \times 10^{-2}$, s ⁻¹	$\dot{\gamma} = 5 \times 10^{-4}$, s ⁻¹
0.70G, GPa	30.1	0.0812	7.8	85.2	97.8
0.75G, GPa	32.3	0.0784	8.9	85.1	97.7
0.80G, GPa	34.4	0.0758	10.2	85.0	97.6

process pertaining to the three sets of results is reported. While predicting the free volume fraction present in basic sliding unit, the number of grain boundaries that align to form plane interfaces and the free energy of activation for the rate controlling process (Eqs. (1a), (1b)–(3) of this paper) for the two nanocrystalline materials, the experimental finding [30,31] that when the grain size is below 15 nm, the shear modulus falls by up to 30% for a grain size of ~ 5 –6 nm is kept in mind. (For the quasi-/nanocrystalline material the value of G is given.) The results are summarized in Table 2.

For the two nanocrystalline materials the shear modulus in the bulk, as reported by Frost and Ashby [32], was used. Based on the present analysis one is able to suggest that in the Al-based nano-/quasicrystalline material the plane interface is made up of 1–2 grain boundaries ($=N_{PI}$). The same increases to 18–24 and 8–10 respectively for the Ni–Fe and Zn- nanocrystalline materials. The likely range of activation energy values (ΔF_o) and free volume fractions (γ_o) in the three cases are also presented in Table 2. The predictions concerning the values of N_{PI} and γ_o can be checked by high-resolution TEM and/or MD simulations by any interested reader.

As capability for prediction of new results is a desirable feature of a model, there appears to be a case in favor of the present analysis.

References

- Padmanabhan KA, Vasin RA, Enikeev FU. Superplastic flow: common basis for a ubiquitous phenomenon. Springer; 2001.
- Chokshi AH, Rosen A, Karch J, Gleiter H. On the validity of the Hall–Petch relationship in nanocrystalline materials. *Scr Metall* 1989;23:1679–83.
- Koch C.C., Narayan J. The inverse Hall–Petch effect—fact or artifact? In: Mukhopadhyay NK, Ali F, Scudino S, Khoshkhoo MS, Stoica M, Srivastava VC, et al. editors. Farkas D, Kung H, Mayo M, Van Swygenhoven H, Weertman J. Symposium proceedings: structure and mechanical properties of nanophase materials – theory and computer simulation vs. experiment, Boston, Massachusetts, USA, 28–30 November 2000: Preface. *Mater Res Soc Symp—Proc* 2001; 634, p B5.1.1–B5.1.11.
- Mukhopadhyay NK, Ali F, Scudino S, Khoshkhoo MS, Stoica M, Srivastava VC, et al. Grain size softening effect in Al62.5Cu25Fe12.5 nanoquasicrystals. *Appl Phys Lett* 2013;103:201914.
- Padmanabhan KA, Nitsche R., Hahn H. On the deformation of nanocrystalline metals and ceramics. In: Fourth European conference on advanced materials, processes., Milano: Associazione Italiana Di Metallurgia; 1995, p. 289–298.
- Hahn H, Padmanabhan KA. A model for the deformation of nanocrystalline materials. *Philos Mag B* 1997;76:559–71.
- Conrad H, Narayan J. On the grain size softening in nanocrystalline materials. *Scr Mater* 2000;42:1025–30.
- Conrad H, Narayan J. Mechanism for grain size softening in nanocrystalline Zn. *Appl Phys Lett* 2002;81:2241–3.
- Padmanabhan KA, Schlipf J. Model for grain boundary sliding and its relevance to optimal structural superplasticity Part 1—Theory. *Mater Sci Technol* 1996;12:391–9.
- Padmanabhan KA, Gleiter H. Optimal structural superplasticity in metals and ceramics of microcrystalline- and nanocrystalline-grain sizes. *Mater Sci Eng, A* 2004;381:28–38.
- Padmanabhan KA, Dinda GP, Hahn H, Gleiter H. Inverse Hall–Petch effect and grain boundary sliding controlled flow in nanocrystalline materials. *Mater Sci Eng, A* 2007;452–453:462–8.
- Padmanabhan KA, Basariya MR. A mesoscopic grain boundary sliding controlled flow model for superplasticity in intermetallics. *Int J Mater Res Former Z Fuer Met* 2009;100:1543–51.
- Padmanabhan KA, Basariya MR. Mesoscopic grain boundary sliding as the rate controlling process for high strain rate superplastic deformation. *Mater Sci Eng, A* 2009;527:225–34.
- Padmanabhan KA. Grain boundary sliding controlled flow and its relevance to superplasticity in metals, alloys, ceramics and intermetallics and strain-rate dependent flow in nanostructured materials. *J Mater Sci* 2009;44:2226–38.
- Sripathi S, Padmanabhan KA. On the experimental validation of a mesoscopic grain boundary sliding-controlled flow model for structural superplasticity. *J Mater Sci n.d.*;49:199–210.
- Padmanabhan KA. A theory of structural superplasticity. *Mater Sci Eng* 1977;29:1–18.
- Sutton A, Vitek V. On the structure of tilt grain boundaries in cubic metals I. Symmetrical tilt boundaries. *Philos Trans R Soc London, Ser Math Phys Sci* 1983;309:1–36.
- Sutton A, Vitek V. On the structure of tilt grain boundaries in cubic metals II. Asymmetrical tilt boundaries. *Philos Trans R Soc London, Ser Math Phys Sci* 1983;309:37–54.
- Sutton AP, Vitek V. On the structure of tilt grain boundaries in cubic metals. III. Generalizations of the structural study and implications for the properties of grain boundaries. *Philos Trans R Soc London, Ser Math Phys Sci* 1983;309:55–68.
- Wolf D. Structure–energy correlation for grain boundaries in F.C.C. metals—III. Symmetrical tilt boundaries. *Acta Metall Mater* 1990;38:781–90.
- Wolf D. Structure–energy correlation for grain boundaries in f.c.c. metals—IV. Asymmetrical twist (general) boundaries. *Acta Metall Mater* 1990;38:791–8.

- [22] Padmanabhan KA, Davies GJ. Superplasticity: mechanical and structural aspects, environmental effects, fundamentals and applications. Springer-Verlag; 1980.
- [23] Nieh TG, Wadsworth J, Sherby OD. Superplasticity in metals and ceramics. Cambridge University Press; 1997.
- [24] Argon AS. Plastic deformation in metallic glasses. *Acta Metall* 1979;27:47–58.
- [25] Conrad H, Narayan J. Mechanisms for grain size hardening and softening in Zn. *Acta Mater* 2002;50:5067–78.
- [26] Cheung C, Djuanda F, Erb U, Palumbo G. Electrodeposition of nanocrystalline Ni–Fe alloys. *Nanostruct Mater* 1995;5:513–23.
- [27] Padmanabhan KA. Mechanical properties of nanostructured materials. *Mater Sci Eng, A* 2001;304–306:200–5.
- [28] Varam S, Rajulapati KV, Bhanu Sankara Rao K. Strain rate sensitivity studies on bulk nanocrystalline aluminium by nanoindentation. *J Alloys Compd* 2014;585:795–9.
- [29] Maier V, Durst K, Mueller J, Backes B, Höppel HW, Göken M. Nanoindentation strain-rate jump tests for determining the local strain-rate sensitivity in nanocrystalline Ni and ultrafine-grained Al. *J Mater Res* 2011;26:1421–30.
- [30] Grewer M, Markmann J, Karos R, Arnold W, Birringer R. Shear softening of grain boundaries in nanocrystalline Pd. *Acta Mater* 2011;59:1523–9.
- [31] Grewer M, Birringer R. Shear shuffling governs plastic flow in nanocrystalline metals: an analysis of thermal activation parameters. *ArXiv14042457 Cond-Mat*. 2014.
- [32] Frost HJ, Ashby MF. Deformation–mechanism maps: the plasticity and creep of metals and ceramics. Pergamon Press; 1982.

On the experimental validation of a mesoscopic grain boundary sliding-controlled flow model for structural superplasticity

Sriharsha Sripathi · K. A. Padmanabhan

Received: 18 May 2013 / Accepted: 22 August 2013 / Published online: 4 September 2013
© Springer Science+Business Media New York 2013

Abstract Different mechanisms have been suggested by many authors as controlling the rate of superplastic flow in different materials. From the viewpoint of computational effort and aesthetics, it is highly desirable to explain the phenomenon, independent of the material/system considered, on a common basis. With this aim, a mesoscopic grain boundary sliding-controlled deformation model was proposed sometime ago as being responsible for superplastic flow in materials of different kinds. In this paper, a rigorous numerical computational procedure for the experimental validation of the model, which takes into account all the physical requirements of the model, is presented. The soundness of the new procedure is established by analysing the experimental data pertaining to many systems belonging to different classes of materials, and matching the results of the analysis with the experimental findings.

Introduction

The subject of superplasticity has been reviewed extensively. Often, the phenomenon is described by Eq. 1 [1, 2].

$$\dot{\epsilon} = a \frac{\sigma^n}{d^{a'}} \exp\left(-\frac{Q}{kT}\right) \quad (1)$$

where $\dot{\epsilon}$ is the strain rate, a and a' are constants, d is the average grain size, σ is the external stress, n is the stress exponent (inverse of the strain rate sensitivity index, m), Q is

the activation energy, k is the Boltzmann constant and T is the absolute temperature of deformation. For significant superplastic elongation in tension, m has to satisfy the condition $0.3 \leq m \leq 1$ in a strain rate range $\dot{\epsilon}_{\min} \leq \dot{\epsilon} \leq \dot{\epsilon}_{\max}$; i.e. there is a lower and upper bound to the strain rate range of significant superplasticity. The grain size should be less than $\sim 10 \mu\text{m}$ for metals and $\sim 1 \mu\text{m}$ or less for ceramics and should remain relatively stable during deformation. The many ways of achieving a refined, relatively stable microstructure are well reviewed [2–5]. Superplasticity appears to be a near-ubiquitous phenomenon observed in many different classes of materials [6]. Some recent/unconventional examples are nanostructured materials, earth's lower mantle, ice having fine grain size, bulk metallic glasses and carbon nanotubes [7–9].

A model in which grain boundary sliding (GBS) that develops to a mesoscopic scale (defined to be of the order of a grain diameter or more) was proposed sometime ago and developed over a period of time. It has also been validated approximately using experimental data pertaining to a few systems and approximate numerical procedures. A detailed description of the model and the earlier validation procedures can be found elsewhere [6, 10–18]. A brief report on an improved algorithm (and computer code) for validating the model was presented recently at a conference [19]. In this paper, a detailed description of the new method is provided and the results of the present analysis are compared with the earlier findings. The predictions of the analysis are validated using experimental results pertaining to several alloys and material classes.

Creep-based approach

A constitutive equation often used to analyse high-temperature creep is represented as Eqs. 2a or 2b [20].

S. Sripathi · K. A. Padmanabhan (✉)
School of Engineering Sciences and Technology, University of
Hyderabad, Gachibowli, Hyderabad 500 046, India
e-mail: kap@annauniv.edu; kapse@uohyd.ernet.in;
ananthaster@gmail.com

S. Sripathi
e-mail: sripathi1@yahoo.com

$$\dot{\epsilon} = A \frac{DGb}{kT} \left(\frac{b}{d}\right)^p \left(\frac{\sigma}{G}\right)^n \quad (2a)$$

$$\dot{\epsilon} = A \frac{DGb}{kT} \left(\frac{b}{d}\right)^p \left(\frac{\sigma - \sigma_0}{G}\right)^n \quad (2b)$$

where A and p are empirical constants, D is the appropriate diffusivity (lattice, grain boundary or mixed/effective, given as $D = D_0 \exp(-Q/kT)$, where D_0 is the pre-exponential (frequency) factor, Q is the activation energy for the rate-controlling process), G is the shear modulus at the test temperature, b is the Burgers vector and d is the average grain size. Eqs. 2a, 2b have been assumed, without proof to be relevant to superplasticity also. As $\ln \dot{\epsilon} - \ln \sigma$ plots over a wide range are not linear, at times a threshold stress, σ_0 [21], considered to be necessary for the onset of superplasticity is included (Eq. 2b). Using Eqs. 2a, 2b, different rate-controlling mechanisms have been suggested for different materials and no unification of the interpretations has been attempted.

In the present manuscript, we develop a rigorous computational procedure for analysing superplasticity data in the context of the mesoscopic GBS model. We apply this analysis to previously reported measurements in a wide variety of materials systems. The results show very similar values for the threshold stress and the free energy of activation for materials of similar composition and are consistent with the notion that a unique rate-controlling mechanism underpins superplastic flow in materials of all classes and grain size ranges.

Mesoscopic GBS-controlled model for superplastic deformation [6, 10–18]

In this model, a high-angle grain boundary is divided into a number of atomic scale ensembles that surround free volume sites present at discrete locations, which depend on the boundary misorientation, material composition (which in turn, determines the nature and magnitude of inter-atomic forces and electronic interactions) and experimental conditions. Due to the presence of free volume, which depends on the variables listed above, these ensembles possess a lower shear modulus than the rest of the boundary and constitute the basic units of sliding. The shape of the basic sliding unit is assumed to be an oblate spheroid (see Fig. 1a), on average of length equal to 5 atomic diameters in the boundary plane and height 2.5 atomic diameters (equal to the average grain boundary width, as revealed by many field ion microscopic studies) in the perpendicular direction. (This shape is chosen for mathematical development, as a uniform stress–strain field that develops inside a deformed oblate spheroid is already worked out [22]. The real shape could even be irregular and this is taken into

account by introducing a form factor of the order of unity [10]). It is assumed that the rate-controlling process is confined within the grain boundary region (Fig. 1b, c). Atomic scale sliding persists till it is rendered ineffective by steric hindrance, e.g. a triple junction (Fig. 1d). For GBS to develop to a mesoscopic scale, two or more grains need to align to form a plane interface (Fig. 1e).

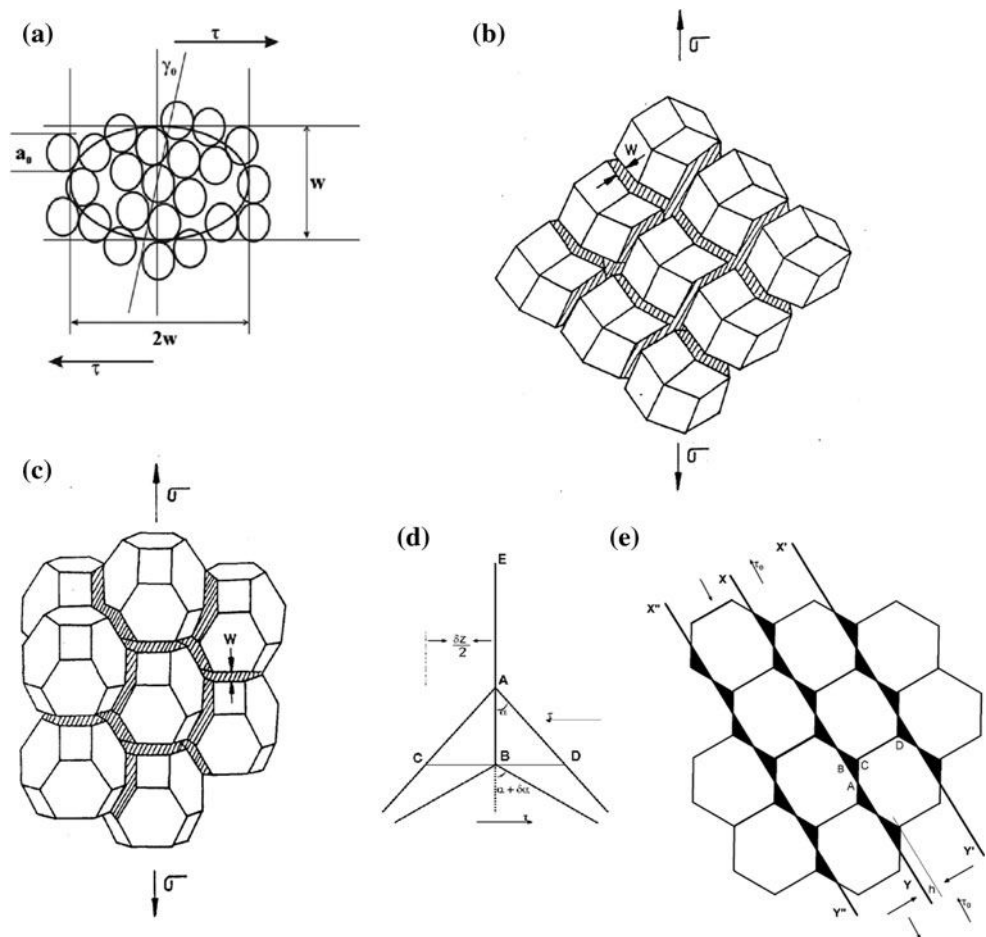
Further interconnection of similar plane interfaces can lead to long-range sliding till it gets stopped by an insurmountable barrier, e.g. a very large grain or a big precipitate. Thus this model views GBS as a two-scale process, where deformation at a boundary (atomic/microscopic scale) develops to a mesoscopic scale in the second stage. The driving force for plane interface formation is the minimization of the total free energy of the deforming system and the work done by the external stress reaching its maximum value for this configuration (Taylor's principle of maximum work). It is easy to show that the extension of the boundary EA in Fig. 1d downwards to EB will lead to a decrease in the total free energy of the deforming system. In the limit, the triple junction will be transformed into a horizontal line, i.e. a plane interface [14]. These processes give rise to a long-range threshold stress which has to be overcome for mesoscopic GBS to set in. Equation 3 represents the mathematical form of the mesoscopic GBS-controlled model for superplastic deformation, which is suggested to be relevant for understanding the superplastic behaviour of materials of all kinds and having grain size in the μm , sub- μm or nm range [10, 14, 19]:

$$\dot{\epsilon} = \frac{2cW\gamma_0 v}{d} \sinh\left(\frac{(\sigma - \sigma_0)c\gamma_0 V_0}{2kT}\right) \exp\left(-\frac{\Delta F_0}{kT}\right) \quad (3)$$

where, $V_0 = \frac{2}{3}\pi W^3$; $v = \frac{kT}{h}$ or 10^{13} s^{-1} ; $W = 2.5a_0$; ΔF_0 is the free energy of activation for the basic sliding event,¹ γ_0 is the shear strain produced in a unit sliding event, V_0 is the volume of the basic sliding unit (an oblate spheroid), W is the grain boundary width, a_0 is the atomic diameter, v is the thermal vibration frequency, ($= kT/h$ or 10^{13} s^{-1}), h is the Planck constant, c is a yield criterion-dependent constant and σ_0 is the threshold stress necessary for the onset of mesoscopic boundary sliding. The threshold shear stress in case of the present systems studied, in all of which the

¹ ΔF_0 is the sum of E_{trans} , the change in the internal energy when the oblate spheroid gets sheared in the absence of the surrounding matrix, E_{el} , the elastic strain energy of the deformed oblate spheroid and E_{int} , the interaction energy of the elastic field. It is assumed that the constrained shear transformation (inside the solid matrix) occurs without any heat flow. ΔF_0 can be interpreted equivalently as the enthalpy change of the deformed oblate spheroid, the enthalpy change of the deformed oblate spheroid plus matrix or the change of internal energy of the deformed oblate spheroid, matrix and loading mechanism regarded as a simple thermodynamic system. (Read 'Helmholtz free energy' for 'internal energy' and 'Gibbs free energy' for 'enthalpy' [22]).

Fig. 1 **a** Sliding/Shear unit, according to the GBS Model [6], **b** & **c** shaded grain boundaries of rhombic dodecahedral and tetrakai decahedral grains within which the rate-controlling process is confined [10], **d** shear stress-driven movement of a boundary triple junction to lower the overall free energy of the system, **e**: resulting planar interfaces (along XY, X'Y', X''Y'', etc.), which result when the atoms located in the shaded regions are moved by the extension of the boundaries normal to the shear direction to reach the sliding boundary planes [14]



average grain size is much greater than ~10–15 nm, is given by Eq. 3 [14]:

$$\tau_o = \left(\frac{8G\Gamma_B r}{3^{0.25}} \right)^{0.25} \frac{1}{d} \tag{4}$$

where, Γ_B is the specific grain boundary energy and r is the residual misfit which is removed by diffusion (an accommodating process faster than GBS). From Eq. 4 it is seen that at a given grain size, τ_o decreases with increasing temperature (G decreases with increasing T) and at a fixed temperature it increases with decreasing grain size (due to more number of grain boundaries aligning themselves to form the plane interface on decreasing the grain size).

The free energy of activation for the rate-controlling process is computed using Eq. 5 [22].

$$\Delta F_o = \frac{1}{2} (\beta_1 \gamma_o^2 + \beta_2 \varepsilon_o^2) G V_o \tag{5}$$

where ε_o is the unit dilatation strain, derived from the value of the unit shear strain as $(= \gamma_o \times c)$, β_1 and β_2 are constants appropriate to the oblate spheroid shape and are given by $\beta_1 = 0.944 \left(\frac{1.59-p}{1-p} \right)$; $\beta_2 = \frac{4}{9} \left(\frac{1+p}{1-p} \right)$, where p is Poisson's ratio.

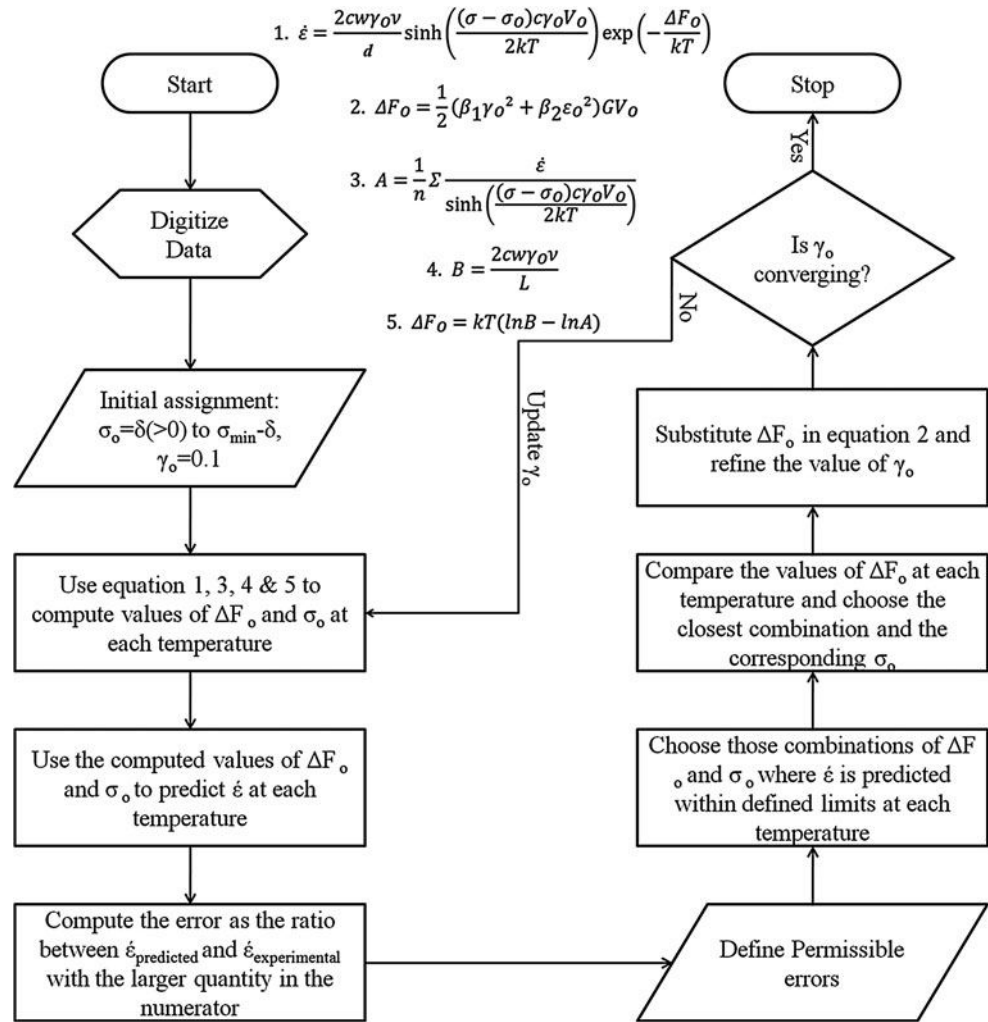
New algorithm and computer code

Figure 2 presents a new algorithm developed for validating the mesoscopic GBS-controlled flow model for superplasticity. The inputs for the algorithm are the experimentally generated data of stress and strain rate at different temperatures and grain sizes for the different systems, as reported in the literature. The atomic diameter and the shear modulus at different temperatures are also taken from literature. The tolerances for the computed values have been prescribed keeping the maximum experimental accuracies in mind.

The variations in the magnitude of the unit shear strain produced in a boundary sliding event and the threshold stress necessary for the onset of mesoscopic boundary sliding, as a function of grain size and temperature or temperature, as the case may be, should be consistent with the requirements of the physical model. Data points relevant to optimal superplastic flow (regions I and IIa [2], where m increases with increasing strain rate) were digitized manually.

The computational procedure consists of two stages. In the first stage the value of the free energy of activation and the corresponding threshold stress are computed assuming

Fig. 2 Flow chart describing the algorithm. ΔF_0 free energy of activation, γ_0 unit shear strain, V_0 volume of the basic sliding unit, W grain boundary width, a_0 atomic diameter, ν thermal vibration frequency, k Boltzmann constant, c yield criterion-dependent constant, σ_0 threshold stress, $\dot{\epsilon}$ strain rate, d grain size, σ external stress, G shear modulus at temperature T and β_1 and β_2 constants defined below Eq. 5



the value of the average unit shear strain, γ_0 , to be ~ 0.10 (based on bubble raft experiments and MD simulations [23, 24]). In the next stage, the computed value of the free energy of activation is matched with the prediction of Eq. 5 and the value of the unit shear strain is so adjusted that they agree. As shown in the algorithm (Fig. 2), this is done iteratively till a consistent value of the unit shear strain is obtained, which satisfies all the equations simultaneously.

The predictions of the analysis were matched with the experimental results with the standard deviation (SD), average error (AE) and correlation coefficient (CC) as the criteria, Eq. 6.

$$SD = \left(\frac{\sum (\dot{\epsilon}_{\text{expt}} - \dot{\epsilon}_{\text{pred}})^2}{N - 2} \right)^{0.5}; \quad AE = \frac{SD}{\sqrt{N}};$$

$$CC = \left(\frac{\sum (\dot{\epsilon}_{\text{expt}} \dot{\epsilon}_{\text{pred}}) - N \dot{\epsilon}_{\text{m expt}} \dot{\epsilon}_{\text{m pred}}}{\left(\sum \dot{\epsilon}_{\text{expt}}^2 - N \dot{\epsilon}_{\text{m expt}}^2 \right) \left(\sum \dot{\epsilon}_{\text{pred}}^2 - N \dot{\epsilon}_{\text{m pred}}^2 \right)} \right)^{0.5} \quad (6)$$

Here $\dot{\epsilon}_{\text{pred}}$, $\dot{\epsilon}_{\text{expt}}$ are the predicted and experimental strain rate values, respectively, $\dot{\epsilon}_{\text{m pred}}$, $\dot{\epsilon}_{\text{m expt}}$ are the mean of the experimental and predicted strain rate values and N is the number of experimental stress–strain rate pairs taken at each temperature for the analysis.

The algorithm presented in Fig. 2 works as follows. The initial value of γ_0 is taken as 0.10. σ_0 is assigned values starting from δ to $(\sigma_{\min} - \delta)$, with $\delta = 0.001\sigma_{\min}$, where σ_{\min} is the minimum stress applied at the given temperature for which an experimental datum point is available. At each temperature, in Eq. 3 using the mean of the experimental values of the stress and the corresponding strain rate, ΔF_0 for each of the σ_0 values is computed. At all temperatures, those combinations of ΔF_0 – σ_0 which fell within a prescribed error range (chosen based on the experimental accuracies) were accepted and those ΔF_0 values, which together for all the test temperatures employed for the particular material formed the closest numerical set, and the corresponding σ_0 values were

chosen. ΔF_0 value so chosen at each temperature was used, along with Eq. 5, to refine the value of γ_0 iteratively till a near-stable value, which satisfies Eqs. 3 and 5 simultaneously is obtained. Evidently, this method is an improvement on the earlier validation procedures [14–17].

As a single mechanism is assumed to operate in the entire experimental region of interest, the free energy of activation should be independent of temperature for each system.

Systems analysed

Table 1 presents the details of the systems analysed by different authors and a summary of the results thus obtained. 4 magnesium-based alloys, 2 each of zinc-, aluminium- and copper-based alloys, a silicon nitride and 3 each of zirconia and alumina–zirconia–mullite are the materials of interest. Superplastic intermetallic alloy systems are considered separately in Appendix A, because one more author was involved in that work.

Earlier analyses

In this section the ideas on the threshold stress, constitutive equation, the free energy of activation and the rate-controlling mechanism for the different materials, as reported by the different authors, are summarized.

In papers dealing with Mg1, Cu1-2 and Zr1-2 systems the threshold stress is considered to be absent/neglected. But, the authors of Mg2 and Ac2 believe that superplastic flow is accompanied by a threshold stress. In Al1, which uses a variant of Eq. 2a, G is replaced by the elastic modulus E. The authors of papers dealing with Mg3, Mg4, Zr1-3, Ac1-3 and Si1 use Eq. 1. The paper dealing with Mg4 makes a mention of the threshold stress, but has not included it in any rate equation.

The investigators of the zinc-based and the copper-based systems have not reported any activation energy for the rate-controlling process. In some cases (Zr3, Ac1) the activation energies are reported at different stress levels. But, in Table 1, for clarity, only the values for the lowest and the highest stress levels are given. When Eq. 1 is used

Table 1 Details of the systems analysed

Tag ^a	System composition	Test temperatures (K)	Initial grain size (μm)	Reported values of	
				<i>m</i> (range)	<i>Q</i> (kJ mol ⁻¹)
Magnesium-based alloys[†]					
Mg1	Mg 6.19Zn 1.1Y 0.46Y [25]	673, 698, 723	5.2	0.20–0.75	92
Mg2	Mg 4Y 0.4Nd 0.7ZrO ₂ [26]	598, 623, 648, 673	2		126
Mg3	Mg 5.8Zn 1Y 0.48Zr [27]	673, 723, 753	~ 15–20		76, 213
Mg4	Mg 3Zn 0.5 Y 1.5 Zr [28]	648, 673, 698, 723	5		107.8, 146.3
Zinc-based alloys[†]					
Zn1	Zn 22Al [29]	398, 453, 518, 545	0.9	0.35–0.50	Unreported
Zn2	Zn 22Al [30]	423, 473, 503	2.5		
Quasi-single phase copper alloys[†]					
Cu1	Cu 2.8Al 1.8Si 0.4Co [31]	723, 773, 823, 873	7	0.20–0.38	Unreported
Cu2	Cu 2.8Al 1.8Si 0.4Co [31]	673, 723, 773, 823	3		
Aluminium-based alloys[†]					
Al1	Al 8.9Zn 2 Mg 0.09Sc [32]	493, 523, 563, 583, 603	0.68	0.05–0.55	142
Al2	Al 3 Mg 0.2Sc [33]	573, 623, 673 723	0.2		120, 90
Zirconia-based ceramics/composites[‡]					
Zr1	ZrO ₂ 3Y ₂ O ₃ [34]	1523, 1573, 1623, 1673, 1723	0.51	0.45–0.58	533
Zr2	ZrO ₂ 4Y ₂ O ₃ [34]		0.75		
Zr3	ZrO ₂ 8Y ₂ O ₃ 10Al ₂ O ₃ [35]	1573, 1623, 1673, 1723	1.1		597, 683
Alumina-based ceramics/composites[#]					
Ac1	Al ₂ O ₃ 20Zr ₂ O ₃ 30Al ₁₆ Si ₂ O ₁₃ [36]	1673, 1723, 1773	0.39	0.33–0.58	911, 840
Ac2	Al ₂ O ₃ 20Zr ₂ O ₃ 30Al ₁₆ Si ₂ O ₁₃ [37]		0.4		870
Ac3	Al ₂ O ₃ 25 NiAl ₂ O ₄ 25 3Y ₂ O ₃ Zr ₂ O ₃ [38]	1623, 1648, 1673, 1698, 1723	1.3		377, 368
Silicon nitride ceramic					
Si1	Si ₃ N ₄ [39]	1723, 1773, 1823, 1873	0.068	0.5 to ~ 1	574.8, 852.8

^a The ‘Tag’ from this point onward, refers to the system designation in the form given here. The compositions are weight, volume or mole percentage, as shown by the superscripts †, ‡ and #, respectively

to describe the flow, the activation energy can be calculated from the slope of an Arrhenius plot at a constant stress or constant strain rate [40]. In the papers dealing with Mg3, Zr1-3, Ac1-3 and Si1 the activation energy at constant stress is reported using Eq. 7. In case of Mg4 the activation energy at constant strain rate is estimated based on Eq. 8. Both these are ‘apparent’ values. (Their interrelationship $\Delta F_{\sigma, \sigma} = n\Delta F_{\dot{\epsilon}, \dot{\epsilon}}$ was established quite a while ago [40]).

$$Q_{\sigma} = \left(-R \frac{\partial \ln \dot{\epsilon}}{\partial (1/T)} \right)_{\sigma} \quad (7)$$

$$Q_{\dot{\epsilon}} = \left(nR \frac{\partial \ln \dot{\epsilon}}{\partial (1/T)} \right)_{\dot{\epsilon}} \quad (8)$$

Table 1 reveals significant differences in the values of the activation energy even for very similar alloys. As a result, different rate-controlling mechanisms have been suggested. More importantly in none of these papers the model for the rate-controlling mechanism has been derived in detail. They are decided based mostly on the values of n and Q and a guess about the magnitude of the activation energy for diffusion (no diffusion measurements were made). The value of the activation energy being vastly different for systems of very similar composition is sometimes due to incorrect handling of the rate equation. A standard protocol to handle the rate equation is missing. The picture is confusing also because diffusion data for complex alloys, ceramics and composites are not available and many superplastic alloys fall in these categories.

Details of the analysis

The material properties required for the current analysis are the atomic diameter, a_0 ; the shear modulus, G ; C_d , the coefficient of variation of the shear modulus with T ; Poisson’s ratio p and the melting temperature T_m . All these values are available in standard literature. In cases where a single element constituted more than 90 % of the material, the properties used for the analysis corresponded to those of the major element. For some systems, where the other elements were present in greater amounts, the values of G , p and T_m could be taken from existing literature. But, in case of systems Ac1-3, which are multiphase composites, the value of G was obtained by the rule of mixtures, p and T_m were taken to be approximately equal to those of the principal component (as these values were not available for each constituent). Following Frost and Ashby [41], C_d and the atomic diameter for all the systems were chosen as those of the corresponding major constituent.

For zirconia-based systems and when the system properties were approximated by those of the principal constituent, the values of G , p , T_m and C_d were taken from

[42]; for the system Mg4 the grain size was obtained from the author through personal correspondence; for the 3-phase ceramic/ceramic composite systems, p , T_m and C_d were taken from [43, 44] and for the silicon nitride ceramic system, G , p , T_m and C_d were obtained from [45, 46]. The atomic diameters for all the systems were taken from [42].

Results

A total of 33 systems were analysed using the improved algorithm described here. The grain sizes of these systems vary over a wide range: nano, sub-micron and micron ranges; different classes of materials involved: metallic (quasi-single phase and microduplex), ceramic, ceramic composite and material with a quasi-crystalline phase and (in Appendix A) intermetallics were analysed. Zr3, Ac1-3 and Si1 were tested in compression and the rest in tension.

In Appendix A, the results of the intermetallics, as analysed earlier as also using the current algorithm, are presented. With the improved algorithm, the predictions are better and also the algorithm is statistically more correct.

The origin of Region I in the sigmoidal $\log \sigma - \log \dot{\epsilon}$ plot of superplastic flow is attributed at times to dynamic grain growth. In our opinion, such a significant decrease in the value of m in region I cannot arise from this term alone. In fact, the sigmoidal plots are made soon after the steady-state conditions are reached during superplastic flow. In near-isotropic alloys, in which category many, if not most, superplastic materials fall, such a steady state is reached after <10–20 % elongation [47]. It is highly unlikely that the grain size would have increased so significantly to reduce the ‘ m ’ value drastically within such a short strain interval. Hence our present case is in favour of the presence of a threshold stress for the onset of superplastic deformation. In addition, d in Eq. 3 should correspond to the strain at which the $\log \sigma - \log \dot{\epsilon}$ plot is generated. For the same strain, this grain size would be different for each of the test temperatures. These values are not reported for any of the systems. Therefore, in all cases the starting grain size was taken as equal to d . This is an approximation. The present analysis has been carried out within these restrictions.

It is seen that the mesoscopic GBS-controlled flow model could predict the strain rates very well for all classes of materials of grain sizes in the different ranges mentioned. The maximum value of tolerance (defined as the larger of the $(\dot{\epsilon}_{\text{experimental}}/\dot{\epsilon}_{\text{predicted}})$ and $(\dot{\epsilon}_{\text{predicted}}/\dot{\epsilon}_{\text{experimental}})$ ratios) required was ~ 6.3 for Zn1. The best prediction was for Zc3, with the minimum and maximum tolerances being ~ 1.02 and ~ 1.08 , respectively. The maximum and minimum

values of the coefficient of correlation among all the systems were 0.9998 and 0.8897, respectively.

Table 2 presents the results comparing the predictions for a few systems of similar compositions. $\Delta F_{o, \text{diff}}$ is the difference between the maximum and the minimum values of the free energy of activation for all the similar systems put together. cc_{γ_0} is the coefficient of correlation for γ_0 values for all the systems and T values. From Table 2 it is clear that the variation in the value of the free energy of activation is below 42 kJ mol^{-1} , the commonly found scatter in the activation energy reported in the literature among the best estimates of that parameter. Therefore, the presently observed minor variation is attributed to experimental scatter and the small compositional differences present in the alloys tested [48].

Refined values of γ_0 for some of the similar systems were comparable. From Table 2 it is seen that the correlation coefficient for γ_0 for the Zn 1–2 systems is the highest. This is because both the systems were of the same composition.

Similarly when two out of the four magnesium-based systems, Mg1 and Mg4, were compared, the correlation coefficient was high. However, when the other magnesium systems (of different compositions) were also considered together, the correlation coefficient decreased. Hence it is clear that γ_0 values for similar systems are of similar magnitudes and they also vary similarly as a function of the experimental conditions and as required by theory (i.e. it increases with increasing T). The correlation coefficients for the other similar systems are also shown in Table 2. The correlation coefficient for Ac1-2 systems is relatively low, but the tolerances and the match between the experimental and the calculated strain rates were very good.

In Table 2 the maximum values of the tolerance, standard deviation, average error and the minimum value of the correlation coefficient obtained are displayed. These statistical parameters clearly demonstrate that cutting across material class and grain size range the accuracy of predictions of the mesoscopic GBS-controlled flow model is very good.

Table 2 Statistical analysis of the results for similar systems

Systems	$\Delta F_{o, \text{diff}} \text{ kJ mol}^{-1}$	cc_{γ_0}	Maximum			Minimum CC
			Tolerance	SD	AE	
Zn1 and Zn2	20	0.9776	6.3069	0.1048	0.0349	0.9176
Zr1, Zr2 and Zr3	39	0.9137	2.4312	0.0266	0.0109	0.9231
Mg1 and Mg4	21	0.9781	2.7596	0.0537	0.0240	0.9354
Ac1 and Ac2	36	0.6667	1.8876	0.0298	0.0111	0.9665

Table 3 Results in detail

System	T (K)	$\Delta F_o, (\text{KJ mol}^{-1})$	γ_0	σ_o (MPa)	Maximum Tol	SD	AE	CC
Zr1	1523	379	0.0959	12.91	1.2997	0.0022	0.0008	0.9859
	1573	374	0.0964	12.90	1.3198	0.0044	0.0017	0.9871
	1623	378	0.0981	8.24	1.3898	0.0065	0.0027	0.9908
	1673	376	0.0991	7.97	1.3300	0.0098	0.0040	0.9914
	1723	390	0.1023	2.40	2.0899	0.0106	0.0035	0.9675
Ac1	1673	381	0.0887	14.48	1.1237	0.0032	0.0016	0.9972
	1723	364	0.0892	14.34	1.1697	0.0126	0.0063	0.9945
	1773	353	0.0908	12.48	1.0906	0.0222	0.0111	0.9960
Cu1	723	160	0.0996	27.59	1.1667	0.0021	0.0011	0.9785
	773	166	0.1016	15.94	1.4182	0.0037	0.0017	0.9560
	823	171	0.1033	10.18	1.5375	0.0049	0.0020	0.9705
	873	176	0.1046	7.53	2.4491	0.0114	0.0040	0.9444
Si1	1723	450	0.1285	12.43	1.1880	0.0027	0.0010	0.9936
	1773	445	0.1287	8.32	1.2612	0.0065	0.0026	0.9981
	1823	444	0.1287	3.72	1.2612	0.0059	0.0024	0.9967
	1873	440	0.1289	3.24	1.1418	0.0058	0.0026	0.9984

It is seen that some data for similar systems fit to better tolerances than some others. Experimental data for a large number of similar systems need to be analysed and more accurate values for γ_0 and σ_0 need to be obtained for these system-dependent physical constants to be used as standard values for very accurate strain rate predictions in commercial software packages.

Table 3 presents the results in detail for some of the systems. Stress versus the predicted and experimental strain rates for these systems are presented in Fig. 3. The experimental points are represented by symbols; each symbol is associated with a particular temperature. The predicted values appear as full lines (a least squares fit was used for getting the model constants and predicting the strain rates). The insets of these plots reveal the small scatter in the values of free energy of activation as a function of the test temperature.

For the systems presented in Table 3, as expected from theory, γ_0 increased with increasing test temperature in all systems. The value of γ_0 strongly depends on the value of the shear modulus. Hence with more detailed experimentation/theoretical development in the estimation of G and availability of more accurate G values, highly reliable material and temperature-specific sets of γ_0 values may be generated for future use.

According to theory, σ_0 should decrease with increasing T . This is verified in all but one case. To identify the reasons for this exception (which could be due to experimental scatter or some unknown reason), a more detailed study of the behaviour of σ_0 is presently underway.

The atomic diameter used here for calculations corresponds to those of the principal constituent of each alloy. This will not matter much because the atomic diameter is a very small quantity. Many previous calculations have

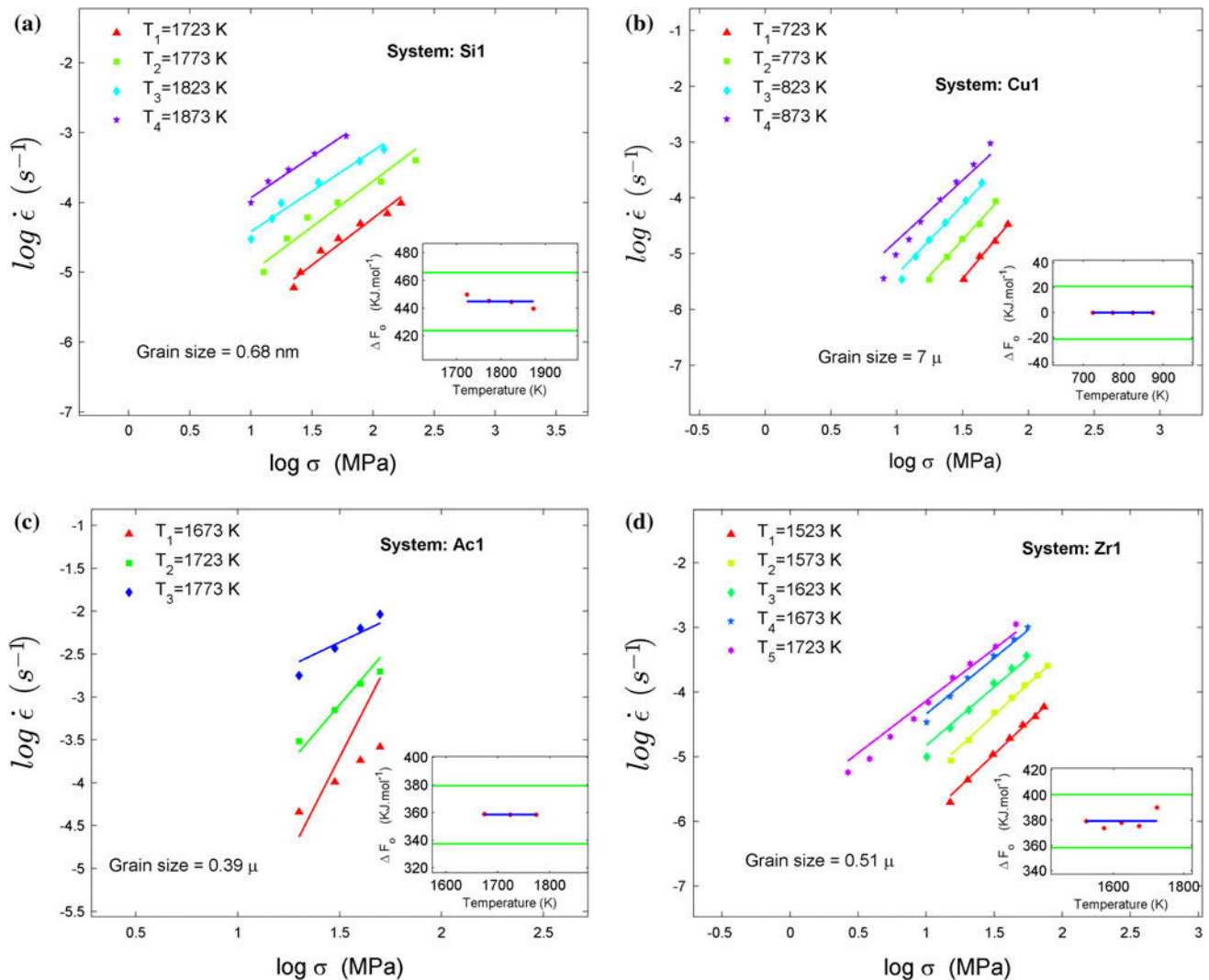


Fig. 3 a–d Predicted and experimental strain rates versus stress plots on a log–log scale for the systems discussed in Table 3

Table 4 Maximum changes in ΔF_0 , σ_0 and Tol when the yield criterion is changed

Tag	T	Von Mises			Tresca			Mohr–Coulomb		
		ΔF_0	σ_0	Tol	ΔF_0	σ_0	Tol	ΔF_0	σ_0	Tol
Mg1	723	126	1.21	1.23	124	1.21	1.23	124	1.21	1.23
Mg2	648	132	0.42	2.76	130	0.42	2.76	130	0.42	2.76
Mg3	753	132	0.89	1.40	131	0.89	1.40	131	0.89	1.40
Mg4	648	129	2.02	3.28	127	2.02	3.28	127	2.02	3.42
Zn1	545	102	2.91	1.55	100	3.54	1.50	101	3.54	1.50
Zn2	423	84	26.94	4.71	83	27.05	5.00	83	26.00	6.06
Cu1	873	175	7.53	2.45	173	7.53	2.45	174	7.31	2.56
Cu2	823	162	9.49	8.59	160	9.49	8.59	161	8.84	10.3
Al1	563	103	13.92	2.54	101	13.83	2.55	102	13.72	2.56
Al2	723	130	3.16	3.16	128	3.16	2.00	128	3.16	2.00
Zr1	1723	390	2.40	2.09	387	2.40	2.09	386	2.40	2.09
Zr2	1523	386	3.45	2.13	366	3.84	8.27	383	3.37	2.11
Zr3	1723	351	3.00	1.45	348	2.80	1.46	348	2.79	1.46
Ac1	1673	381	14.48	1.13	372	17.54	1.73	378	13.73	1.13
Ac2	1773	362	1.84	1.84	358	1.84	1.84	358	4.59	1.85
Ac3	1723	371	4.10	1.04	367	4.11	1.04	367	4.11	1.04
Si1	1723	450	12.43	1.19	446	12.43	1.19	446	12.43	1.19

The units are T , K; ΔF_0 , kJ mol^{-1} , σ_0 , MPa

shown that small changes in this value do not affect the predictions significantly.

In this model, a fundamental sliding event involves a cluster of atoms which has free volume present in it. This is responsible for the shear yield stress in this basic sliding unit being less than that in the rest of the grain boundary and the resulting unit shear. Such a line of argument would suggest that the shear modulus should decrease with decreasing grain size and this effect should become prominent in the nm—grain size range, where the grain boundary to grain interior area ratio is high. Experimental support for this statement is available [49]. These authors have shown experimentally that when the grain size of nanocrystalline Pd falls below about 20 nm the shear modulus decreases by about 30 % compared with that for the bulk. Presently ab initio calculations are underway to determine the shear modulus of the oblate spheroid as a function of the free volume ratio.

Another point of interest is Eq. 5 which suggests that as the oblate spheroid is embedded in a solid matrix, the free energy of activation would be affected by the hydrostatic component of the stress system. Then it would be more appropriate to use a hydrostatic pressure-dependent yield criterion e.g. Mohr–Coulomb, than von Mises or Tresca yield criterion. This is done in Table 4 in which the computed values of the free energy of activation, the threshold stress and the ratio of the experimental and calculated strain rates (tolerance) are compared. In this Table the

values of the free energy of activation, the threshold stress and the tolerance for each system, when the yield criterion used is changed from von Mises to either Tresca or Mohr–Coulomb are presented. As the values of the free energy of activation were least sensitive to the yield criterion, the values of ΔF_0 , σ_0 and Tol for all the systems at that temperature where ΔF_0 changed the most on changing the yield criterion are presented in Table 4. It is clear that the differences in the free energy of activation are rather small and the yield criterion chosen does not also appear to affect the accuracy of prediction of the strain rate significantly.

However, the threshold stress seems to be influenced strongly by the yield criterion chosen. A statistical analysis for understanding the behaviour of the threshold stress is presently underway.

Conclusions

The predictions based on the mesoscopic GBS-controlled flow model for superplastic deformation are well within order of magnitude accuracy with respect to the experimental results concerning all the systems studied. The systems taken up for investigation included pseudo-single phase and microduplex metallic alloys, ceramic and ceramic composite systems and alloys containing quasi-crystalline particles and intermetallics. Tensile as well as compressive stress–strain rate datasets were used to

validate the analysis. The grain size range covered by these materials was also wide: micron, sub-micron and nanocrystalline. Activation energies for similar systems are close and the system- and temperature-dependent values of the unit shear strain, which according to theory should increase in magnitude with increasing temperature, obey that prediction. The applicability of this model to many classes of materials studied over a wide grain size range makes this model attractive from physical, computational and aesthetic points of view.

Acknowledgement *N.B.* The computer programme used to carry out the present analysis can be obtained on request for use, on condition that the source should be acknowledged whenever use is made.

Appendix A: Application to intermetallics, dispersion strengthened alloys and composites

(This section was completed in collaboration with M. Raviathul Basaria).

Table 5 presents the results obtained by the procedure outlined in the main paper. Systems 1–4 were studied in [14, 15], systems 5–9 in [16] and the rest in [17]. As before, the required material properties were extracted from [41, 42, 48]. For comparison, the values obtained earlier are also included in Table 5. The measure of prediction accuracy was defined, as before, as the larger value

between $(\dot{\epsilon}_{\text{experimental}}/\dot{\epsilon}_{\text{predicted}})$ and $(\dot{\epsilon}_{\text{predicted}}/\dot{\epsilon}_{\text{experimental}})$ ratios (Tol).

In this case also, in accordance with theory, the value of γ_0 for a given system increases with increasing temperature. In the earlier numerical validation procedures, γ_0 was assumed (as an approximation) to be independent of temperature and system. A few more points are also worthy of note: for systems 1–4 the accuracy of predictions has improved with the present algorithm. For systems 3 and 4 of similar composition, in each paper the grain size and temperature are different. In these cases the values of ΔF_0 and γ_0 at the common temperature of 1723 K are found to agree very well, which demonstrates the robustness of the present algorithm. For the rest of the systems, it is noted that in the earlier method [16, 17] ΔF_0 value was calculated at each temperature for each datum point and then a mean value was obtained which gave rise to very accurate predictions. But that method did not use the method of least squares, as done here, which makes the statistics used here more formal/correct.

The correlation coefficient for the relation between γ_0 and T for the Ti–Al systems (systems 7–9) is 0.9983; similarly for the aluminium-based systems 10–12, of similar composition, a correlation coefficient of 0.9159 is obtained. System 13 is omitted from this correlation although it is also an Al alloy because of its considerably different composition.

See Table 5.

Table 5 Details and the results of the intermetallic and other systems analysed

Sl. No	Composition and L, μm	T (K)	ΔF_0 (kJ mol ⁻¹)		σ_0 (MPa)		Tol		γ_0 , refined
			Old	New	Old	New	Old	New	
1	Al 33.6Cu 0.44Zr, 7.6 [50]	713	141.5	146	0.90	1.44	1.7	1.10	0.1268
		753		149	0.70	0.67	1.3	1.10	0.1302
		793		149	0.50	0.46	1.2	1.24	0.1324
2	Al 13Si, 18 [51]	791	135.0	137	0.34	0.56	2.9	1.58	0.1269
		811		141	0.32	0.51	2.1	1.59	0.1290
		831		143	0.30	0.51	2.3	2.06	0.1309
3	ZrO ₂ 3Y ₂ O ₃ (mol%), 0.41 [52]	1623	393.0	388	2.94	3.09	16.9	9.74	0.0996
		1673		384	2.92	2.94	17.1	8.09	0.1009
		1723		404	2.90	2.94	9.7	8.37	0.1054
4	*ZrO ₂ 3Y ₂ O ₃ (mol%) [52]	1723	393.0	404	2.94	3.09	9.7	4.88	0.1072
				403	2.92	2.94	6.4	8.70	0.1054
				418	2.90	2.94	10.6	9.75	0.1054
5	Co ₃ Ti, 24 [53]	1173	219.3	221	16.9	5.74	1.1	1.76	0.1288
		1223	219.0	225	10.3	2.64	1.2	1.83	0.1340
		1273	218.7	229	9.70	2.01	1.1	1.89	0.1397
6	Ni ₃ Si, 15 [54]	1323	176.6	226	14.33	12.36	1.1	1.19	0.1482
		1353	176.3	221	8.10	7.58		1.42	0.1499
		1373	175.3	224	1.02	0.83		1.35	0.1532

Table 5 continued

Sl. No	Composition and L, μm	T (K)	ΔF_o (kJ mol ⁻¹)		σ_o (MPa)		Tol		γ_o , refined
			Old	New	Old	New	Old	New	
7	Ti 46.8Al (at.%), 0.8 [55]	1073	242.2	262	18.1	39.63	1.1	2.03	0.1131
		1123	242.8	271	9.0	17.26		2.06	0.1179
		1173	245.3	277	8.9	9.49		1.45	0.1222
8	Ti 47Al (at.%), 5 [56]	1273	247.7	282	11.8	20.84	1.3	1.63	0.1305
		1323		286	6.01	9.79	1.2	1.55	0.1353
		1373		292	5.72	5.29	1.3	1.86	0.1413
9	Ti 48Al (at.%), 0.9 [57]	1163	240.3	280	34.0	17.21	1.2	1.03	0.1222
		1273	240.6	285	8.60	6.75	1.2	1.17	0.1312
		1373	240.3	290	4.60	3.72	1.1	1.13	0.1409
10	Al 5 Mg, 24 [58]	748	151.78	129	1.95	23.51	1.07	1.39	0.0719
		773		132	0.90	15.59	1.07	1.31	0.0734
		793		134	0.71	11.95	1.09	1.25	0.0745
11	Al 5.76 Mg, ~1.2 [59]	523	113.57	105	–	30.50	–	1.22	0.0602
		573		107	19.3	12.94	1.14	1.50	0.0616
		623		104	14.5	12.93	1.23	2.11	0.6200
		673		106	9.95	9.55	1.23	1.83	0.0633
		723		105	–	9.44	–	1.60	0.0644
12	Al–5.76 Mg, 3 [60]	723	150.65	123	22.5	4.21	1.19	2.04	0.0694
		748		125	19.5	3.37	1.17	2.80	0.0707
		793		127	13.3	2.07	1.16	5.84	0.0721
13	Al 17Si 2Fe 2 Mg, 1.4 [61]	763	139.61	124	–	13.80	–	4.57	0.1039
		783		125	6.50	7.55	1.15	3.33	0.1049
		793		124	3.70	4.92	1.16	4.37	0.1050
		803		129	2.20	1.72	1.19	7.75	0.1077
14	Mg 6Zn 0.8Zr, 0.65 [62]	473	116.99	95	10.8	11.54	1.16	3.95	0.0998
		498		98	8.40	8.65	1.15	3.87	0.1017
		523		99	6.30	6.27	1.14	5.86	0.1033
15	6 061/20 %SiC, ~2.6 [63]	823	150.60	–	5.15	–	1.09	–	–
		843		128	2.36	6.08	1.05	2.13	0.1219
		863		129	1.22	1.78	1.10	2.64	0.1221
		883		124	–	0.75	–	2.74	0.1235
16	7075/20 %SiC, 1.75 [64]	753	134.07	118	10.1	9.56	1.09	2.19	0.1129
		773		118	6.58	6.46	1.03	1.98	0.1139
		793		116	4.94	4.46	1.04	2.74	0.1141

*For system 4, the grain size was the variable; at a constant temperature of 1723 K experiments were conducted with grain sizes of 0.41, 0.66 and 1.20 μm , respectively

References

- Davies GJ, Edington JW, Cutler CP, Padmanabhan KA (1970) J Mater Sci 5:1091. doi:10.1007/BF02403283
- Padmanabhan KA, Davies GJ (1980) Superplasticity: mechanical and structural aspects, environmental effects, fundamentals and applications. Springer-Verlag, Berlin-Heidelberg
- Kaibyshev OA (1992) Superplasticity of Alloys, Intermetallides, and Ceramics. Springer-Verlag, New York
- Nieh TG, Wadsworth J, Sherby OD (1997) Superplasticity in metals and ceramics. Cambridge University Press, Cambridge
- Padmanabhan KA, Vasin RA, Enikeev FU (2001) Superplastic flow: common basis for a ubiquitous phenomenon. Springer, New York
- Padmanabhan KA, Gleiter H (2012) Curr Opin Solid State Mater Sci 16:243. doi:10.1016/j.cossms.2012.05.001
- Karato S, Zhang S, Wenk H (1995) Science 270:458. doi:10.1126/science.270.5235.458
- Goldsby DL, Kohlstedt DL (2001) J Geophys Res Solid Earth 106:11017. doi:10.1029/2000JB900336
- Huang JY, Chen S, Wang ZQ et al (2006) Nature 439:281. doi:10.1038/439281a

10. Padmanabhan KA, Schlipf J (1996) *Mater Sci Technol* 12:391. doi:10.1179/026708396790165920
11. Venkatesh TA, Bhattacharya SS, Padmanabhan KA, Schlipf J (1996) *Mater Sci Technol* 12:635. doi:10.1179/026708396790122486
12. Hahn H, Padmanabhan KA (1997) *Philos Mag Part B* 76:559. doi:10.1080/01418639708241122
13. Betz U, Padmanabhan KA, Hahn H (2001) *J Mater Sci* 36:5811. doi:10.1023/A:1012956005571
14. Padmanabhan KA, Gleiter H (2004) *Mater Sci Eng* 381:28. doi:10.1016/j.msea.2004.02.054
15. Padmanabhan KA, Dinda GP, Hahn H, Gleiter H (2007) *Mater Sci Eng* 452–453:462. doi:10.1016/j.msea.2006.10.084
16. Padmanabhan KA, Basariya MIR (2009) *Int J Mater Res Former Z Fuer Met* 100:1543. doi:10.3139/146.110218
17. Padmanabhan KA, Basariya MR (2009) *Mater Sci Eng* 527:225. doi:10.1016/j.msea.2009.07.059
18. Padmanabhan KA (2009) *J Mater Sci* 44:2226. doi:10.1007/s10853-008-3076-1
19. Sripathi S, Padmanabhan KA (2012) *Mater Sci Forum* 735:246. doi:10.4028/www.scientific.net/MSF.735.246
20. Mukherjee AK (2002) *Mater Sci Eng* 322:1. doi:10.1016/S0921-5093(01)01115-7
21. Lagneborg R, Bergman B (1976) *Met Sci* 10:20. doi:10.1179/030634576790431462
22. Eshelby JD (1957) *Proc R Soc Lond Ser Math Phys Sci* 241:376. doi:10.1098/rspa.1957.0133
23. Wolf D (1990) *Acta Met Mater* 38:781. doi:10.1016/0956-7151(90)90030-K
24. Wolf D (1990) *Acta Met Mater* 38:791. doi:10.1016/0956-7151(90)90031-B
25. Xie GM, Ma ZY, Geng L, Chen RS (2008) *J Mater Res* 23:1207. doi:10.1557/JMR.2008.0164
26. Watanabe H, Mukai T, Ishikawa K et al (2001) *Mater Trans* 42:157
27. Yan H, Chen R, Han E (2009) *Sci China Ser E: Technol Sci* 52:166. doi:10.1007/s11431-008-0293-4
28. Kim Y, Bae D (2004) *Mater Trans* 45:3298
29. Kumar N, Raman KS, Sastry DH, Little EA (1990) *J Mater Sci* 25:753. doi:10.1007/BF00714105
30. Mohamed FA, Ahmed MMI, Langdon TG (1977) *Met Trans* 8:933. doi:10.1007/BF02661575
31. Shei S-A, Langdon TG (1978) *Acta Met* 26:639. doi:10.1016/0001-6160(78)90116-5
32. Charit I, Mishra RS (2005) *Acta Mater* 53:4211. doi:10.1016/j.actamat.2005.05.021
33. Komura S, Horita Z, Furukawa M et al (2001) *Met Mater Trans* 32:707. doi:10.1007/s11661-001-0087-9
34. Wakai F, Nagano T (1991) *J Mater Sci* 26:241. doi:10.1007/BF00576058
35. Sharif AA, Mecartney ML (2004) *J Eur Ceram Soc* 24:2041. doi:10.1016/S0955-2219(03)00354-6
36. Chen T, Mecartney ML (2005) *J Am Ceram Soc* 88:1004. doi:10.1111/j.1551-2916.2005.00190.x
37. Chen T, Mohamed FA, Mecartney ML (2006) *Acta Mater* 54:4415. doi:10.1016/j.actamat.2006.05.002
38. Dillon RP, Kim D-K, Trujillo JE et al (2008) *J Mater Res* 23:556. doi:10.1557/JMR.2008.0071
39. Xu X, Nishimura T, Hirotsaki N et al (2006) *Acta Mater* 54:255. doi:10.1016/j.actamat.2005.09.005
40. Padmanabhan KA, Davies GJ (1973) *Phys Status Solidi* 18:295. doi:10.1002/pssa.2210180130
41. Frost HJ, Ashby MF (1982) *Deformation-mechanism maps: the plasticity and creep of metals and ceramics*. Pergamon Press, Oxford
42. Gale WF, Totemeier TC (2003) *Smithells metals reference book*. Butterworth-Heinemann, Oxford
43. Sakaguchi S, Murayama N, Kodama Y, Wakai F (1991) *J Mater Sci Lett* 10:282. doi:10.1007/BF00735658
44. Auerkari P (1996) *Mechanical and physical properties of engineering alumina ceramics*. Technical Research Centre of Finland, Finland
45. Vogelgesang R, Grimsditch M, Wallace JS (2000) *Appl Phys Lett* 76:982. doi:10.1063/1.125913
46. Fate WA (1975) *J Appl Phys* 46:2375. doi:10.1063/1.321916
47. Yadava RK, Padmanabhan KA (1979) *Mater Sci Eng* 37:127. doi:10.1016/0025-5416(79)90076-4
48. Bokshtein BS, Bokshtein SZ, Zhukhovitskiy AA (1985) *Thermodynamics and kinetics of diffusion in solids*. Oxonian Press, Oxford
49. Grewer M, Markmann J, Karos R et al (2011) *Acta Mater* 59:1523. doi:10.1016/j.actamat.2010.11.016
50. Matsuki K, Minami K, Tokizawa M, Murakami Y (1979) *Met Sci* 13:619
51. Chung DW, Cahoon JR (1979) *Met Sci* 13:635
52. Owen DM, Chokshi AH (1998) *Acta Mater* 46:667. doi:10.1016/S1359-6454(97)00251-6
53. Kim W-Y, Hanada S, Takasugi T (1998) *Acta Mater* 46:3593. doi:10.1016/S1359-6454(98)00029-9
54. Nieh TG, Oliver WC (1989) *Scr Met* 23:851. doi:10.1016/0036-9748(89)90258-5
55. Sun J, He YH, Wu JS (2002) *Mater Sci Eng* 329–331:885. doi:10.1016/S0921-5093(01)01646-X
56. Wegmann G, Gerling R, Schimansky F-P et al (2002) *Intermetallics* 10:511. doi:10.1016/S0966-9795(02)00026-2
57. Nieh TG, Wadsworth J (1997) *Mater Sci Eng* 239–240:88. doi:10.1016/S0921-5093(97)00564-9
58. Kaibyshev R, Avtokratova E, Apollonov A, Davies R (2006) *Scr Mater* 54:2119. doi:10.1016/j.scriptamat.2006.03.020
59. Musin F, Kaibyshev R, Motohashi Y, Itoh G (2004) *Scr Mater* 50:511. doi:10.1016/j.scriptamat.2003.10.021
60. Nieh TG, Hsiung LM, Wadsworth J, Kaibyshev R (1998) *Acta Mater* 46:2789. doi:10.1016/S1359-6454(97)00452-7
61. Fujino S, Kuroishi N, Yoshino M et al (1997) *Scr Mater* 37:673. doi:10.1016/S1359-6462(97)00153-X
62. Watanabe H, Mukai T, Ishikawa K et al (2001) *Mater Sci Eng* 307:119. doi:10.1016/S0921-5093(00)01974-2
63. Wang T, Huang J (2001) *Mater Trans* 42:1781
64. Nishida Y, Sigematsu I, Arima H et al (2002) *J Mater Sci Lett* 21:465. doi:10.1023/A:1015378405808

A ROBUST NUMERICAL METHOD FOR VALIDATING MESOSCOPIC GRAIN BOUNDARY SLIDING CONTROLLED FLOW MODEL FOR STRUCTURAL SUPERPLASTICITY

Sriharsha Sripathi^{1, a}, K. A Padmanabhan^{1, b}

¹School of Engineering Sciences and Technology, University of Hyderabad, Gachibowli, Hyderabad – 500 046, India.

^asripathi1@yahoo.com, ^bkapse@uohyd.ernet.in, ^bananthaster@gmail.com

Keywords: Structural superplasticity, rate controlling process, mesoscopic grain boundary sliding, superplastic ceramics, sub-micrometer grained materials.

Abstract. Structural superplasticity is observed in materials of different classes with μm –, sub- μm – or nm– grain size. In all cases mesoscopic grain/interphase boundary sliding (\sim grain diameter or more) is suggested to be the rate controlling mechanism [1–3]. Sub- μm grained metallic [4–6] and ceramic [7] systems are analyzed here and good agreement with experimental results is established. Compared with earlier works [3, 8–11], the numerical procedure is more robust, fully automated and the free energy of activation for the rate controlling process is matched with the value for the same obtained using Eshelby's equation [12], which was not done earlier.

Introduction

Structural superplasticity is reported at high homologous temperatures ($\geq 0.4 T_m$, where T_m is the absolute melting temperature; the limit is lower for nanostructured materials). We have published several papers wherein grain boundary sliding (GBS), which develops to a mesoscopic scale (defined to be of the order of a grain diameter or more), is suggested to be the rate controlling process in regions I and II of superplastic deformation (till the point of inflection in the log stress-log strain rate curve) [1-3, 8–11, 13]. In this paper, as an additional step, the free energy of activation for the rate controlling process based on the model presented in [2] is matched with the value calculated by Eshelby's approach [12]. A robust and statistically correct numerical analysis for the validation of the model using data pertaining to sub- μm grained metallic [4–6] and ceramic [7] systems is presented. Good agreement with the experimental results is demonstrated.

The Model

A detailed description of the model, in which GBS is the rate controlling process, can be found in [2, 3, 14]. GBS is viewed as a two-scale process where deformation at a boundary (microscopic scale) develops to a mesoscopic scale (of the order of a grain diameter or more). A high-angle grain boundary is divided into a number of atomic scale ensembles that surround free volume sites present at discrete locations characteristic of the boundary. Due to the presence of free volume, these ensembles possess a lower shear modulus compared with the rest of the boundary and hence constitute the basic units of sliding. For mathematical development, the basic sliding unit is assumed to be an oblate spheroid of 5 atomic diameters in the boundary plane and 2.5 atomic diameters in the perpendicular direction, which (the latter) is roughly equal to the grain boundary width, W . (As the stress-strain field that develops inside a deformed oblate spheroid is already worked out [12] this shape for the basic sliding unit was chosen.) Microscopic sliding persists till it is rendered ineffective by steric hindrances like a triple junction. For GBS to develop to a mesoscopic scale, two or more grains need to align to form a plane interface, which by further interconnection with other similar plane interfaces will lead to long range sliding till it gets stopped

by an insurmountable barrier like an extra-large grain or a coarse precipitate. The Driving force for plane interface formation arises from (a) minimization of the total free energy of the deforming system, and (b) the work done by the external stress reaching its maximum value for this configuration. These processes give rise to a long-range threshold stress which has to be overcome for mesoscopic GBS to set in. The following equations derived are of relevance to this paper.

$$\Delta F_o = \left(\frac{1}{2}\right)(\beta_1 \gamma_o^2 + \beta_2 \varepsilon_o^2) G V_o \quad (1)$$

$$\dot{\varepsilon} = \left(\frac{2cW\gamma_o v}{L}\right) \sinh\left(\frac{(\sigma - \sigma_o)c\gamma_o V_o}{2kT}\right) \exp\left(\frac{\Delta F_o}{kT}\right) \quad (2)$$

$$V_o = \left(\frac{2}{3}\right)\pi W^3; \beta_1 = 0.944\left(\frac{1.59-p}{1-p}\right); \beta_2 = \left(\frac{4(1+p)}{9(1-p)}\right); v = \left(\frac{kT}{h}\right); W = 2.5a; \quad (3)$$

$$SD = \left(\frac{\sum(\dot{\varepsilon}_{\text{expt}} - \dot{\varepsilon}_{\text{pred}})^2}{n-2}\right)^{0.5}; AE = \left(\frac{SD}{\sqrt{n}}\right); r = \frac{\sum \dot{\varepsilon}_{\text{expt}} \dot{\varepsilon}_{\text{pred}} - n \dot{\varepsilon}_{\text{expt}} \dot{\varepsilon}_{\text{pred}}}{(\sum \dot{\varepsilon}_{\text{expt}} - n \dot{\varepsilon}_{\text{expt}})(\sum \dot{\varepsilon}_{\text{pred}} - n \dot{\varepsilon}_{\text{pred}})} \quad (4)$$

Eq. 1 is Eshelby's equation for the free energy of activation, ΔF_o , for the deformation of the oblate spheroid, i.e. the free energy of activation for a basic sliding event, while Eq. 2 is the rate equation for the GBS model. Eq. 3 defines the terms used in Eq. 1 and Eq. 2. The set of equations in Eq. 4 defines the formulae used for statistical analysis.

Specifically ΔF_o is the sum of the energy required to shear the basic sliding unit of oblate spheroid by unit shear strain, γ_o and the energy to produce the momentary dilatation, ε_o , necessary before the unit shear can take place inside a solid matrix, G the shear modulus of the basic sliding unit at the test temperature, p the Poisson ratio, V_o the volume of the basic sliding unit, W the grain boundary width, v the thermal vibration frequency, β_1 , β_2 constants appropriate to the oblate spheroid shape [12], k the Boltzmann constant, h the Planck's constant, T the test temperature on the absolute scale, σ the external tensile stress, c a yield-criterion dependent constant (von Mises for the current work and so $\gamma_o = \sqrt{3}\varepsilon_o$), SD the standard deviation, AE the average error, r the correlation coefficient, $\dot{\varepsilon}$ the external strain rate, the subscripts 'expt', 'pred' and 'm' stand for experimental, predicted and the mean respectively, n the number of readings at each temperature and σ_o is the threshold stress that has to be exceeded to enable microscopic GBS to develop to a mesoscopic scale. The grain shape is assumed to be rhombic dodecahedron. The average grain size is L .

Algorithm:

Initially γ_o was assigned a value of 0.10 [15]. Evidently, at every temperature σ_o should be less than the lowest stress at which flow is reported. σ_o is assigned values starting from δ to $(\sigma_{\text{minimum}} - \delta)$; ($\delta \sim 0.001 \sigma_{\text{minimum}}$). At each temperature, in Eq. 2 using the mean of the experimental values of the stress and the corresponding strain rate, ΔF_o for each of the σ_o values was computed. At all temperatures, the errors (defined in Table 1) in the prediction of strain rate for all the stresses were determined and those combinations of $\Delta F_o - \sigma_o$ which fell within a prescribed error range were accepted. Among these the ΔF_o value at each temperature, which together for the different temperatures formed the nearest numerical set, and the corresponding σ_o values were chosen. Thus, the ΔF_o value was nearly independent of temperature. At each temperature, the selected ΔF_o value was used, along with Eq. 1, to refine γ_o iteratively till a near-stable γ_o value (~ 0.10) was obtained.

Computation Outcome:

Table 1 presents a summary and an error analysis of the results (the error defined as the larger between $\left(\frac{\dot{\epsilon}_{\text{pred}}}{\dot{\epsilon}_{\text{expt}}}\right)$ and $\left(\frac{\dot{\epsilon}_{\text{expt}}}{\dot{\epsilon}_{\text{pred}}}\right)$). For this model, a temperature-independent ΔF_0 value is expected. In contrast, the algorithm is designed to choose those values of ΔF_0 , which suit the results the best. The difference between the maximum and the minimum values of ΔF_0 for systems 1 to 5 (Table 1) are ~ 20 , 10, 12, 17 and 6 $\text{kJ}\cdot\text{mol}^{-1}$ respectively. As the maximum accuracy with which the ΔF_0 value is measured in an experiment is often $\sim \pm 42 \text{ kJ}\cdot\text{mol}^{-1}$ [16], the temperature-dependent variation in the ΔF_0 value observed may be regarded as due to experimental scatter.

The graphs below (Figs 1 to 5) illustrate the fits between the experimental and the predicted values.

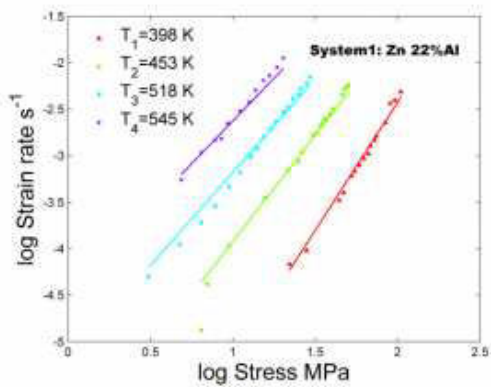


Fig. 1

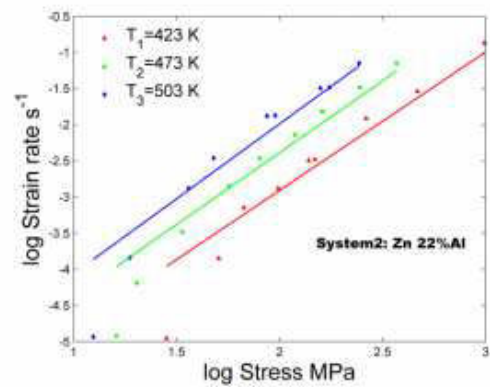


Fig. 2

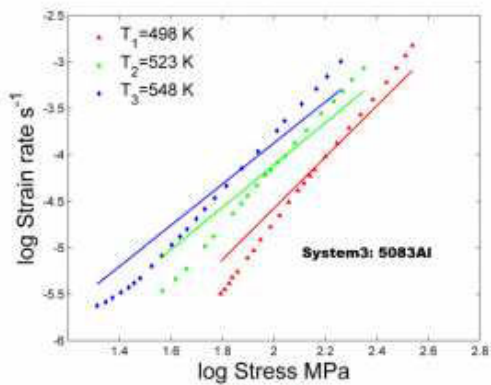


Fig. 3

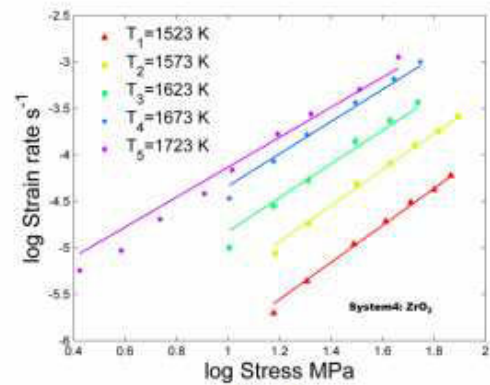


Fig. 4

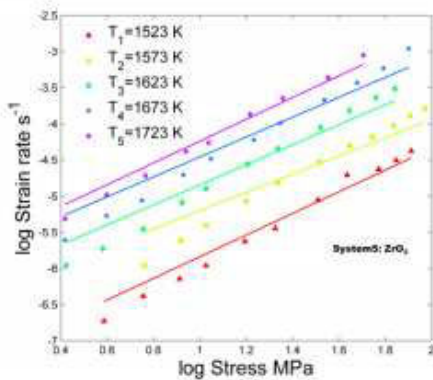


Fig. 5

Figures 1–5: Strain rates predicted (refer Table 1 for system description). Symbols represent experimental data, lines represent the prediction.

Table 1: Summary and an error analysis of the systems

Fig. No	System	T, [K]	L, [μm]	100% γ_0	ΔF_0 [$\text{kJ}\cdot\text{mol}^{-1}$]	σ_0 [MPa]	Maximum error (larger quantity between $\left(\frac{\dot{\epsilon}_{\text{pred}}}{\dot{\epsilon}_{\text{expt}}}\right)$ and $\left(\frac{\dot{\epsilon}_{\text{expt}}}{\dot{\epsilon}_{\text{pred}}}\right)$)	SD	AE	r	Reference
1	Zn 22% Al	398	0.9	8.4623	82.1543	20.9728	2.27	0.0245	0.0061	0.9176	[4]
		453									
		518									
		545									
2	Zn 22% Al	423	2.5	9.4105	84.1714	26.9410	4.72	0.1048	0.0349	0.9996	[5]
		473									
		503									
3	5083 Al	498	0.3	10.6494	122.8297	61.0581	3.35	0.0120	0.0025	0.9285	[6]
		523									
		548									
4	ZrO ₂	1523	0.51	9.5926	379.3761	12.9094	1.30	0.0022	0.0008	0.9859	[7]
		1573									
		1623									
		1673									
		1723									
5	ZrO ₂	1523	0.75	10.2311	390.2677	2.4011	2.09	0.0106	0.0035	0.9675	[7]
		1573									
		1623									
		1673									
		1723									

A Careful examination of Table 1 and the figures reveals that the maximum error between the experimental and the predicted values of the strain rate at any point for all the systems studied taken together is less than 7. As in “order of magnitude” calculations of the present kind a fit is regarded as excellent when the error is less than 10, the fit of the experimental data to the model equations for all the systems examined here may be regarded as very good.

Conclusions:

It is seen that the predictions match the experimental results closely and are well within an order of magnitude, even when the same model is used for both metallic and ceramic systems. The grain sizes in all but one system are in the sub-micron range. For γ_0 , a system-dependent, more accurate value (which is close to 0.10) is obtained, instead of an average value of 0.10, which was assumed earlier based on MD simulations [15].

References:

- [1] K. A. Padmanabhan: Mater. Sci. Eng. Vol. 29 (1977), p. 1
- [2] K. A. Padmanabhan and J. Schlipf: Materials Science and Technology Vol. 12 (1996), p. 391
- [3] K. A. Padmanabhan and H. Gleiter: Materials Science and Engineering A Vol. 381 (2004), p. 28
- [4] N. Kumar, K. S. Raman, D. H. Sastry and A. Little: Journal of Materials Science Vol. 25 (1990), p. 753
- [5] Y. G. Ko, D. H. Shin, K-T Park and C. S. Lee: Materials Science and Engineering A Vol. 449–541 (2007), p. 756
- [6] F. A. Mohamed, M. M. I. Ahmed and T. G. Langdon: Metallurgical Transactions A Vol. 8A, (1977), p. 933
- [7] F. Wakai and T. Nagano: Journal of Materials Science Vol. 26 (1991), p. 241
- [8] T. A. Venkatesh, S. S. Bhattacharya, K. A. Padmanabhan and J. Schlipf: Materials Science and Technology Vol. 12 (1996), p. 635
- [9] K. A. Padmanabhan, G. P. Dinda, H. Hahn and H. Gleiter: Materials Science and Engineering A Vol. 452–453 (2007), p. 462
- [10] K. A. Padmanabhan and M. R Basaria: Int. J. Mat. Res. Vol. 11 (2009), p. 1543
- [11] K. A. Padmanabhan and M. R. Basaria: Materials Science and Engineering A Vol. 527 (2009), p. 225
- [12] J. D. Eshelby: Proc. Roy. Soc. London A Vol. 241 (1957), p. 376
- [13] K. A. Padmanabhan and G. J. Davis: Superplasticity (Springer-Verlag, Heidelberg, Berlin 1980).
- [14] K. A. Padmanabhan: J. Mater. Sci. Vol. 44 (2009), p. 2226
- [15] Wolf D: Acta Metall. Mater. Vol.38 (1990), p.781, 791
- [16] B. S. Bokshetein, S. Z. Bokshetein, A. A. Z. Zhukhourtskii: Thermodynamics and Kinetics of Diffusion in Solids (Oxonion Press Pvt. Ltd., New Delhi 1985).